INFORMATION TO USERS

This manuscript has been reproduced from the microfilm master. UMI films the text directly from the original or copy submitted. Thus, some thesis and dissertation copies are in typewriter face, while others may be from any type of computer printer.

The quality of this reproduction is dependent upon the quality of the copy submitted. Broken or indistinct print, colored or poor quality illustrations and photographs, print bleedthrough, substandard margins, and improper alignment can adversely affect reproduction.

In the unlikely event that the author did not send UMI a complete manuscript and there are missing pages, these will be noted. Also, if unauthorized copyright material had to be removed, a note will indicate the deletion.

Oversize materials (e.g., maps, drawings, charts) are reproduced by sectioning the original, beginning at the upper left-hand corner and continuing from left to right in equal sections with small overlaps. Each original is also photographed in one exposure and is included in reduced form at the back of the book.

Photographs included in the original manuscript have been reproduced xerographically in this copy. Higher quality 6" x 9" black and white photographic prints are available for any photographs or illustrations appearing in this copy for an additional charge. Contact UMI directly to order.

UMI

A Bell & Howell Information Company
300 North Zeeb Road, Ann Arbor MI 48106-1346 USA
313/761-4700 800/521-0600

Nonlinear Characteristics of Tuned Liquid Dampers

by

Jin Kyu Yu

A dissertation submitted in partial
fulfillment of the requirements for the
degree of

Doctor of Philosophy

University of Washington

1997

Approved by ______________________
Chairperson of Supervisory Committee

____

____

____

____

Program Authorized
to Offer Degree Civil Engineering

Date 1/31/97

UMI Number: 9730145

UMI
300 North Zeeb Road
Ann Arbor, MI 48103

Doctoral Dissertation

Signature ____________

Date 1/29/97

University of Washington

Abstract

Nonlinear Characteristics of Tuned Liquid Dampers

by Jin Kyu Yu

Chairperson of the Supervisory Committee: Professor Dorothy A. Reed
Department of Civil Engineering

In recent years, tuned liquid dampers (TLD) have been successfully employed in practice to mitigate undesirable structural vibrations. Although this device has many advantages, its damping mechanism has not been thoroughly investigated, nor are any definite guidelines available for TLD design. In this study, the behavior of TLD is investigated experimentally and numerically. The results are incorporated into the development of a design procedure.

Shaking table experiments were conducted to investigate the characteristics of the shallow water sloshing motion in rectangular or circular tanks under small and large amplitude excitations. The results reveal that the most distinguishing characteristic of the shallow-water is a hardening-spring type nonlinearity. The nonlinearity is explicitly quantified using the jump-frequency as a function of excitation amplitude and tank size. It was found that the characteristics of nonlinearity are different in two regions: identified as the weak wave breaking and strong wave breaking regions.

An equivalent TMD model was developed to capture the energy dissipation capacity of the TLD based on the experimental results by means of energy dissipation curve matching. The nonlinear stiffness and damping characteristics of the TLD were incorporated into this model as functions of excitation amplitude and tank size.

A numerical fluid model using the random choice method to solve the shallow-water wave equations proposed by Gardarsson and Yeh (1994) was employed to simulate shallow-water sloshing motion in a rectangular tank. It was found that the model accurately simulated weak or moderate wave breaking. However, the model cannot capture the wave phenomenon under extremely strong excitation motions.

Numerical schemes were developed to simulate the dynamic motions of a single-degree-of-freedom structure coupled with a TLD. Based on the captured nonlinear properties of the TLD, a nonlinear tuning procedure is proposed. The performance of TLDs in mitigating the structural vibration was evaluated using the interaction model of a structure with a proposed equivalent TMD. The results reveal that the nonlinear tuning enhances the TLD performance. A TLD design procedure under harmonic and white noise excitations is developed based on the results of performance investigations.

Finally, the performance of TLDs under wind or earthquake conditions was investigated numerically. For the simulated wind condition, the selected TLD reduced the structural vibrations significantly. For the Northridge earthquake, the TLD was ineffective during the initial stage of the earthquake. The performance of the TLD for earthquake loadings must be further investigated.

TABLE OF CONTENTS

LIST OF FIGURES

LIST OF TABLES

Number Page

NOTATION AND ABBREVIATIONS

A	Amplitude of base excitation Maximum structural displacement
$A_{\max}$	Maximum allowable structural displacement
B, b	Tank width
D	Tank diameter
E	Energy
$E[\ ]$	Ensemble average of the quantity in [ ]
E_d	Energy dissipation by the damper
F	Force
F_w	Base shear force due to water sloshing
F_η	Hydrodynamic force calculated based on hydrostatic water pressure on the tank end walls.
$H_{a/b}$	Complex frequency response function relating output a to input b.
L	Tank length
S	Spectral density function
S_0	Constant spectral density of white noise input
T	Fundamental period
c	Damping coefficient
c_{cr}	Critical damping coefficient ($c_{cr} = 2m\omega = 2\sqrt{km}$)
f	Frequency (in Hz) External forcing frequency
f_d	Natural frequency of the damper Nonlinear natural frequency of the TLD: $f_d = \xi f_w$
f_e	External forcing frequency
f_{jump}	Jump frequency
f_w	Linear natural frequency of the TLD based on linear theory
g	Gravity acceleration

h_0	Undisturbed water depth
k	Stiffness coefficient
k_d	Stiffness of the damper
k_w	Fundamental linear stiffness of the TLD
m	Mass
m_d	Mass of the damper
m_s	Mass of the structure
m_w	Mass of the water
u	Horizontal velocity of water particles
x	Absolute displacement of the structure
$\bar{x}$	Relative displacement of the structure
x_0	Maximum displacement of the structure without damper Initial displacement of the structure in free vibration
x_s	Structural displacement
x_d	Damper's displacement
Λ	Nondimensional excitation amplitude (A/L)
β	Excitation frequency ratio ($\beta = f_e / f_s$)
β_d	Damper frequency ratio to external forcing frequency
β_{jump}	Jump frequency ratio ($\beta_{jump} = f_{jump} / f_w$)
ε	Water depth ratio ($\varepsilon = h/L$)
ϕ	Phase angle
γ	Damper frequency ratio (f_d/f_s)
η	Wave height or free water surface elevation
κ	Stiffness hardening ratio or non-dimensional stiffness of damper
μ	Mass ratio (m_d/m_s)
ω, ω_e	External forcing angular frequency
ω_s	Excitation angular frequency of shaking table

	Natural angular frequency of structure
ω_d	Natural angular frequency of damper
ω_w	Fundamental linear angular frequency of the TLD
ξ	Frequency shift ratio
ζ	Damping ratio ($\zeta = {}^{c}\!/_{c_{cr}}$)
ζ_s	Damping ratio of structure
ζ_d	Damping ratio of damper

Superscripts

a'	Nondimensionalized value of a
$\dot{a}$	Time derivative of a

Subscripts

d	Damper
e	External
s	Structure

DOF	Degree Of Freedom
NSD	A SDOF System with Nonlinear Stiffness and Damping
RCM	Random Choice Method
RMS	Root Mean Square
SDOF	Single Degree Of Freedom
TLD	Tuned Liquid Damper
TMD	Tuned Mass Damper

ACKNOWLEDGMENTS

I would like to thank Professor Dorothy A. Reed for providing the opportunity to perform this research. Without her valuable guidance and continuous support through the long process of research, this dissertation would not have been possible.

I with to extend my sincere appreciation to Professor Harry Yeh. His sharp insight into the subject always guided me to the right track of the research.

Appreciation is also directed to Professors Gregory Miller and George Turkiyyah for their thorough review of this dissertation in a timely manner. Their comments and suggestions significantly improved this document.

Most of all, my gratefulness is to my wife Myung, son Jeehah and daughter Jean for their love, support and patience.

CHAPTER 1

INTRODUCTION

Undesirable vibrations of lightly damped, flexible modern structures have created concern in the structural engineering community. Although these vibrations are related to serviceability problems, such as occupant comfort and cladding integrity, rather than affecting the primary load-bearing capacity, the economic considerations are significant. The most promising solution to mitigating these vibrations is through the use of artificial damping devices.

In recent years, one type of passive damping system, called the tuned liquid damper (TLD) has been successfully employed in practice, e.g., Fediw, et al. (1993); Fujii, et al. (1990); Tamura, et al. (1988); Ueda, et al. (1991); Wakahara, et al. (1992, 1993). Although this type of device has many advantages, the mechanism by which it dissipates energy related to undesirable vibrations is not completely understood, nor has it been thoroughly investigated. The primary objective of this study is to investigate experimentally and numerically the behavior of tuned liquid dampers in order not only to identify the underlying physical phenomenon of the liquid sloshing behavior that contributes to the damping capability of the device, but also to incorporate such knowledge into the development of a design scheme.

In this chapter, a review of background information for this study will be presented. Following this review, an outline of the organization of this dissertation is provided.

1.1 Tuned liquid damper (TLD)

The tuned liquid damper is a passive mechanical damper designed to suppress undesirable structural vibration through the liquid sloshing motion in a rigid tank. The vibration energy is dissipated by means of friction in the boundary layers of the fluid, contamination of the free surface and wave breaking. Water is most commonly used as a liquid for the TLD, hence, the words "water" and "liquid" are used interchangeably throughout this study.

For analysis purposes, the water in rigid tanks is classified as "deep" or "shallow". The specific classification is based on the ratio of the water depth to the wave length in the direction of motion. The damping mechanism in the water is developed primarily by the viscous action in the boundary layers near the bottom surface and the side walls of the tank and the sloshing motion of the free surface layer of the water. As a damper, deep water is limited in its damping capability because a large portion of the water does not participate in the damping mechanism. Shallow water maximizes the participation of the water in the damping action. This research focuses on the TLD using shallow water.

The motion of liquids in rigid containers has been a subject of many studies due to its frequent applications in engineering disciplines, e.g., Chaiseri, et al. (1989); Chester, et al. (1968); Faltinson, et al. (1978); Housner (1959); Lepelletier (1988); Miles (1976); Modi, et al. (1988); Shimizu, et al. (1987). Notable progress in numerical simulation of the shallow water for the rectangular TLD was made by Sun (1992). Because his analytical model can not simulate the water sloshing motion with wave breaking, he introduced two empirically-based coefficients for damping and frequency shift in the governing equations. Koh et al. (1994) modified Sun's model to make the energy dissipation term applicable to arbitrary excitations. Gardarsson and Yeh (1994) proposed a numerical solution scheme to solve the shallow-water equations using the random choice method (RCM).

Recently, successful applications of TLDs to civil engineering structures have been reported. It was found that the TLD has several potential advantages over other damping systems, such as low installation and maintenance cost; fewer mechanical problems; no fail-safe devices required; activated at even low excitation levels; and easy adjustment of the damper parameters even after installation by adjusting the water level in the tank. This result implies a promising future of TLD as a damping device for various types of civil engineering structures including super flexible tower-type structures and high-rise buildings. It is also noted that there exist difficulties in TLD design because of the complex behavior of liquid sloshing that involves a consideration of wave breaking and amplitude dependent nonlinear characteristics.

1.2 Damping mechanism of the TLD

In this section, the damping mechanism of the TLD is reviewed. Because the tuned mass damper (TMD) is a well-known passive mechanical damping system that has been used widely for serviceability-based structural vibration control, the damping mechanism of the TMD is continuously referenced in explanations of the TLD.

Figure 1.1 demonstrates schematics of passive mechanical dampers (TLD & TMD)

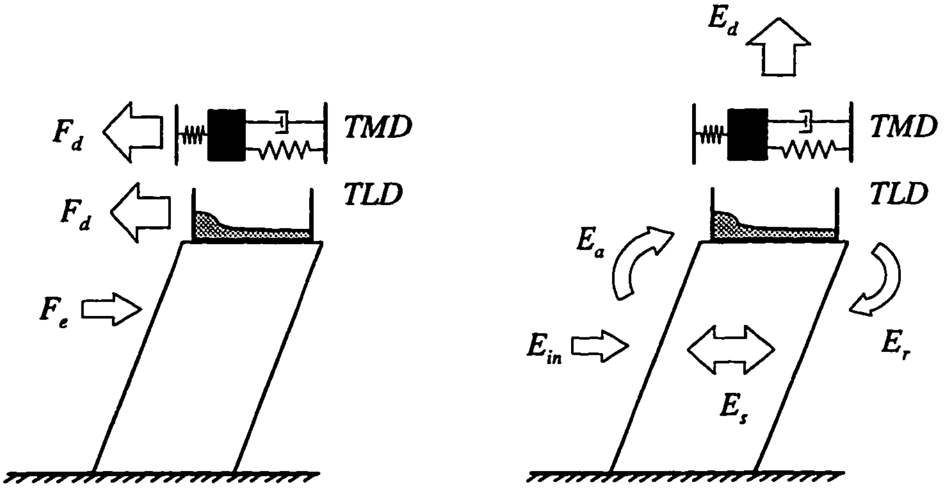

(a) Resisting Force

(b) Energy Flow

Figure 1.1 Mechanisms of the mechanical dampers (TLD & TMD): F_e = excitation force; F_d = resisting force by dampers; E_{in} = energy input; E_a = energy absorbed by dampers; E_d = energy dissipated by dampers; E_r = energy returned to structure; E_s = structural vibration energy.

attached to a structure. Figure 1.1(a) schematically illustrates the inertia forces of the solid mass in the TMD and the water mass in the TLD resisting structural motion as the structure is subjected to an external force. Figure 1.1(b) presents the energy flow among the excitation force, the structure and the damper. The dampers absorb a part of the structural vibration energy. The absorbed energy is dissipated through the damper's inherent damping capacity. The energy flow from the structure to the damper is called the "energy absorption mechanism". The damper changes the dynamic characteristics of the structure by changing the phase of the structural motion through the absorption mechanism. The structural vibration energy is dissipated through the energy dissipation capacity of the damper.

The motion of the solid mass and the characteristics of the stiffness and damping of the TMD have been thoroughly investigated. However, the motion of the water mass and the characteristics of the stiffness and damping of the TLD have not been subject to the same level of scrutiny. In particular, as the wave breaking occurs, the water sloshing motion cannot be predicted by analytical methods.

1.3 Performance measurement of damping devices

The ultimate goal of this research is to develop a design process for the TLD. The design criteria must be evaluated in the context of damper performance. Performance of the damper is defined as the capability to reduce undesirable structural motion effectively and robustly. Effectiveness of the damper may be assessed in several ways, including one or more of the following (Reed, et al., 1996):

- Reduction in peak or RMS structural displacement;
- Reduction in peak or RMS structural acceleration;
- Increase in "effective damping" of the combined system when the main system coupled with the damper is treated as a single-degree-of-freedom combined system; or
- Increase in energy dissipation per cycle over a system without a damping device.

Performance of the damper in terms of robustness is another important consideration in damper design. Robustness of the damper performance is not a well-defined term. However, in general, it would be qualitatively defined as "the level of insensitivity of the damper effectiveness to slight offsets in damper parameters from the desired values." The damper parameters in this sense include, but are not limited to, the tuning and damping ratios of the damper. The offset in the damping parameters occurs mainly due to the inaccurate estimations of the structural properties, damper properties, mass ratio, or loading conditions. In this research, the robustness of the TLD will be assessed in the context of energy dissipation over a wide range of excitation frequencies.

1.4 Objectives and scope of work

Despite several successful applications as well as numerical and experimental investigations of the TLD behavior, there currently exist limitations which restrict the designer's ability to effectively employ the TLD as a damping device. These limitations include, but are not limited to, the following:

- The underlying physical phenomenon of the water sloshing motion is not thoroughly understood. Although the wave breaking phenomenon is common in real practice, water sloshing with wave breaking has rarely been addressed in research. Some important characteristics of shallow water sloshing motion such as nonlinearity have been identified but not explicitly quantified.
- Present methods for TLD design involve many approximations and there are no definitive guidelines.

In recognition of these limitations, the primary objectives of this study were established as follows:

- To investigate the characteristics of the shallow water sloshing motion in a tank using shaking table experiments under small and large amplitude excitations.

- To explicitly identify and quantify parameters which significantly influence the TLD performance.
- To develop a simple mechanical model of the TLD based on the experimental results.
- To identify a numerical fluid model based on the shallow-water equations for use in prediction of tank behavior.
- To develop a design procedure for the TLD.

In this thesis, background theory and results of the experimental investigations will be presented prior to the numerical models. Design procedures and their applications under various loading conditions will be discussed.

Chapter 2 presents the results of experimental investigations of the characteristics of shallow water waves in rectangular and circular tanks. The behavior of wave breaking in rectangular tanks is examined in detail. Because structural vibration is not purely uni-axial motion, circular TLDs may be more feasible than rectangular ones. The characteristics of wave motion in circular tanks are discussed based on the experimental results.

In Chapter 3, an equivalent TMD model of a TLD of rectangular or circular shape is proposed. This model possesses nonlinear stiffness and damping calibrated from the experimental investigations. This model is called the NSD model because of the nonlinear stiffness and damping parameters. An energy dissipation matching scheme used to identify these parameters will be described in detail. A numerical scheme to solve the shallow-water wave equations using the random choice method (RCM model) proposed by Gardarsson and Yeh (1994) will be evaluated based on the experimental results.

In Chapter 4, numerical schemes to model the interaction of a TLD with a single-degree-of-freedom structure are developed. The capability and limitations of the RCM model are evaluated. Frequency response analysis methods coupled with an iterative procedure to solve the nonlinear system are developed for harmonic or white noise excitations. Performance of the TLD is evaluated using the solution scheme. A dynamic searching scheme for the effective TLD design is proposed. Performance of TLDs under wind or earthquake conditions is investigated. Wind pressure time series data were generated using an autoregressive model. Ground displacement data for Northridge earthquake were selected for the study. Conclusions of the research are summarized in Chapter 5.

CHAPTER 2

EXPERIMENTAL INVESTIGATIONS OF SHALLOW WATER WAVES IN RECTANGULAR AND CIRCULAR TANKS

A series of shaking table experiments were conducted to investigate the characteristics of water sloshing motion in rectangular and circular tanks under various base excitation conditions. The results for harmonic base excitation are presented in this chapter. The results for earthquake conditions will be discussed in Chapter 4.

2.1 Shaking table tests

2.1.1 Test set-up

Figure 2.1 shows the schematic diagram of the shaking table experiment set-up. The experiment was conducted using the facilities in the structural dynamics laboratory at the University of Southern California. The components of the experimental set-up are described below:

1) Shaking Table: The MTS shaking table can generate a horizontal motion in one direction. The shaking table has capacities of ± 51 mm maximum displacement, 890 mm/sec maximum velocity, $4g$ maximum acceleration, and 0 to 50 Hz operating frequency. The amplitude and the frequency of the harmonic shaking table excitation was controlled manually using the console panel. The feed-back signal from the actuator is recorded as the shaking table displacement, x_s.

2) Loadcell: The multi-component transducer can measure six directional components of force/moment. The loadcell was calibrated on site under static and dynamic loads.

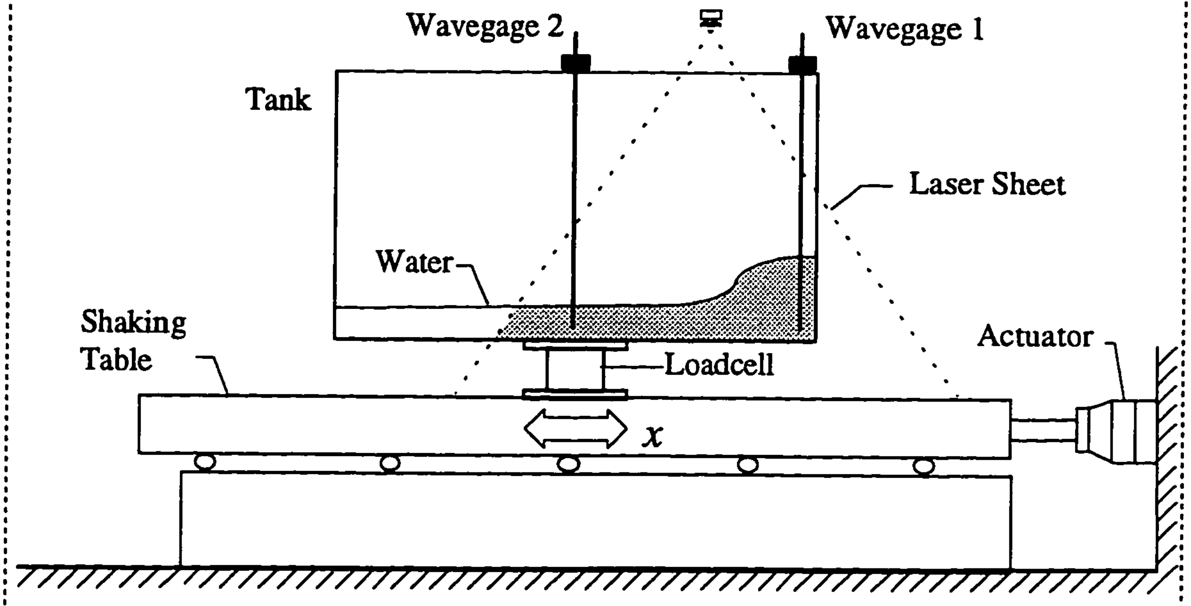

Figure 2.1: Shaking table experiment set-up.

3) Wavegage: Capacitance-type wave gages were installed near the end wall, at the mid-tank[*1] and at the middle of the side wall of the circular tank. The gages near the wall are located at 17 mm and 40 mm from the inside surface of the tank wall for the rectangular tank and the circular tank respectively.

4) Laser-light sheet: A higher-power (4W) Argon-ion laser projects a laser beam. The laser beam is directed through fiber-optics and converted to a thin laser sheet by a scanner. The image of the vertical laser-sheet illumination through the water depth is captured by a video camera and processed with a microcomputer. The quantitative video visualization allows for analysis of the spatial, as well as temporal, variations of the water surface profiles.

[*1] In the shortest tank (L=335 mm), wave gage was installed only at the end wall because there was no space for mounting. For the circular tank, an additional wage gage was installed at the middle of the side wall.

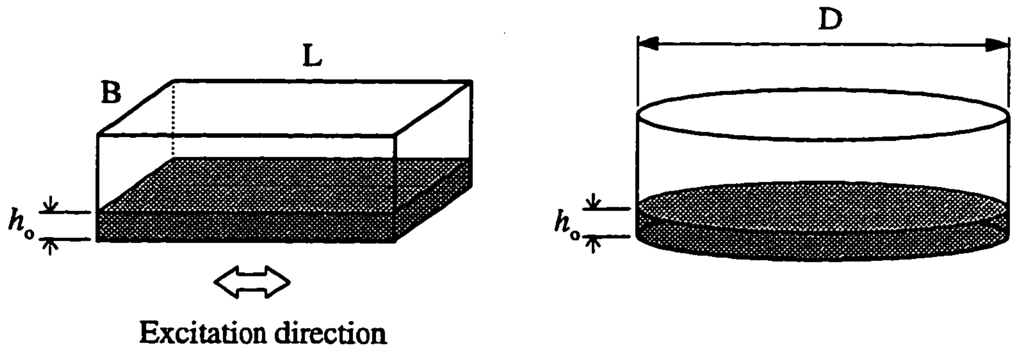

Figure 2.2: Rectangular and circular TLD configurations.

5) A harmonic function generator was connected to the actuator to control the motion of the actuator. The data were collected using a 16 channel data acquisition system.

6) Tank: The tanks were fabricated from clear acrylic plates. The bottom plates of the tanks are 19 mm (¾") thick. The side plates are 13 mm (½") thick for the rectangular tanks and 6 mm(¼") thick for the circular one. Water was used for these experiments. The configurations of the tanks are illustrated in Figure 2.2 and described in Tables 2.1 and 2.2.

2.1.2 Test cases

One of the primary objectives of the experimental study was to investigate the behavior of the water sloshing motion and the effects of the excitation amplitudes and frequencies, tank configurations and liquid depth on the sloshing behavior. Three different sizes of rectangular tanks and one circular tank were investigated in the study. The rectangular tank sizes were selected on the basis of previous investigations for rectangular tanks by Sun, et al. (1991) and Koh, et al. (1994). The circular tank size was selected to maintain the fundamental natural frequency of the water sloshing with the same depth of water as one of the rectangular tanks. Each tank filled with the desired level of water was excited with various amplitudes and frequencies as described in Tables 2.1 and 2.2. The data were recorded after the water sloshing motion reached the steady state.

Based on the linear wave theory (Lamb, 1932), the fundamental natural frequency of the water sloshing motion, f_w, was calculated by

$$f_w = \frac{1}{2\pi}\sqrt{\frac{\pi g}{L}\tanh(\pi\frac{h_0}{L})} \qquad \text{for a rectangular tank} \qquad (2.1)$$

Table 2.1: Data for the experimental investigations of rectangular tanks.

Tank Size		*Water Depth* h_0 *(mm)*	*Water Depth Ratio* ε	*Natural Freq.* f_w *(Hz)*	*Excitation Amplitude*	
Length *L* *(mm)*	*Width* *b* *(mm)*				*A* *(mm)*	*A/L*
335	203	9.6	0.029	0.457	10,20,40	.030 - .119
335	203	15	0.045	0.571	2.5,5,10,20,30	.007 - .119
590	335	15	0.025	0.325	2.5,5,10,20,30,40	.004 - .068
590	335	22.5	0.038	0.397	2.5,5,10,20,30,40	.004 - .068
590	335	30	0.051	0.458	2.5,5,10,20,30,40	.004 - .068
590	335	45	0.076	0.558	20	.034
900	335	30	0.033	0.301	2.5,5,10,20,30,40	.003 - .044
900	335	40	0.044	0.347	2.5,5,10,20,30,40	.003 - .044
900	335	55	0.061	0.406	10,20	.011 - .022
900	335	71	0.079	0.459	2.5,5,10	.003 - .011

Table 2.2: Data for the experimental investigations of circular tanks

Tank Diameter *D* *(mm)*	*Water Depth* h_0 *(mm)*	*Water Depth Ratio* ε	*Natural Freq.* f_w *(Hz)*	*Excitation Amplitude*	
				A *(mm)*	*A/D*
690	15	0.022	0.325	10,20,40	.014 - .058
690	22.5	0.033	0.397	10,20,40	.014 - .058
690	30	0.043	0.458	2.5,5,10,20,30, 40	.004 - .058
690	40	0.065	0.558	2.5,5,10	.004 - .014

and $$f_w = \frac{1}{2\pi}\sqrt{\frac{1.17\pi g}{D}\tanh\left(\frac{1.17\pi h_0}{D}\right)} \quad \text{for a circular tank} \qquad (2.2)$$

where g is gravity acceleration, L and D are the length and the diameter of the tank, respectively, and h_0 is the undisturbed water depth as illustrated in Figure 2.2.

2.2 Characteristics of water sloshing motion in rectangular tanks

In presenting the experimental results, several key parameters will be used. These are defined as follows:

The wave height, η, is defined as the water surface elevation from the undisturbed state. In the experiments, it was measured by wave gages near the end wall, at the mid-tank (when possible) and at the middle of the side wall (for the circular tank only). The quantity is nondimensionalized by dividing by the undisturbed water depth, h_0, as

$$\eta' = \frac{\eta}{h_0}. \qquad (2.3)$$

The base shear force, F_w, is defined as the reaction force of the water tank created by water sloshing motions induced by the shaking table movement. In this analysis, the measured base shear force was obtained by subtracting the inertia force of the tank from the total force measured by the loadcell to identify the force due to water sloshing motion only. In order to eliminate the undesirable high-frequency system noise, which is always present in the laboratory data, a low-pass filter was applied to the measured data. The applied low-pass filter will be discussed later in this section. The base shear force is nondimensionalized as

$$F_w' = \frac{F_w}{m_w \omega^2 A} \qquad (2.4)$$

where m_w is the mass of the water in the tank, ω is the excitation angular frequency of the shaking table, A is the shaking table excitation amplitude and the product $m_w\omega^2 A$ is the maximum inertia force of the water mass treated as a solid mass.

The amount of energy dissipation per cycle is an important concern for vibration control. As will be seen in the interaction model of Equation (4.1), the base shear force, F_w, generated by the water sloshing motion resists the excitation motion. Therefore, a measure of this force in dissipating energy is critical to this investigation. The energy dissipation per cycle, E_w, is defined as the work done by the base shear force during one cycle of the shaking table motion. This quantity is represented by the area of force-displacement (F_w - x_s) loop which can be calculated by

$$E_w = \int_{T_s} F_w \, dx_s \tag{2.5}$$

where T_s is the period of the shaking table motion and x_s is the shaking table displacement. The energy dissipation per cycle is nondimensionalized as

$$E_w' = \frac{E_w}{\frac{1}{2} m_w (\omega A)^2} \tag{2.6}$$

where $m_w(\omega A)^2 / 2$ is the maximum kinetic energy of the water mass treated as a solid mass. In the next section, an examination of these parameters is presented for the experimental cases.

In the data analyses, a low-pass filter[1] was employed to eliminate the high-frequency system noise or to separate each frequency component of waves. The natural fundamental frequency of the empty tank system which comprises the empty tank, the loadcell and the mounting system was identified at approximately 10 Hz. The noise from the shaking table

---

[1] Zero-phase forward and reverse digital filtering technique was employed using 5th order low-pass digital Butterworth filter. Refer to Matlab commands "BUTTER" and "FILTFILT" in signal processing toolbox.

system was measured at much higher frequencies. To eliminate the high-frequency system noises, the cut-off frequency of the low-pass filter must be set to a lower value than 10 Hz: e.g., the cut-off frequency was set to 5 Hz for the loadcell-measured base shear data along the excitation direction. For shallow water in a rectangular tank, the natural frequencies of each mode of the sloshing motion can be expressed as

$$f_n \approx nf_1 \tag{2.7}$$

where the subscripts indicate the mode number and f_1 is the fundamental natural frequency that can be calculated from Equation (2.1). To identify the effect of each mode of water sloshing motions, it is necessary to filter out all frequency components higher than the designated frequency. This filter-out was done by adjusting the cut-off frequency of the low-pass filter to a desired value: e.g., to obtain the data including up to n^{th} mode, the cut-off frequency of the low-pass filter was set to (n+0.5) times the fundamental natural frequency, i.e., *cut-off frequency* = (n+0.5) f_1.

2.2.1 Time history responses of water sloshing motion at steady-state for harmonic excitation

Figure 2.3 shows the sample time history responses of the steady-state water sloshing motions for the rectangular tank of length L = 590 mm, water depth h_0 = 30 mm and excitation amplitude A = 20 mm at the harmonic base excitation frequency ratios β = 0.7, 1.0, 1.2 and 1.4, respectively. The excitation frequency ratio in the horizontal axis is defined as

$$\beta = \frac{f_e}{f_w} \tag{2.8}$$

where f_e is the shaking table excitation frequency and f_w is the fundamental natural frequency of water sloshing calculated with Equations (2.1) or (2.2). In the figure, η_1' and η_2' are the nondimensional wave heights near the end wall and at the middle of the tank, respectively. F_{wx} and F_{wy} are the base shear force measured along and across the direction

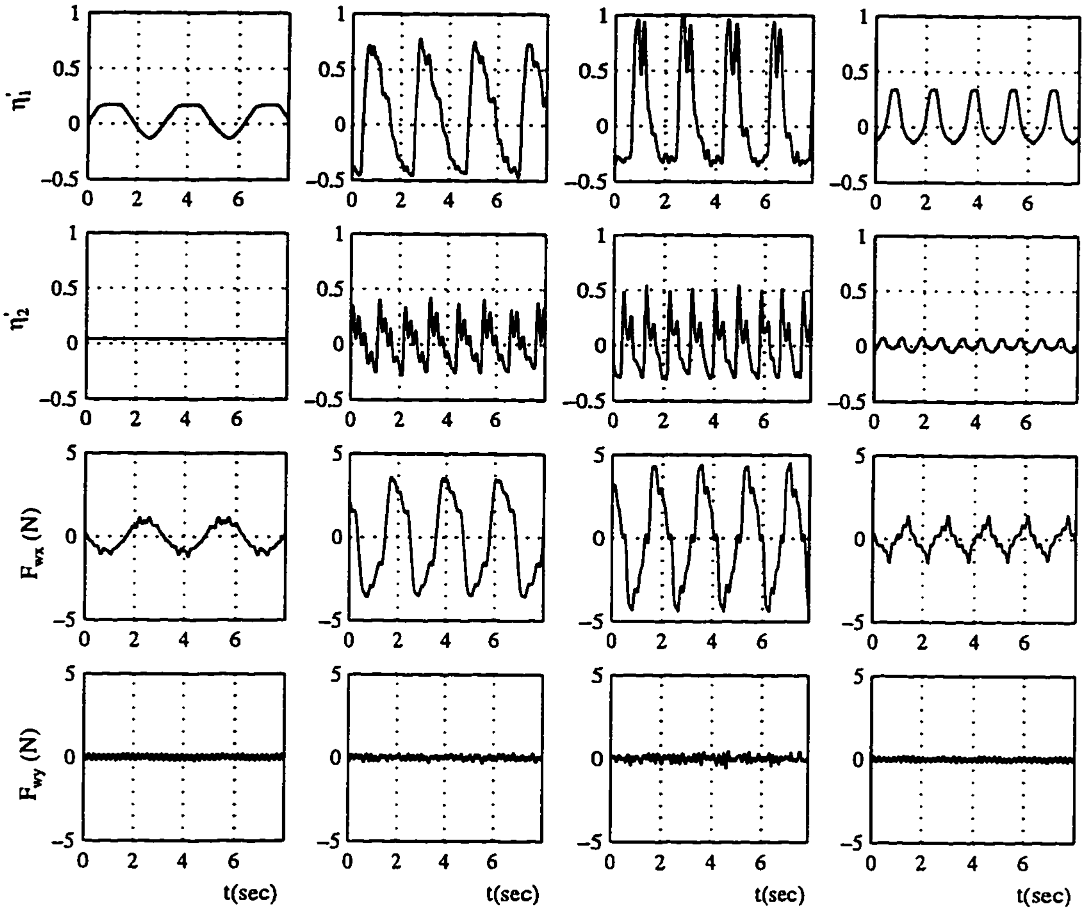

β=0.7 β=1 β=1.2 β=1.4

Figure 2.3 Sample time histories of water sloshing motions in the shaking table tests for the case of the tank with length L=590 mm, water depth h_0=30 mm, and excitation amplitude A=20 mm; the water surface elevation at the end wall η_1' and at the mid-tank η_2' and the base shear forces F_{wx} and F_{wy} in the direction of along and across excitation, respectively. β is the excitation frequency ratio.

of excitation, respectively. The raw data measured with the loadcell contain system noise. As will be discussed in Section 2.2.3, contribution of the frequency-components higher than 5 Hz on the wave motion is not significant and can be ignored. Therefore, a low-pass filter with cut-off frequency of 5 Hz was applied to the raw data of F_{wx} to eliminate the system noise. The raw data of F_{wy} are filtered by a low-pass filter with cut-off frequency of 10 Hz. At the excitation frequency ratio $\beta = 0.7$, small and smooth waves develop. At higher excitation frequency ratios β of 1.0 and 1.2 which are near the fundamental natural frequency of the TLD, strong waves develop and wave breaking occurs. In this range of excitation frequencies, higher-frequency waves riding on the primary wave appear in the wave motion. The wave motion dramatically decreases at $\beta = 1.4$.

Figure 2.4 presents the steady-state time history responses of the water surface elevations at the end wall, η_1', for the case of the tank with length L = 590 mm and water depth h_0 = 30 mm at various excitation frequencies for the excitation amplitudes A = 10, 20 and 40 mm, respectively. Wave breaking was apparent over a wide range of frequencies for each excitation amplitude case. High-frequency waves are evident in the wave motions. The high-frequency components of the wave decrease at larger amplitude excitation. The wave shapes show significant irregularities. The irregularities become more significant as the excitation amplitude increases and are taken into account in the data analyses. It is apparent that the water sloshing motion changes depending on the excitation amplitude and frequency.

Figure 2.5 illustrates the loadcell-measured base shear force due to water sloshing motions, F_w, for the same cases as Figure 2.4. The irregularities previously observed in the wave height measurements are not significant for the base shear force data. The influence of high-frequency waves is less significant on the base shear force than on the wave height. The high-frequency waves decrease as the excitation amplitude increases.

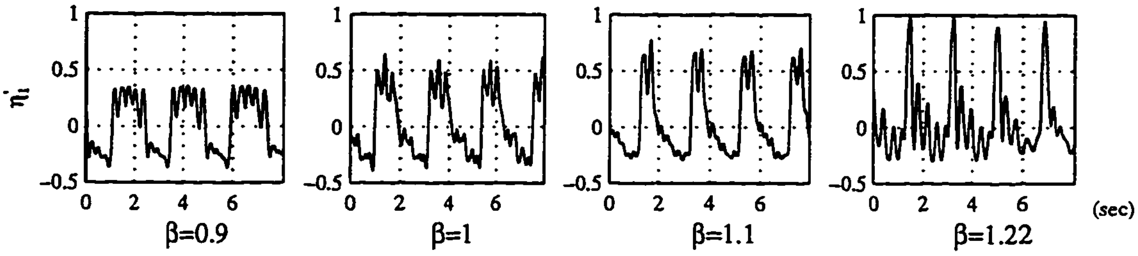

(a) A = 10 mm

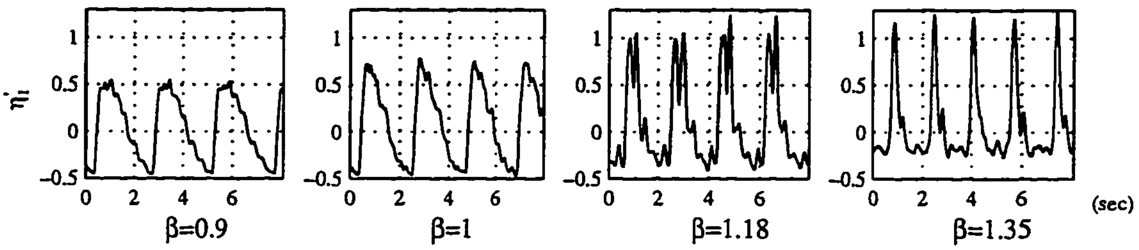

(b) A = 20 mm

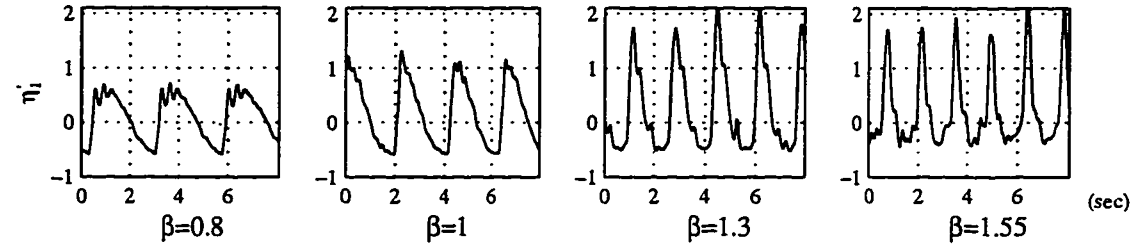

(c) A = 40 mm

Figure 2.4 Sample time histories of the nondimensional wave heights for the steady-state wave motion at various excitation frequencies for the cases of the tank with length L = 590 mm, water depth h_0 = 30 mm and excitation amplitude A = 10, 20 and 40 mm, respectively.

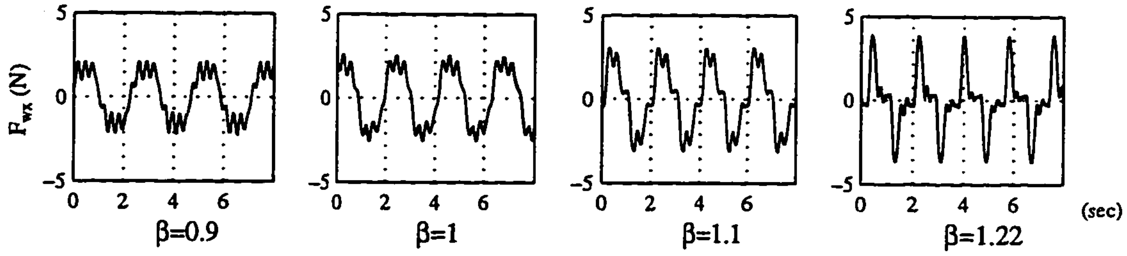

(a) A = 10 mm

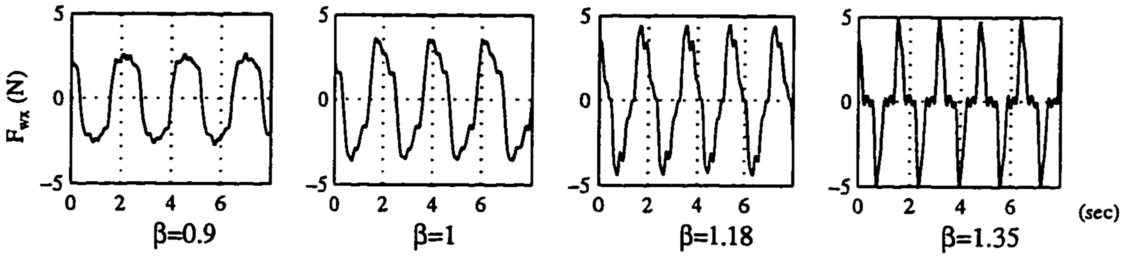

(b) A = 20 mm

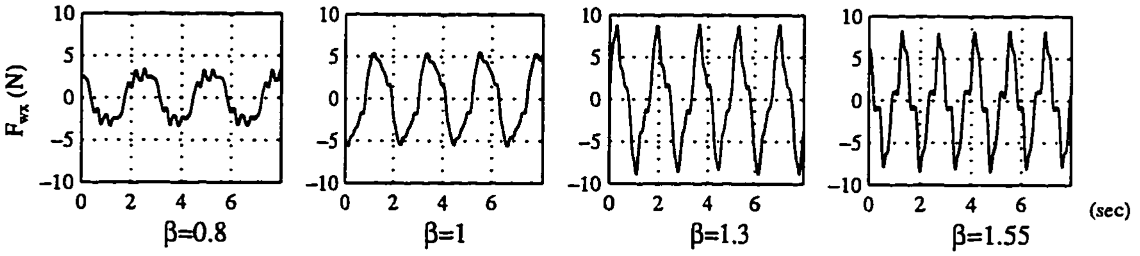

(c) A = 40 mm

Figure 2.5 Sample time histories of the measured base shear force in the x-direction for the same conditions as Figure 2.4.

Figure 2.6 contains plots of the base shear force vs. the shaking table displacement (F_w-x_t loops) for the same cases as in Figure 2.5. The dashed lines indicate the base shear forces including only the fundamental mode of water sloshing. The solid lines indicate the base shear forces including higher modes up to 5th mode. The effects of the higher modes of water sloshing motions on the time history base shear forces can be determined by comparing these two curves. The higher modes change the time history of the magnitude of the base shear forces. However, the amount of the energy dissipation per cycle which is calculated by the area inside the loop does not change significantly by the higher modes. For example, for the sweep frequency cases of the tank with length L=590 mm, water depth h_0 = 30 mm and excitation amplitude A = 20 mm, the difference in the energy dissipation using the two representations is on average about 2 %. As mentioned in Chapter 1, the energy dissipation capacity is a measurement of the performance of tuned liquid dampers. The magnitude of the base shear force $|F_w|$ and its phase lag ϕ from the shaking table displacement are two major factors determining the area inside the contour. The time history magnitudes of the base shear forces during one cycle can be most accurately represented by the RMS values.

2.2.2 Frequency responses of water sloshing motion

As observed in the study of time history responses in the previous section, the characteristics of water sloshing in the tank depend on the base excitation amplitude A, the tank length L, and the water depth h_0. The three primary parameters may be combined to define the secondary parameters: the linear fundamental natural frequency f_w, the base excitation amplitude in acceleration $\ddot{A}$, and the water depth ratio ε. The linear fundamental natural frequency f_w is defined in Equations (2.1) or (2.2). The base excitation amplitude in acceleration is defined as $\ddot{A} = \omega_e{}^2 A$ in which $\omega_e = 2\pi f_e = 2\pi\beta f_w$. The water depth ratio is defined as $\varepsilon = \frac{h_0}{L}$. The effects of each parameter on the water sloshing motions are investigated and discussed in this section.

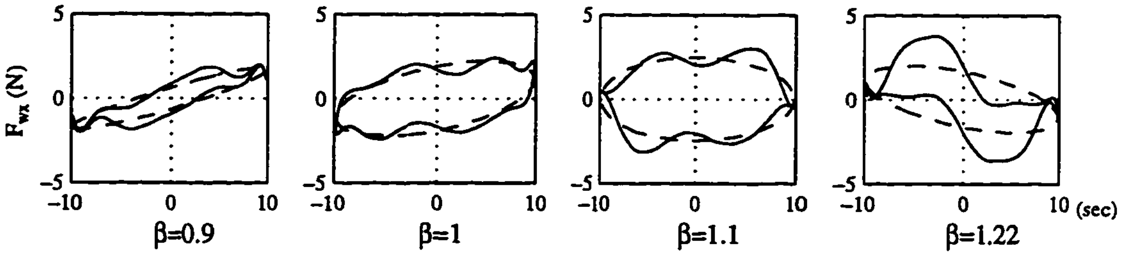

(a) A = 10 mm

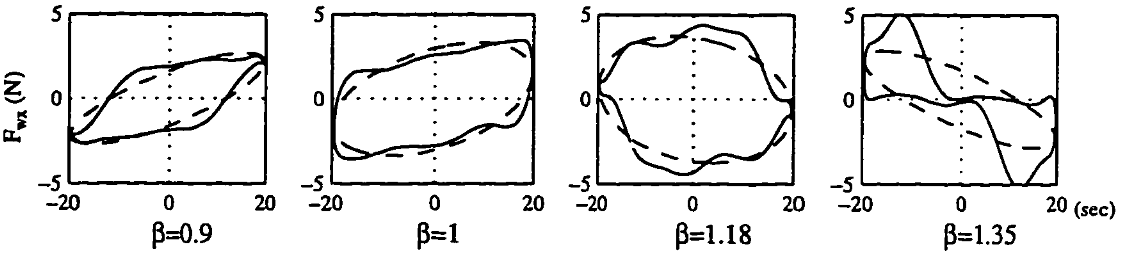

(b) A = 20 mm

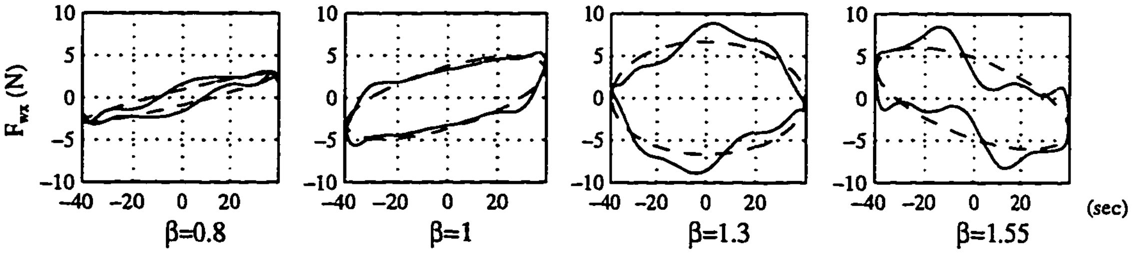

(c) A = 40 mm

Figure 2.6 Energy dissipation curves of the base shear force F_w vs. the shaking table displacement x_s for the same conditions as Figure 2.5. The dashed lines represent calculations including higher modes up to 9th mode; the solid line represents calculations only including the first mode.

To investigate the effects of the base excitation amplitude upon wave motion in the tank, the experimental cases of the tank with length $L = 590$ mm, water depth $h_0 = 30$ mm are examined under various excitation amplitudes $A = 10$, 20 and 40 mm. Figure 2.7 shows the frequency sweep plots of several nondimensional quantities: the maximum wave height near the end wall $\eta'_{1,\max}$, the maximum base shear force $F'_{w,\max}$, the phase angle ϕ of the fundamental mode of F_w from x_s, and the energy dissipation per cycle E'_w.

The maximum wave height increases as the excitation frequency increases toward the fundamental natural frequency of the TLD. The wave height reaches peak value at the excitation frequencies higher than the fundamental natural frequency, i.e., $\beta > 1.0$. This phenomenon illustrates the nonlinear characteristics of the water sloshing motions. After a gradual, fairly smooth build-up to a peak value, at a certain excitation frequency, the value of $\eta'_{1,\max}$ drops dramatically. This excitation frequency is referred to as the "jump frequency", f_{jump}, and used as a parameter representing the nonlinearity of the wave motion. The existence of the jump frequency at $\beta > 1.0$ indicates that the water sloshing motion displays a "hardening-spring type" nonlinearity. As the excitation amplitudes increase from A=10 mm to A=40 mm, the jump frequency ratios increase from about 1.22 to 1.55, where the jump frequency ratio is defined as $\beta_{jump} = \frac{f_{jump}}{f_w}$. This indicates that the nonlinearity of the water sloshing motion becomes stronger as the excitation amplitude increases. In summary, as the base excitation amplitude increases:

- The resonance frequency increases.
- The peak value of the maximum wave height increases over all frequencies.
- The magnitudes of the base shear and the energy dissipation increase. However, the nondimensional maximum base shear and the corresponding nondimensional energy dissipation per cycle decrease.

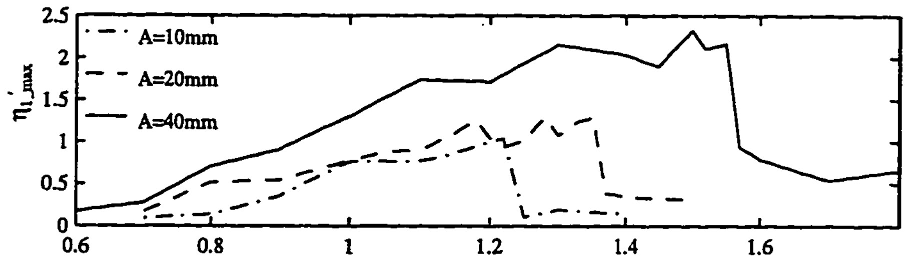

(a) Maximum wave height near end wall

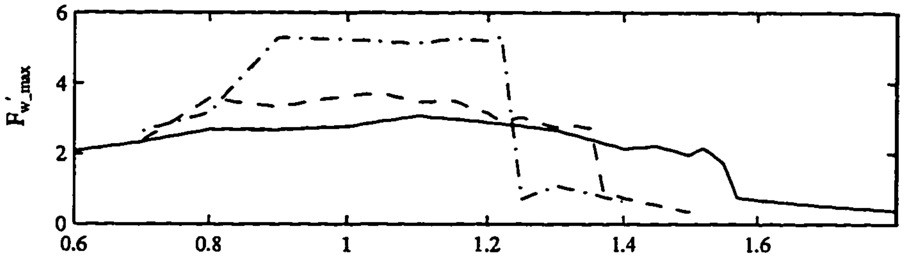

(b) Maximum base shear force

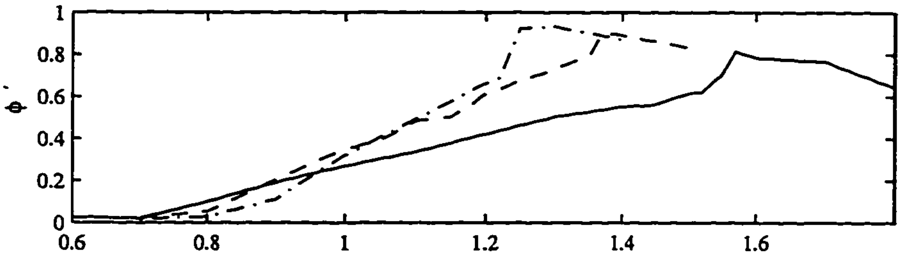

(c) Phase angle between Fw and x

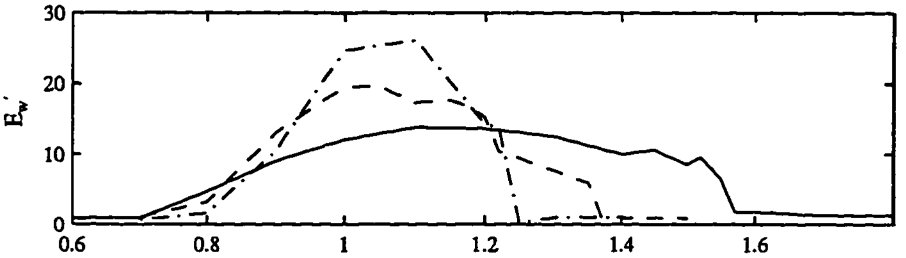

(d) Energy dissipation per cycle

Figure 2.7 Sample frequency responses of water sloshing motion in shaking table tests of the tank with length $L = 590$ mm, water depth $h_0 = 30$ mm and excitation amplitude $A =$ 10, 20 and 40 mm.

- The slope of phase angle curve decreases over sweep excitation frequencies.
- The region of excitation frequencies at which the water sloshing motion is active becomes wider.

Figure 2.8 presents two sweep frequency plots of the maximum wave heights at the end wall of the tank $\eta'_{1,\max}$ to investigate the effect of the water depth h_0 upon the water sloshing motion in the tank. The two primary parameters A and L are fixed while the water depth h_0 varies. Figure 2.8(a) shows the frequency responses of the tank with length $L = 590$ mm with water depth $h_0 = 15, 22.5, 30$ and 45 mm respectively under the excitation amplitude $A = 20$ mm. Figure 2.8(b) presents the same plots of the tank with length $L = 900$ mm with water depth $h_0 = 40$, 55 and 71 mm under the excitation amplitude $A = 10$ mm. Although slight variations in the shape and magnitude of the curves are observed, the water depth does not significantly influence the water sloshing motion in the range of selected experimental cases.

Figure 2.9 contains the sweep frequency plots of the maximum wave heights at the end wall of three tanks with lengths $L = 335$, 590 and 900 mm, respectively for excitation amplitude $A = 10$ mm. The water depth of each tank was determined such that the linear fundamental natural frequencies f_w of the tanks become identical: in this case $f_w = 0.458$ Hz. It is observed that the smaller tank with the shallower water depth develops the stronger wave motion and the higher jump frequency. Because the effect of the water depth is not significant as observed in Figure 2.8, the differences in three curves reflect mainly the influence of the tank length L on the wave motion. Apparently, the length of the tank influences the water sloshing motion significantly.

The data shown in Figures 2.7 through 2.9 indicate that the water sloshing motion in the tank is significantly influenced by the excitation amplitude and the tank length. The underlying physical phenomenon is described in the following paragraphs.

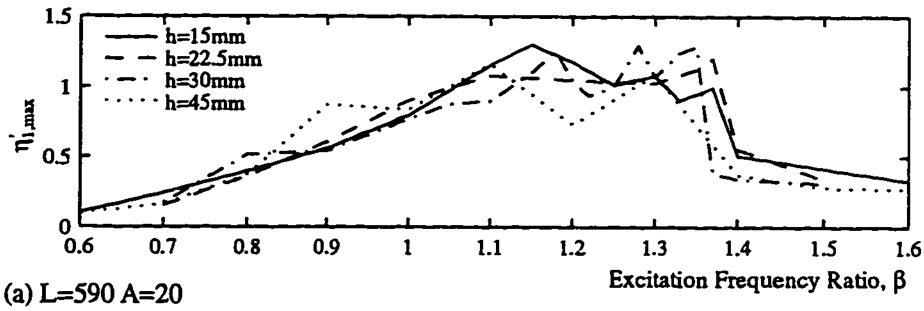

(a) L=590 A=20

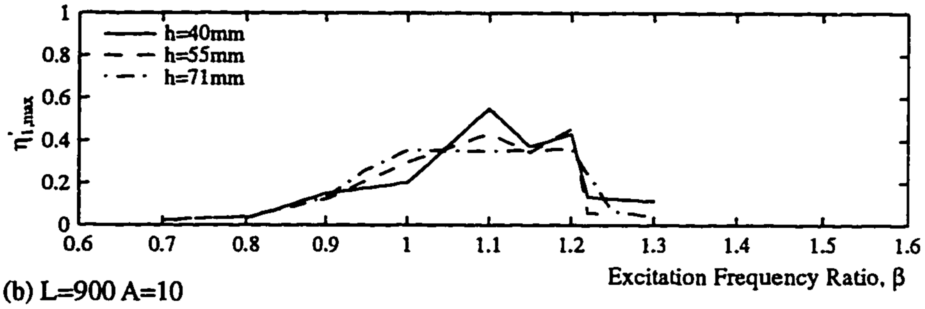

(b) L=900 A=10

Figure 2.8 Sample frequency responses for the selected experimental cases to investigate the effect of water depth h_0 on the water sloshing motion.

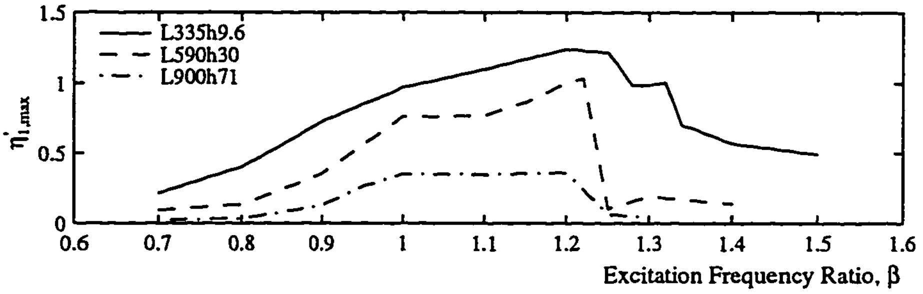

Figure 2.9 Sample frequency responses for the selected experimental cases to investigate the effect of tank length L on the water sloshing motion.

Based on the shallow-water wave theory, the propagation speed, S, of a smooth wave may be expressed as

$$S = \sqrt{g(h_0 + \eta)} = \sqrt{gh_0(1+\eta')} \tag{2.9}$$

where $\eta' = \frac{\eta}{h_0}$. Because the wave length L_0 of the fundamental mode of sloshing motion in a rigid tank with length L can be calculated by $L_0 = 2L$, the fundamental frequency of the tank, f, is calculated by

$$f = \frac{S}{2L} = \frac{\sqrt{gh_0}}{2L}\sqrt{1+\eta'} \ . \tag{2.10}$$

Considering the "linear" fundamental natural frequency of the shallow-water wave based on Equation (2.1) as

$$f_w \cong \frac{\sqrt{gh_0}}{2L} \tag{2.11}$$

the ratio of the real fundamental natural frequency to the linear fundamental natural frequency is approximated by

$$\frac{f}{f_w} \cong \sqrt{1+\eta'} \ . \tag{2.12}$$

Equation (2.12) indicates that the natural frequency of the shallow-water wave is a function of the wave height. Because the wave height is related to the excitation amplitude A and the tank length L as observed in Figures 2.7 through 2.9, the frequency shift ratio is dependent on these two parameters. In other words, the nonlinearity of the shallow-water sloshing is, at least, a function of A and L.

As mentioned previously, the jump frequency can be used as a representation of the nonlinearity of the water sloshing motion. Figure 2.10 shows the relationship between the jump frequency and the two parameters A and L. In this plot, the parameter "nondimensional excitation amplitude" is introduced, which combines the two parameters in the form of

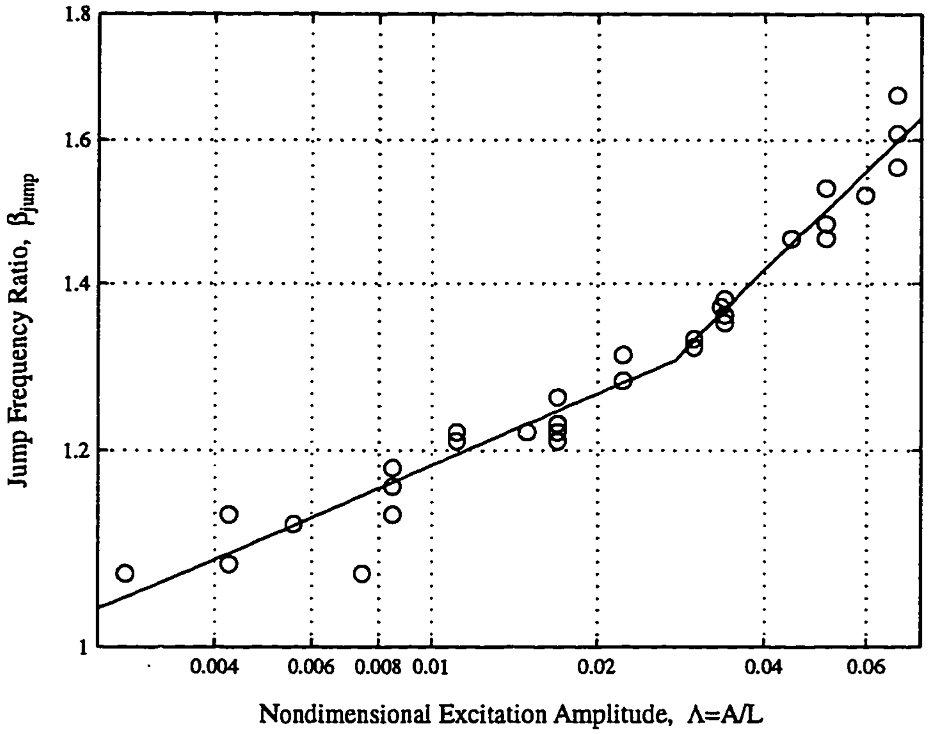

Figure 2.10 Relationship between the jump frequency ratio and the nondimensional excitation amplitude based on experimental results.

$$\Lambda = \frac{A}{L}\,. \tag{2.13}$$

The values of the jump frequency ratio β_{jump} for all experimental cases described in Table 2.1 were plotted against the nondimensional excitation amplitude. These two parameters exhibit clear correlation. The approximate functional relationship between these two parameters change slope at $\Lambda \approx 0.03$ in this log-log scale plot. The regression line of β_{jump} on Λ in each region is determined using the least squares method as

$$\begin{aligned} \beta_{jump} &= 1.85\Lambda^{0.095} \quad \textit{as} \quad \Lambda \le 0.03 \quad \textit{and} \\ \beta_{jump} &= 2.89\Lambda^{0.222} \quad \textit{as} \quad \Lambda \ge 0.03\,. \end{aligned} \tag{2.12}$$

These equations reflect that in the region of larger excitation amplitude, approximately $\Lambda > 0.03$, the slope of the regression line increases. This means that the rate of change in the jump frequency becomes faster in this excitation amplitude range. This result implies that the nonlinearity of the water sloshing motion changes more rapidly in this region.

2.2.3 Higher modes of water sloshing motion

As discussed in the previous section, the higher modes of water sloshing are apparent in the time history responses of the wave height and the base shear force near the resonance frequency. The effects of the higher modes of the water sloshing motion on the energy dissipation plots have been also discussed. In this section, the effects of the higher modes are systematically investigated using the frequency response plots of the experimental results.

Figure 2.11 presents the results of the experimental investigation for the tank with length L=590 mm, water depth h_0 = 30 mm and excitation amplitude A = 20 mm. It contains the plots of $\eta'_{\max}$, $F'_{w,\max}$, $F'_{w,rms}$ and E'_d filtered with four different cut-off frequencies such that each curve includes only the low frequency components up to the designated mode. By comparing these curves, the effects of the higher frequency components upon the water sloshing motions are summarized as follows:

- The effect gradually increases as the excitation frequency increases up to jump frequency.
- The effect is most significantly related to $\eta'_{\max}$. It is less significantly related to F'_w and negligible for E'_d.
- The effect is less for RMS values than peak values of η and F_w.
- The contribution of the frequency components higher than 9th mode on the wave motion is not significant and can be ignored.

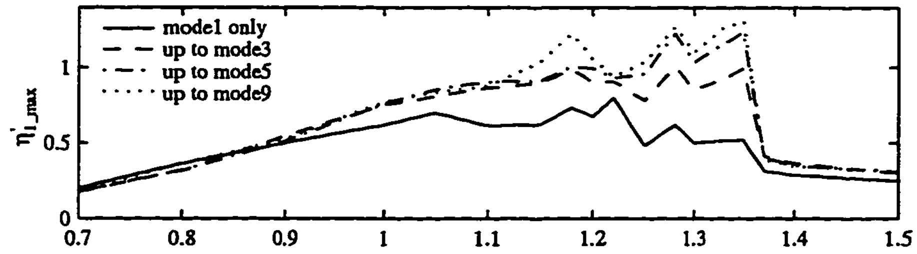

(a) Maximum wave height near end wall

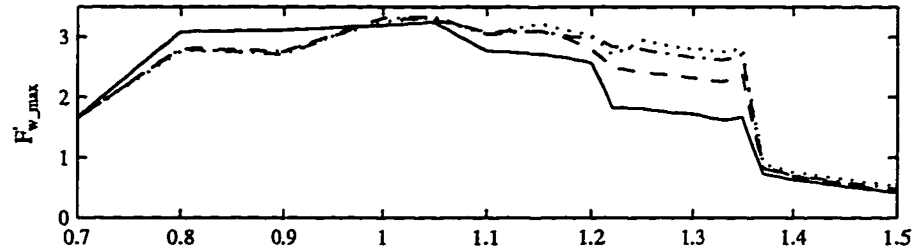

(b) Maximum base shear force

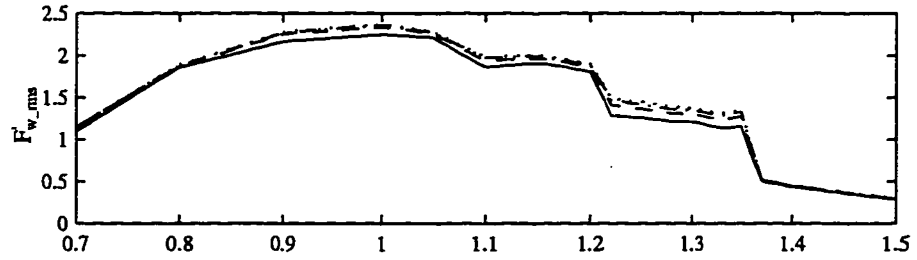

(c) RMS base shear force

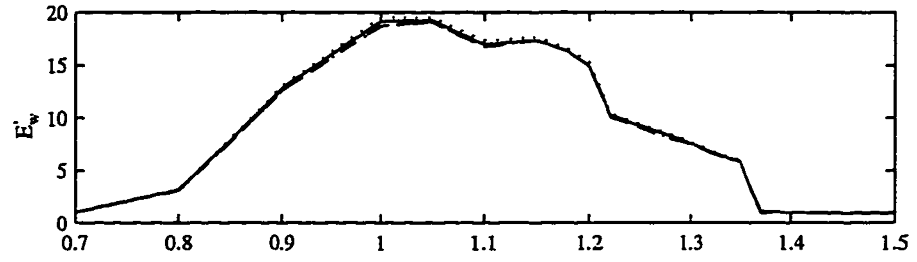

(d) Energy dissipation per cycle

Figure 2.11 The effects of higher frequency components of the water sloshing motion upon its frequency responses for the tank with length L = 590 mm, water depth h_0 = 30 mm and excitation amplitude A = 20 mm.

- The higher frequency components of the water sloshing motion do not contribute to the energy dissipation capacity of the TLD. Therefore, performance of the TLD can be accurately predicted by considering only the fundamental mode of the water sloshing motion.

2.2.4 Calculation of the base shear force based on the wave height near the end walls of rectangular tank.

The TLD generates a hydrodynamic force due to the water sloshing motion. For small amplitude excitation, it is common practice to approximate the hydrodynamic force by the hydrostatic pressures on the tank end walls. In large amplitude excitation, the wave breaks in a certain frequency region. The approximations for hydrostatic pressure and ignoring the vertical acceleration of the water particles must be investigated.

As shown in Figure 2.11, the true water sloshing responses can be closely represented by including low frequency components up to 9th mode. Because the 9th mode frequencies of the tanks for all experimental cases are lower than 10 Hz at which the system noises exist, the low pass filter with cut-off frequency between the 9th mode frequency and 10 Hz was applied to the experimental raw data to eliminate the system noise.

Assuming hydrostatic pressure on the tank end walls and ignoring the vertical acceleration of the water particles, the hydrodynamic force of the TLD, $F_{\eta l}$, hereinafter the linear hydrodynamic force, can be calculated by

$$F_{\eta 1} = \frac{1}{2}\rho g b (h_l^2 - h_r^2) \tag{2.15}$$

where ρ is the water density; g is the acceleration due to gravity; b is the tank width and h_l and h_r are the water surface elevations at the end walls.

Figure 2.12 presents the frequency responses of the tank with length L=590 mm, water depth h_0=30 mm and excitation amplitude A=20 mm. The solid curves represent the

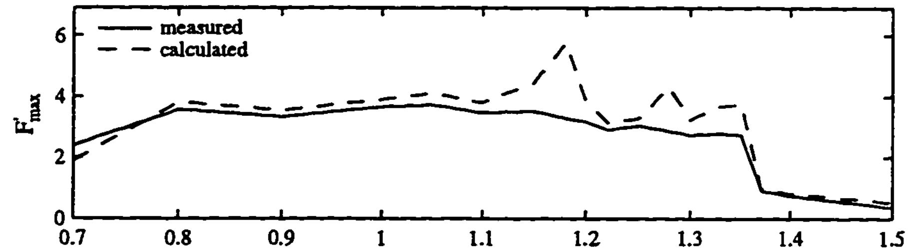

(a) Maximum base shear force

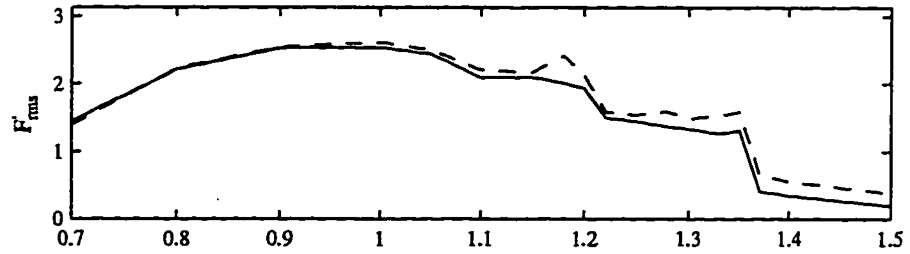

(b) RMS base shear force

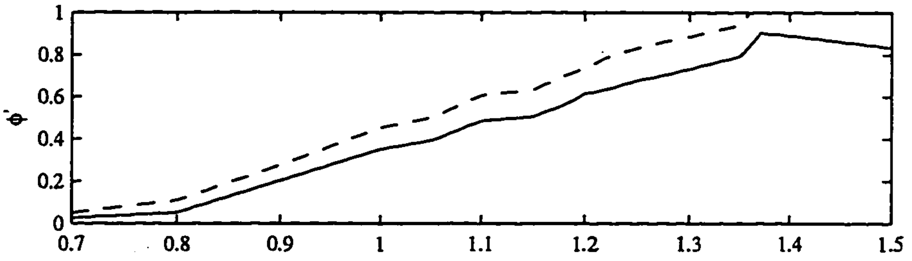

(c) Phase angles between F and x_s

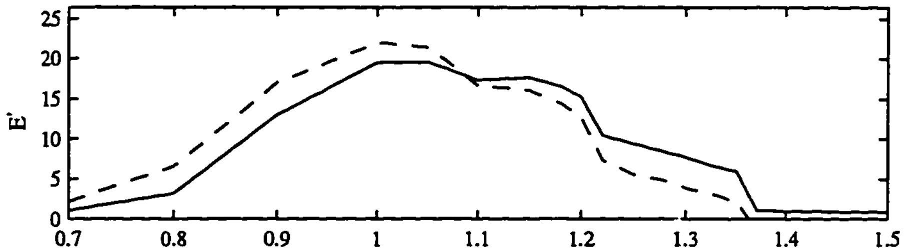

(d) Energy dissipation per cycle

Figure 2.12 Comparison of the base shear force, F_η, calculated from the wave height and the one measured by the load cell, F_w for the tank with length L=590mm, water depth h_0=30mm and excitation amplitude A=20mm.

base shear force, F_w measured by the loadcell. The dashed curves indicate the linear hydrodynamic forces, F_η calculated from the measured wave heights at the end wall of the tank using Equation (2.15). Both data were filtered to retain the lower frequency components up to the 9th mode. The nondimensional values of the maximum and RMS base shear forces, the phase angle of the two forces from the shaking table displacement and the energy dissipation per cycle by the two forces are plotted vs. sweep frequency.

In the plot for the maximum values of the two forces, significant discrepancies are observed in both shape and magnitude, particularly near the resonance frequency. These discrepancies can be explained as follows: After the peak wave hits the end wall, the remaining bulk mass of the water runs up the end wall. Although this latter run-up does not develop significant hydraulic pressure, the calculated force derived from wave height alone reaches its maximum value. Consequently, the maximum calculated force may be exaggerated. Because the duration of the wave run-up is short, the discrepancy is reduced in the plots for the RMS of the forces. Plots for the RMS values of two forces are more similar. However, the discrepancy in the magnitude of the damping forces near the resonance frequency is still about 10 to 20 %.

The phase angles of F_η lag behind those of F_w over the entire range of sweep frequencies. The differences fall within the range of less than 0.15π. This discrepancy is assumed to reflect that the maximum value of F_η is captured after maximum F_w was measured because of the run-up discussed previously and the distance of the wave gage from the end wall. The energy dissipation plots reflect the combined effects of the magnitudes and the phase angles of the two forces.

2.3 Water sloshing motion in circular tanks.

The shaking table experiments were conducted for a circular tank with diameter D of 690 mm. The experimental cases are described on Table 2.2. The experimental cases for the circular tank were selected to maintain the same fundamental natural frequency as the rectangular tank with length L=590 mm and the same water depth.

Figure 2.13 presents sample time history responses of the water sloshing motions at steady-state of the tank with diameter D=690 mm, water depth h_0=30 mm and excitation amplitude A=20 mm at various base excitation frequencies. The measured quantities are the same as for the corresponding rectangular tank cases (Figure 2.3) except η_3' is the nondimensional wave height at the middle of the side wall. It is apparent that the water sloshing motion depends on the excitation amplitude and frequency.

Figure 2.14 shows the frequency responses of the water sloshing motions in the circular tanks for the same cases under the base excitation amplitude A = 10, 20 and 40 mm. These cases correspond to the rectangular tank cases presented in Figure 2.7. It is observed that the shapes and the magnitudes of the wave heights, the base shear forces and the energy dissipation per cycle for the circular TLD are similar to those of the corresponding rectangular TLD.

Although the wave behavior in a circular tank is more complex than in the rectangular one, in practice, it is often analyzed as an equivalent rectangular tank. The observation of the similarity in trends of the water sloshing motion in a circular tank and those in the comparable rectangular tank justifies the use of this approximation method for the circular TLD.

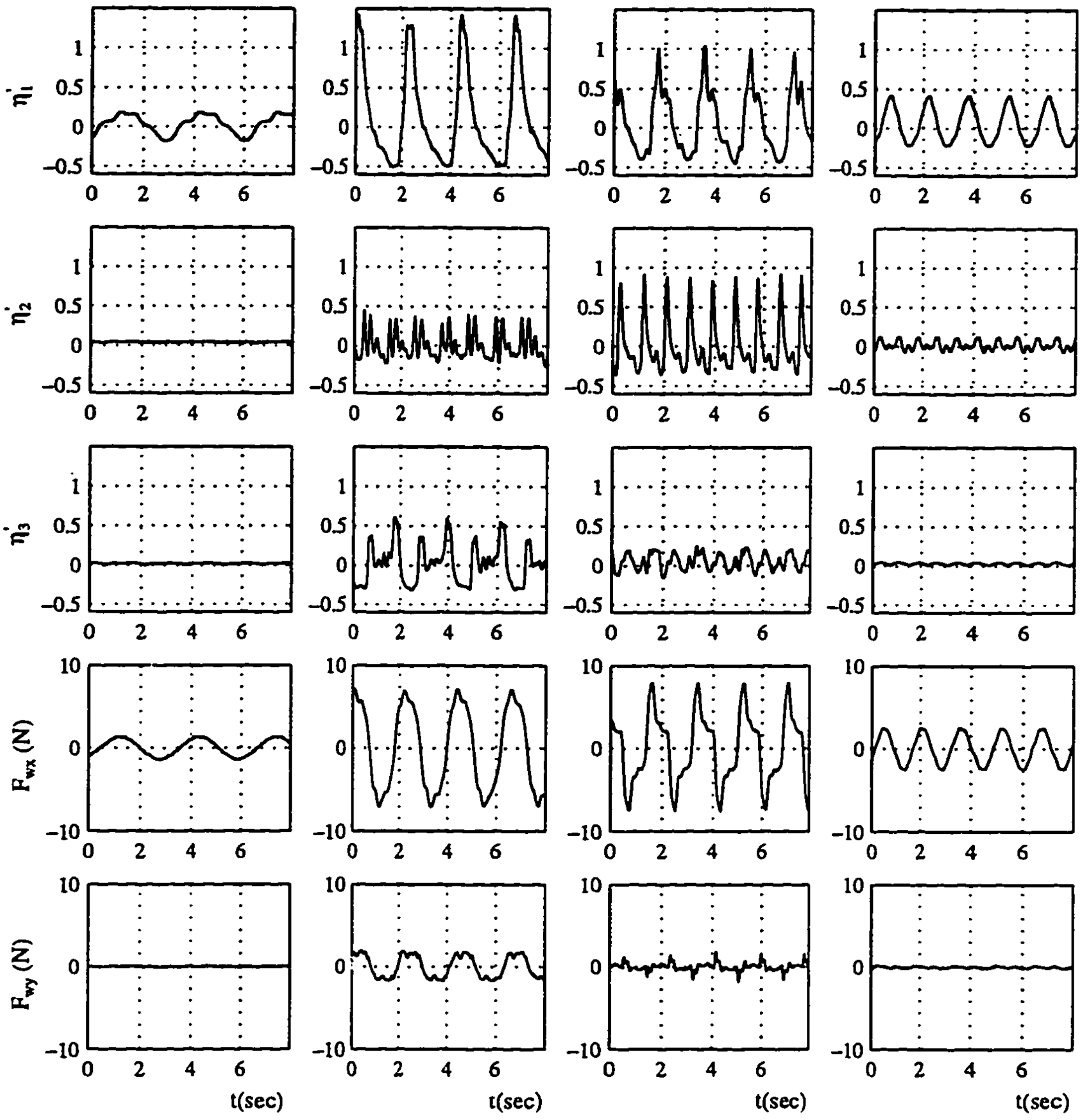

β=0.7 β=1 β=1.2 β=1.4

Figure 2.13 Sample time history responses of water sloshing motion for the circular tank with diameter D=690mm, water depth h_0=30mm and excitation amplitude A=20mm.

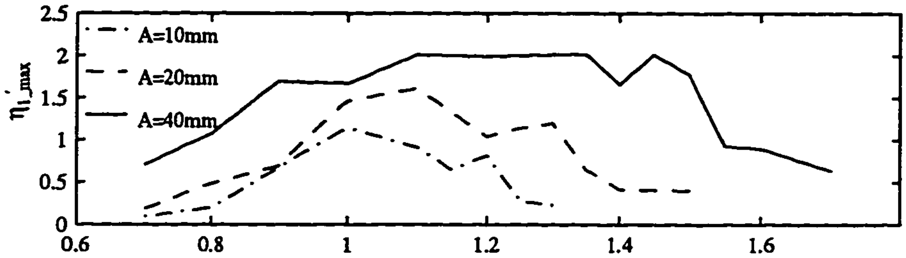

(a) Maximum wave height near end wall

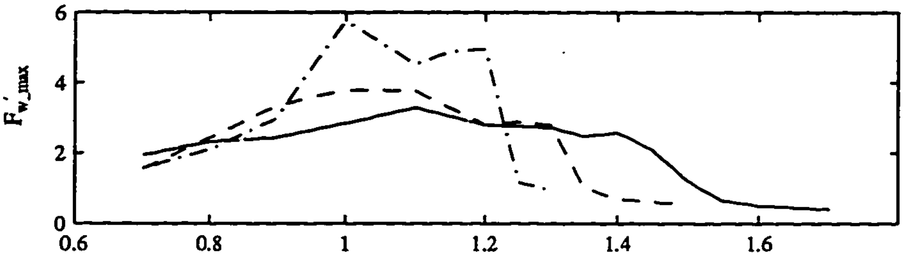

(b) Maximum base shear force

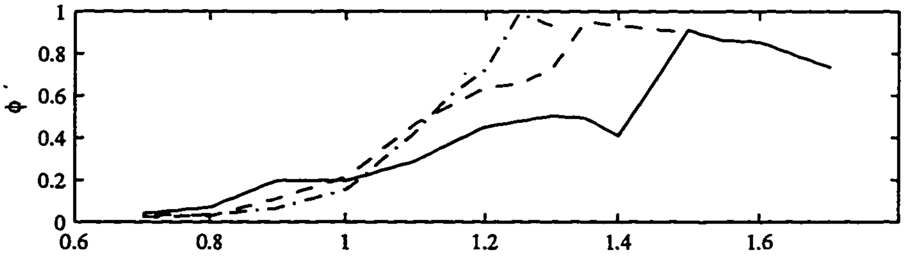

(c) Phase angle between Fw and x

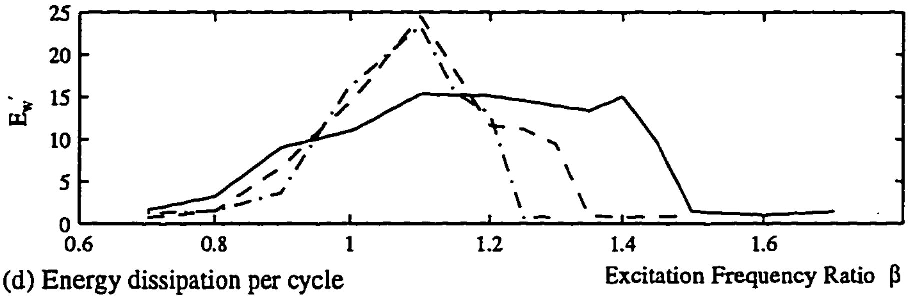

(d) Energy dissipation per cycle

Figure 2.14 Sample frequency responses of water sloshing motion for the circular tank with diameter D=690mm, water depth h_0=30mm and excitation amplitude A=20mm.

CHAPTER 3

NUMERICAL MODELS OF THE TLD

Two numerical models were investigated. The first is an equivalent TMD model developed based on the experimental results. This model incorporates the nonlinear stiffness and damping characteristics of the TLD, and is called the "NSD model".

The second model is a fluid model based on the shallow-water wave equations characterized using the random choice method (RCM model) which was proposed by Gardarsson and Yeh (1994). A series of numerical analyses were conducted using this model to simulate the water sloshing motion in rectangular tanks. This model is evaluated by comparing the results with the experimental investigations.

3.1 NSD model - an empirically-based equivalent TMD model

The behavior of passive TMDs has been thoroughly investigated, e.g., McNamara (1977); Warburton (1980, 1981, 1982). The use of a TMD model to represent the TLD is attractive because of the body of knowledge devoted to the TMD and the similarity in the mechanisms of the TLD and TMD as described in Section 1.2. In this investigation, an equivalent TMD model that incorporates the nonlinear stiffness and damping characteristics is developed on the basis of experimental results. This model is called the "NSD model".

3.1.1 Modeling

As discussed in Section 1.2, the water mass of the TLD reacts to the structural movement in a similar manner as the mass of the TMD. The TLD exhibits its inherent damping and stiffness characteristics due to its sloshing motion. After the damping and stiffness of the TLD are quantified, the TLD can be modeled as a SDOF mass with stiffness and damping.

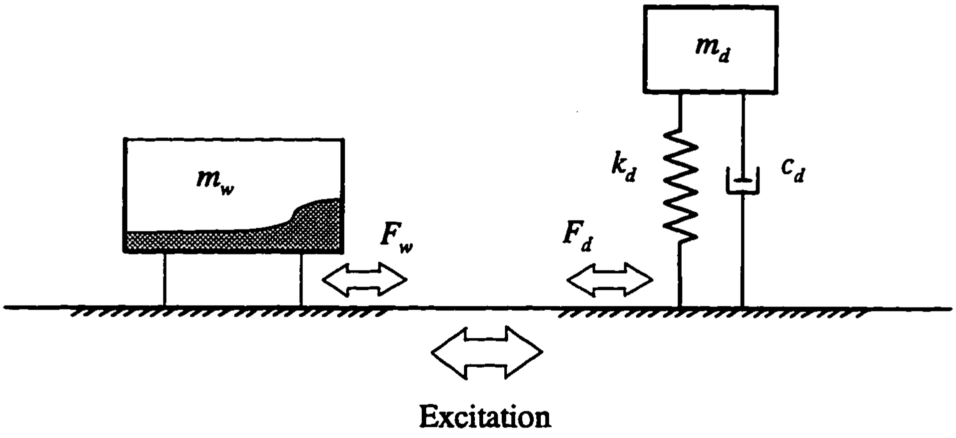

(a) TLD (b) NSD Model

Figure 3.1 An equivalent TMD model of the TLD

Figure 3.1 illustrates a TLD and the proposed equivalent TMD model as a SDOF system with stiffness and damping parameters, k_d and c_d, respectively. However, unlike the TMD which is considered as a linear system, the TLD possesses strong nonlinear characteristics as observed in the shaking table experiments and must be modeled as a nonlinear system. The stiffness and damping of the NSD model are determined such that the base shear force (or damping force) due to the TLD, F_w, and that due to the corresponding NSD model, F_d, are equivalent under the same base excitation.

The damping force is characterized by its amplitude and phase. Alternatively, the single parameter of energy dissipation per cycle, E_d, can be used to match the properties of a TLD with its equivalent TMD representation. The energy dissipation per cycle is defined by the area inside the loop of the damping force vs. the base displacement contour as described by Equation (2.5). This quantity represents the combined effects of the amplitude and the phase of the damping force on the structural motion over the period of one cycle.[1] In determining the properties of the NSD model, a comparison of the energy dissipation has advantages over a comparison of the damping forces of two systems. First, comparing one scalar quantity is more appealing. Second, as illustrated in Figure 2.11, the effect of higher modes of the water sloshing on the quantity of the energy dissipation is negligible. Therefore, in this investigation, the energy dissipation is employed as a parameter for determining model parameters.

3.1.2 Energy dissipation matching scheme

Figure 3.2 presents typical sweep frequency plots of the nondimensional energy dissipation per cycle for the TLD with length L = 590 mm, water depth h_0 = 30 mm and excitation amplitude A = 20 mm and for its corresponding NSD model. The nondimensional energy dissipation curve for the TLD (E_w', solid line) is determined from measurements of the shaking table experiments using Equations (2.5) and (2.6). The nondimensional energy dissipation for the corresponding NSD model (E_d', dashed line) is calculated using the procedure described in Appendix A.2 and summarized here. In presenting this procedure, the following parameters are used: f_e indicates the excitation frequency; f_w represents the linear fundamental natural frequency of the TLD as defined in Equation (2.1); ω_w is the linear fundamental natural angular frequency of the TLD defined by $\omega_w = 2\pi f_w$; β is the excitation frequency ratio as defined in Equation (2.8); m_w is the mass of the water in the tank; k_w is the linear fundamental stiffness of the TLD defined by $k_w = m_w \omega_w^2$; m_d, k_d and c_d are the mass, stiffness coefficient and damping coefficient of the corresponding NSD model, respectively; the critical damping ratio is defined as $c_{cr} = 2m_w\omega_w$; and the damping ratio of the equivalent TMD model, ζ, is defined by

$$\zeta = \frac{c_d}{c_{cr}} . \tag{3.1}$$

---

[1] See Appendix A.2 for the relationship of energy dissipation to the damping force in SDOF system.

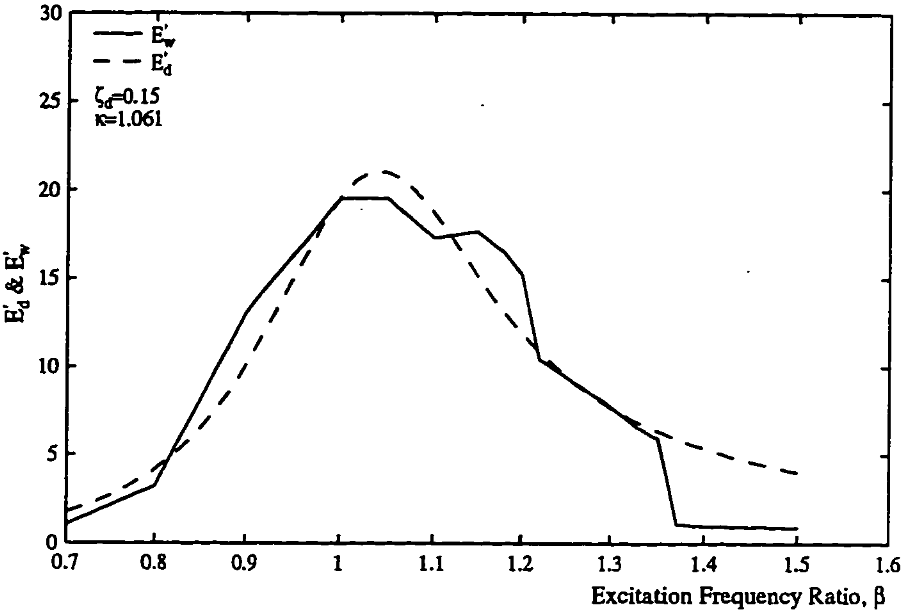

Figure 3.2 Matching scheme of the sweep frequency energy dissipation curves to obtain the stiffness hardening ratio, κ, and damping ratio, ζ_d, of the NSD model of the TLD with length L=590mm, water depth h_0=30mm and excitation amplitude A=20mm.

The stiffness hardening ratio, κ, is defined by

$$\kappa = \frac{k_d}{k_w} . \tag{3.2}$$

The frequency shifting ratio, ξ, is defined by

$$\xi = \frac{f_d}{f_w} . \tag{3.3}$$

If the NSD model shown on Figure 3.1 (b) is subjected to a harmonic base excitation with frequency ratio β, the amplitude and the phase of the damping force are expressed respectively, in nondimensional form as follows[1]

---

[1] See Equations (A.16) & (A.7) in Appendix A.

$$\left|F_d'\right| = \frac{\sqrt{(1+(4\zeta^2-1)\beta^2)^2+4\zeta^2\beta^6}}{1+(4\zeta^2-2)\beta^2+\beta^4} \tag{3.4}$$

and

$$\phi = \tan^{-1}\left(\frac{2\zeta\beta^3}{-1+(1-4\zeta^2)\beta^2}\right). \tag{3.5}$$

The nondimensional energy dissipation for the NSD model at each excitation frequency is obtained by the formula[1]

$$E_d' = 2\pi\left|F_d'\right|\sin\phi\ . \tag{3.6}$$

E_d' is fit to E_w' by the least squares method over the frequency range of high energy dissipation. In general, this matching region encompasses approximately 70 % of the peak energy dissipation. The fundamental trends of the E_d' curve for various model parameters are described in Appendix A.2.

3.1.3 Determination of the model parameters based on shaking table test results for rectangular TLDs

The matching scheme discussed in the previous section was applied to the experimental cases for rectangular TLDs to determine the stiffness and the damping coefficients of the equivalent TMD model. In general, for the case with smaller excitation amplitude, the E_w' curve becomes higher and narrower, which corresponds to lower damping and lower stiffness of the model. As the excitation amplitude becomes larger, the response curve becomes lower and wider, which leads, consequently, to higher damping and higher stiffness of the model. The specific results are tabulated in Table E.1 in Appendix E.

As discussed in Section 2.2 and illustrated in Figure 2.10, the nonlinearity of the TLD in terms of jump frequency can be expressed as a function of A and L. Sun, et al.

---

[1] See Equation (A.19) in Appendix A.

(1992) found that the nonlinearity of the TLD also depends on the parameter ε that is the ratio of water depth h_0 to the tank length L. The damping of the shallow water sloshing motion is difficult to determine analytically, especially, for wave breaking situations. However, the damping ratio of rectangular TLD under small excitation amplitude is expressed in Sun (1992) as

$$\zeta_w = \frac{\sqrt{\omega v}(1+2h_0/B+S)}{2\sqrt{2}(\eta+h_0)\omega_w} \tag{3.7}$$

which is a function of h_0. Therefore, it was assumed that the stiffness and the damping coefficients are functions of three parameters: A, L and h_0. To determine the contribution of each parameter to the nonlinearity of the TLD, the two coefficients were plotted against various combinations of these three parameters. The combination of three parameters with which the data are best correlated is the best parameter for representing the nonlinearity of the TLD. The nondimensional excitation amplitude for both coefficients (ζ and κ) was determined through an extensive searching for the best correlation as

$$\Lambda = \frac{A}{L} \; . \tag{3.8}$$

This is the same parameter for the jump frequency plot as shown in Equation (2.13).

In Figure 3.3, the variation of damping and stiffness hardening ratios of the equivalent TMD models for the experimental cases is plotted with respect to the nondimensional excitation amplitude, Λ. The damping ratios are clearly correlated with Λ over the entire range of excitation amplitude. The best fitted curve was determined using the least squares method as

$$\zeta_d = 0.52\Lambda^{0.35} \; . \tag{3.9}$$

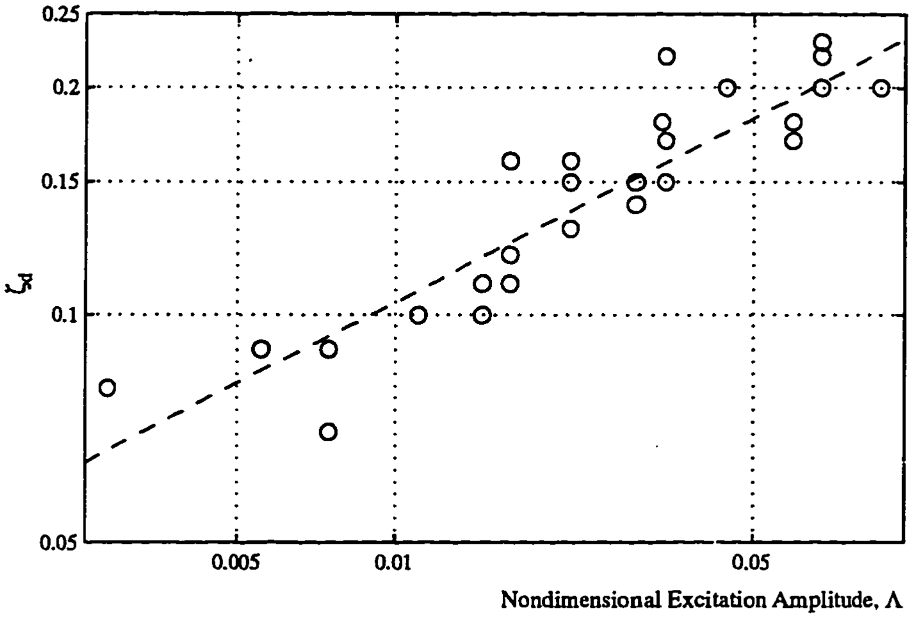

(a) Damping ratio

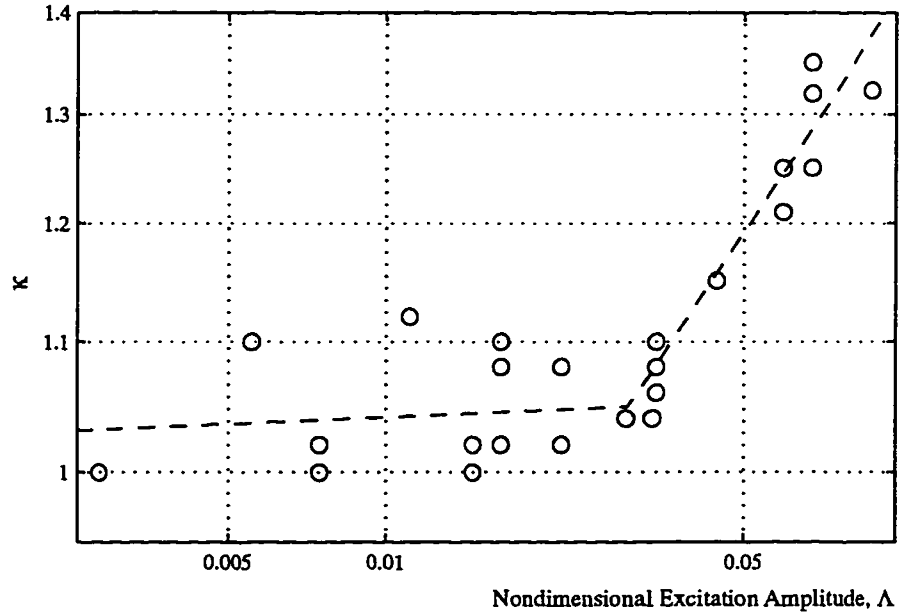

(b) Stiffness hardening ratio

Figure 3.3 The damping ratio, ζ_d, and the stiffness hardening ratio, κ, of the NSD model of the rectangular TLD determined from shaking table experiment.

For the stiffness hardening ratio of the NSD model, the figure shows two distinct regions divided at $\Lambda \approx 0.03$. In each region the slope is clearly different. This phenomenon is consistent with the observation from the jump frequency plots. The two regions are defined as the weak wave breaking region and the strong wave breaking region, respectively. The regression line in each region was determined using the least squares method as

$$\begin{aligned} \kappa &= 1.075\Lambda^{0.007} \quad \text{as} \quad \Lambda \le 0.03 \quad \text{and} \\ \kappa &= 2.52\Lambda^{0.25} \quad \text{as} \quad \Lambda > 0.03 . \end{aligned} \tag{3.10}$$

In the weak wave breaking region, the stiffness hardening ratio changes very slowly at the approximate value of 1.05. The stiffness hardening ratio changes rapidly in the strong wave breaking region. Noticing the relationship between ξ and κ as

$$\xi = \sqrt{\kappa} \ , \tag{3.11}$$

the frequency shift ratio may be expressed as

$$\begin{aligned} \xi &= 1.038\Lambda^{0.0034} \quad \text{as} \quad \Lambda \le 0.03 \quad \text{and} \\ \xi &= 1.59\Lambda^{0.125} \quad \text{as} \quad \Lambda > 0.03 . \end{aligned} \tag{3.12}$$

3.1.4 Application of the equivalent TMD model derived for rectangular TLDs to the circular TLD

Because a structure moves in many directions, the circular shape TLD may have advantages in mitigating vibration over the rectangular one. However, wave motions in the circular tank are more complex than those in the rectangular one. In practice, therefore, the circular TLD is often analyzed as an equivalent rectangular TLD, e.g., Wakahara (1993). The conversion of a circular TLD into rectangular one is made such that the fundamental natural frequency and the mass of two TLDs with the same water depth are equal. To maintain same natural frequencies of the two system, Equations (2.1) and (2.2) are set equal. The length of the equivalent rectangular TLD, L, is obtained in terms of the diameter of the circular TLD, D, as

$$L = 1.17D\,. \tag{3.13}$$

To maintain equal masses of the two systems, the width of the rectangular tank, B, is obtained by

$$B = 1.075\,L\,. \tag{3.14}$$

The matching procedures were applied to the energy dissipation curves obtained from the shaking table experiments for the circular tank with diameter D = 690 mm and various water depths. The damping ratios and the stiffness hardening ratios for each circular tank are tabulated in Table E.3 in Appendix E and plotted in Figure 3.4. From Equation (3.13) the length of the equivalent rectangular tank is found to be L = 590 mm. For comparison purposes, the results for rectangular tanks and its best fitted curves are plotted in the same figure.

In the region of weak wave breaking, i.e., $\Lambda < 0.03$, the data points are scattered from the fitted curve in the plot of stiffness hardening ratio. This discrepancy appears to reflect the phenomenon of swirling wave motion in the circular tank near the resonance excitation frequency. The swirling wave motion reduces the energy dissipation capacity.

However, overall, the NSD properties of the circular TLD are similar to those of the equivalent rectangular TLD. The result justifies the method of analysis of the circular TLD as an equivalent rectangular one.

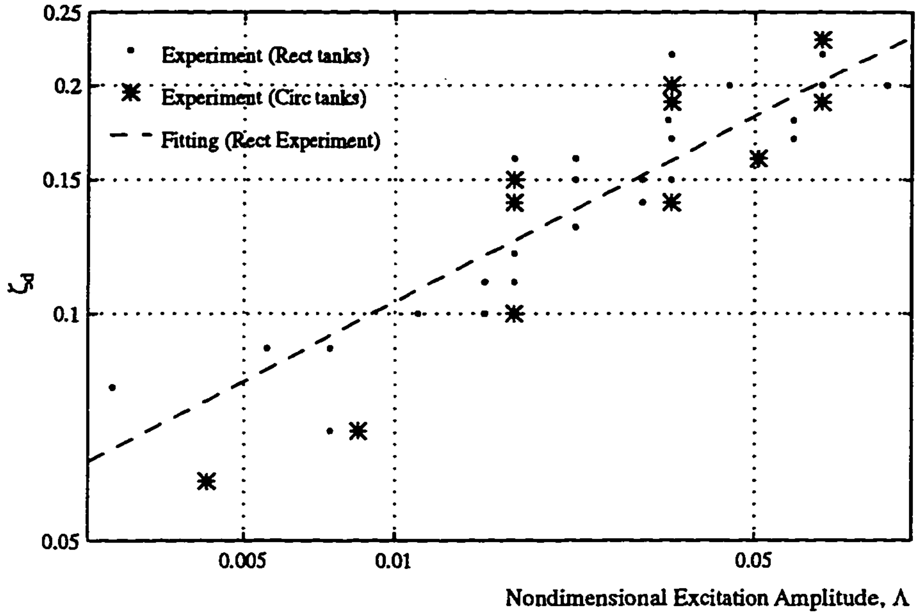

(a) Damping ratio

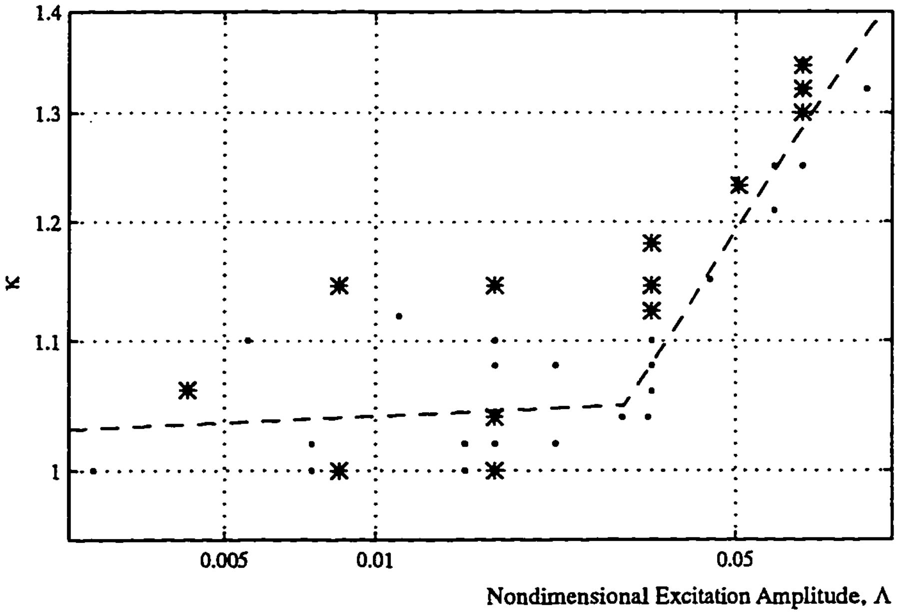

(b) Stiffness hardening ratio

Figure 3.4 The damping ratio, ζ_d, and the stiffness hardening ratio, κ, of the NSD model of the circular TLD determined from shaking table experiment.

3.2 RCM model - a numerical fluid model

The water sloshing motions were simulated numerically using the random choice method (RCM) that was proposed by Gardarsson and Yeh (1994). The shallow-water wave theory is briefly discussed prior to introducing the RCM model. The results of numerical analyses using the RCM model are presented and compared with the experimental data.

3.2.1 Shallow-water wave theory

In this section, background information on shallow-water wave theory is briefly described; the details are presented in Appendix F.

The shallow-water wave theory is based on the depth-averaged equations of mass and momentum conservation. The derivation of these equations involves the assumptions that water is an incompressible and inviscid fluid, the water depth is infinitesimally small in comparison with the characteristic horizontal length scale of the motion, the pressure field is hydrostatic everywhere, and the horizontal velocity is uniform throughout the depth. If one dimensional wave propagation is considered, the shallow-water equations of mass and momentum conservation are respectively,

$$h_t + (uh)_x = 0 \tag{3.15}$$

and

$$u_t + uu_x + gh_x = 0 \tag{3.16}$$

where all parameters are defined in Figure F.1 in Appendix F.

Free-surface flows like sloshing motion in a tuned liquid damper cannot create a significant pressure difference in the field so that the effect of water compressibility is considered to be negligible. While the energy dissipation associated with turbulence can be important, direct viscous effect on the fluid motion is negligible for the high Reynolds number flows typical of those in a tuned liquid damper. For the TLD, the water depth is usually much smaller than the horizontal dimension of the tank, which implies that the assumptions of the infinitesimal flow depth and hydrostatic pressure field are justified.

A wave described by the shallow-water wave equations propagates with a speed independent of its wave length, but dependent on its amplitude: the higher the wave amplitude, the faster it propagates. In other words, the shallow-water wave theory represents a non-dispersive and fully nonlinear wave system. The models based on the non-dispersive, fully-nonlinear shallow-water wave equations are believed capable of modeling wave-breaking, including the effect of energy dissipation, although the breaking is not characterized in detail but as a flow-property discontinuity. In fact, it is this property for which the shallow-water wave theory was adopted to analyze the sloshing motion in a tuned liquid damper since the focus is on the response under large amplitude excitation.

3.2.2 Numerical simulation of water sloshing motion using the RCM model

A numerical scheme to solve the shallow-water wave equations using the random choice method (RCM model) was proposed by Gardarsson and Yeh (1994). The random choice method is a shock-preserving scheme; the shock is represented by the discontinuities of water surface elevation and velocity between two adjacent grid points. This scheme causes no numerical dissipation or dispersion and follows precisely the mathematical formulation of the shallow-water wave theory. However, it has limitations in simulating the real fluid sloshing motion. For example, in a real fluid environment, the breaking wave front is not a discontinuity and the pressure field is not exactly hydrostatic, especially near the breaking wave front.

A series of numerical simulations as described in Table E.2 in Appendix E.2 were undertaken using the RCM model. The length of the tank was meshed with 400 grid points. In order to obtain the steady state responses, each case was run for 80 cycles of the linear fundamental natural period of the tank, $T = 1/f_w$ where f_w is the linear fundamental natural frequency of the tank which is calculated using Equation (2.31). As discussed in Section 2.2.4, the hydrodynamic forces of the TLD were calculated based on the hydrostatic pressures on the tank end walls using Equation (2.7).

Figure 3.5 shows the time history responses of the water sloshing for the case of L=590 mm, h_0=30 mm and A=20 mm. A comparison of these numerical results with the experimental ones presented in Figures 2.4 thru Figure 2.6 reveals discrepancies. It appears that the numerical scheme cannot simulate the higher frequency components observed in the experimental investigations in a satisfactory manner. However, the overall shapes of the time history responses are in good agreement with the ones obtained from the experimental investigations.

Figure 3.6 presents the frequency responses of the water sloshing for the same case. Several discrepancies are observed in comparing the results from the numerical simulations with the experimental investigations. One apparent difference is that the numerical scheme fails to simulate the jump phenomenon observed in the experimental investigation. The other discrepancies are mostly the result of failure in simulation of the higher modes of the water sloshing motion as discussed in the time history response plots.

The discrepancies are reduced in the plots of RMS base shear force and the energy dissipation per cycle. This observation is consistent with the effects of higher modes on the water sloshing motions discussed in Section 2.2.3. However, considering the difficulties in simulating the wave breaking, the RCM model predicts the water sloshing motion with wave breaking with a satisfactory accuracy, particularly, in terms of the energy dissipation capacity.

As described in Section 3.1.2, the damping and stiffness values of a TLD can be determined using the energy dissipation matching scheme. This procedure was applied to the rectangular TLDs described in Table E.2 of Appendix E. The results are plotted in Figure 3.7 as cross-marks. For comparison purposes, the experimental results (dotted marks) and its best fitted curve (dashed line) are presented also in the figure.

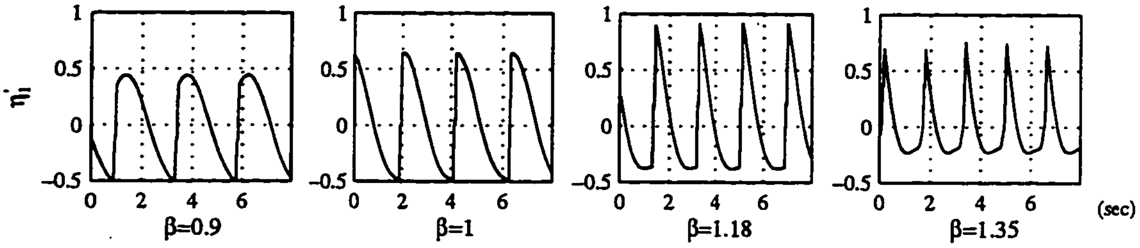

(a) Wave height at end wall

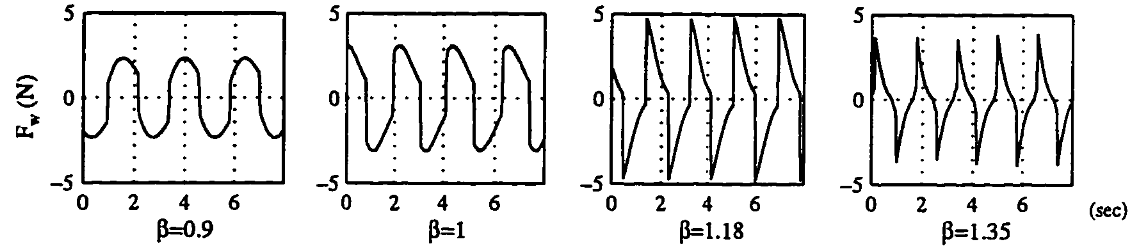

(b) Base shear force

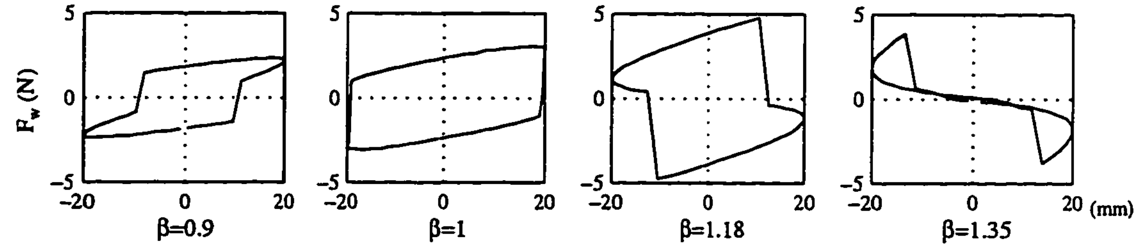

(c) Energy loop

Figure 3.5 Sample time history responses of water sloshing motion simulated using the RCM model for the rectangular tank of L=590mm, h_0=30mm and A=20mm

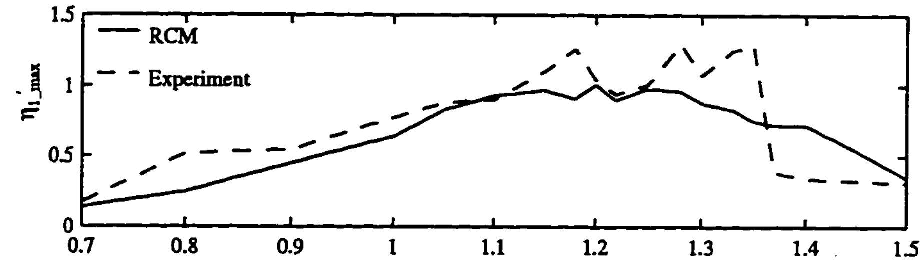

(a) Maximum wave height near end wall

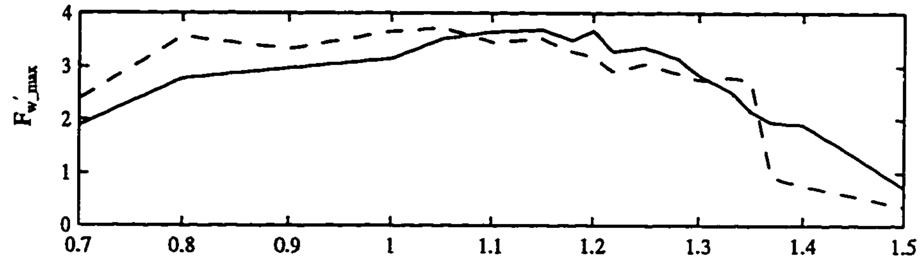

(b) Maximum base shear force

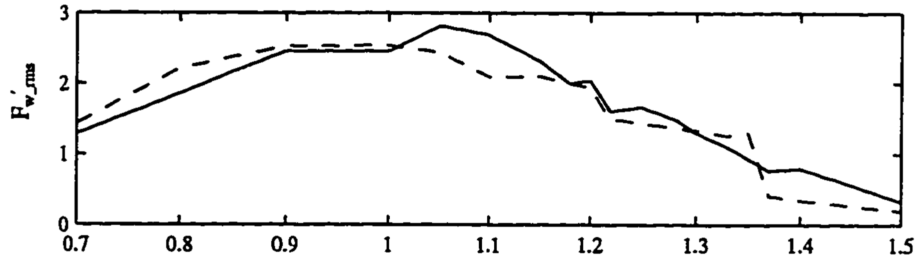

(c) RMS base shear force

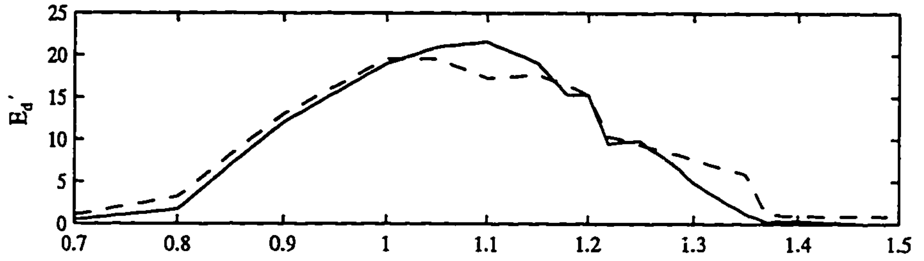

(d) Energy dissipation per cycle

Figure 3.6 Sample frequency responses of water sloshing motion simulated using the RCM model for the rectangular tank of L=590mm, h_0=30mm and A=20mm.

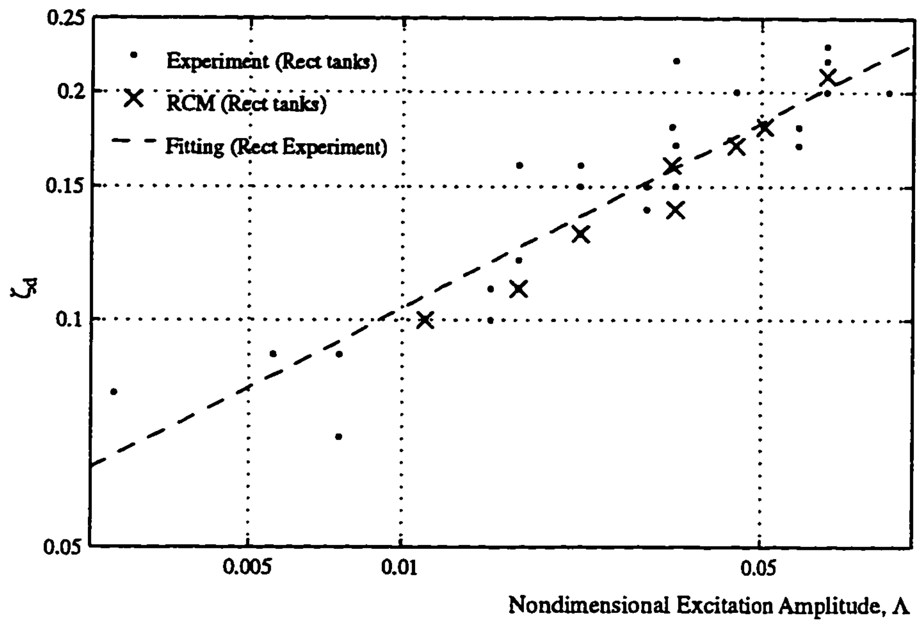

(a) Damping ratio

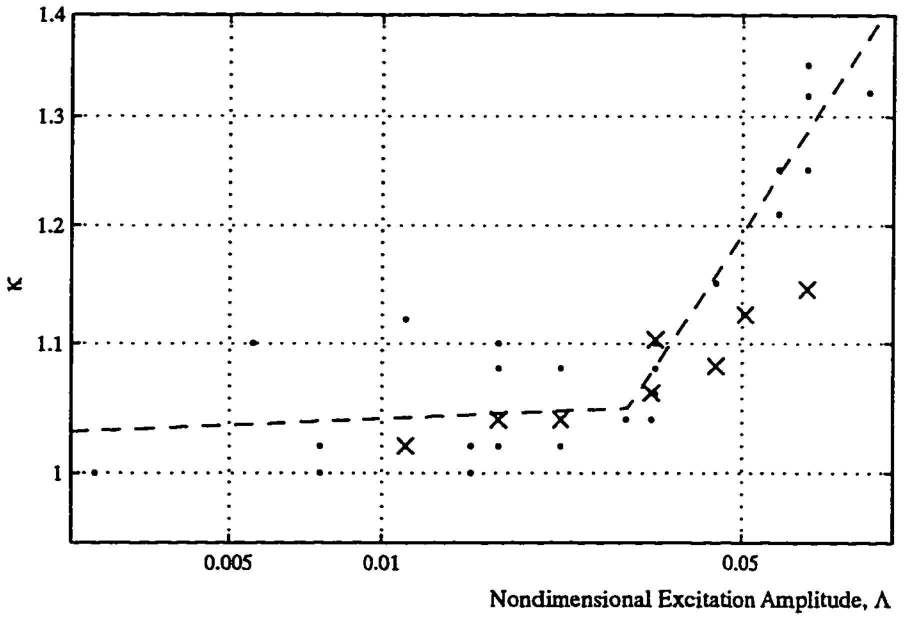

(b) Stiffness hardening ratio

Figure 3.7 The damping ratio, ζ_d, and the stiffness hardening ratio, κ, of rectangular TLDs determined from numerical analyses using the RCM model.

The results from numerical simulations show good agreement with the experimental results in estimating the damping values of the TLDs in the entire range of excitation amplitudes. Two results also agree well in estimating the stiffness of the TLDs over the range of excitation amplitude $\Lambda<0.03$, i.e., weak wave breaking region. However, in the strong wave breaking region, i.e., $\Lambda>0.03$, the RCM model under-estimates the stiffness hardening characteristics of the TLD. This result confirms that the RCM model cannot accurately simulate the wave phenomenon under extremely strong excitation motions. It is, however, concluded that the RCM model accurately predicts the water sloshing motion for other breaking wave phenomena.

CHAPTER 4

DEVELOPMENT OF TLD DESIGN PROCEDURES

Design guidelines for TLDs based upon the numerical models discussed in Chapter 3 are described. The design guidelines are based upon the effectiveness measure defined as the reduction in peak structural displacement. Because the guidelines are based upon the interaction of the TLD with the structural system, this interaction model will be presented before loading-specific investigations are discussed.

4.1 Interaction of a TLD with a SDOF structure

Because the TLD is attached to a SDOF structure, the dynamic structural responses to the external forces are based upon its inherent damping and the damping forces generated by the TLD. In Section 4.1.1, this nonlinearly coupled system is formulated. Numerical solution schemes for the coupled system in time domain are proposed.

4.1.1 Time history numerical solution schemes

Figure 4.1(a) shows the system of a SDOF structure equipped with a TLD. The hydrodynamic force generated by water sloshing motion acts as a resisting force (or, damping force) to the external force. The coupled system is treated as a SDOF system subjected to the total external force which is sum of the damping force, F_d and the external force, F_e. The equation of motion of the coupled system is expressed as

$$m_s\ddot{x}_s + c_s\dot{x}_s + k_s x_s = F_e + F_d \tag{4.1}$$

where m_s, c_s and k_s are mass, damping constant and stiffness constant and x_s is structural displacement, respectively. To determine F_d in the equation, the water sloshing motion is simulated using the RCM model at each time step. The damping forces, i.e., the hydrodynamic forces due to the water sloshing, are calculated from the wave height at the

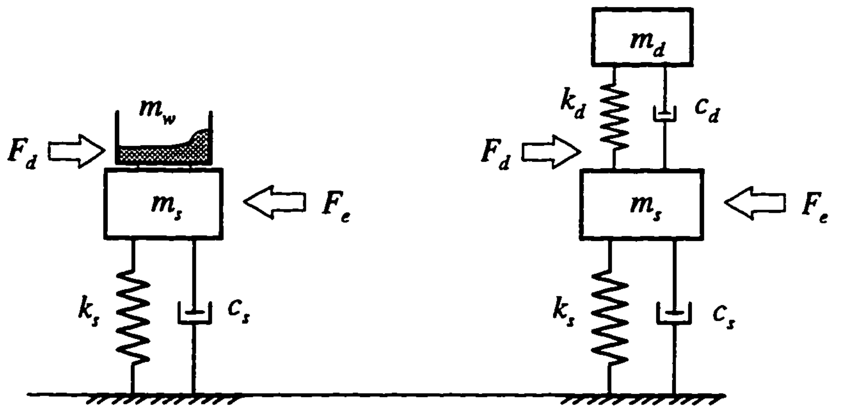

(a) TLD as RCM model (b) TLD as NSD Model

Figure 4.1 A SDOF structure with a TLD

end walls using Equation (2.15). Equation (4.1) is now solved analytically for each time step as described in Appendix D. The solution procedure is schematically illustrated in Figure 4.2.

Figure 4.1 (b) shows the equivalent system in which the TLD is characterized by the NSD model. The coupled system is treated as a traditional 2DOF system. The equation of motion is written as

$$\begin{bmatrix} m_d & 0 \\ 0 & m_s \end{bmatrix} \begin{Bmatrix} \ddot{x}_d \\ \ddot{x}_s \end{Bmatrix} + \begin{bmatrix} c_d & -c_d \\ -c_d & c_d + c_s \end{bmatrix} \begin{Bmatrix} \dot{x}_d \\ \dot{x}_s \end{Bmatrix} + \begin{bmatrix} k_d & -k_d \\ -k_d & k_d + k_s \end{bmatrix} \begin{Bmatrix} x_d \\ x_s \end{Bmatrix} = \begin{Bmatrix} 0 \\ F_e \end{Bmatrix} \qquad (4.2)$$

in which m, c, k and x are the mass, damping constant, stiffness constant and relative displacement of the structure, respectively. The subscripts d and s indicate the damper and structure, respectively. The quantities, m_s, m_d, c_s and k_s are given constants. The external forcing function F_e is approximated to be a constant at each time step of the numerical solving procedure. The damping constant c_d and the stiffness constant k_d of the NSD model are determined by Equations (3.9) and (3.10), respectively.

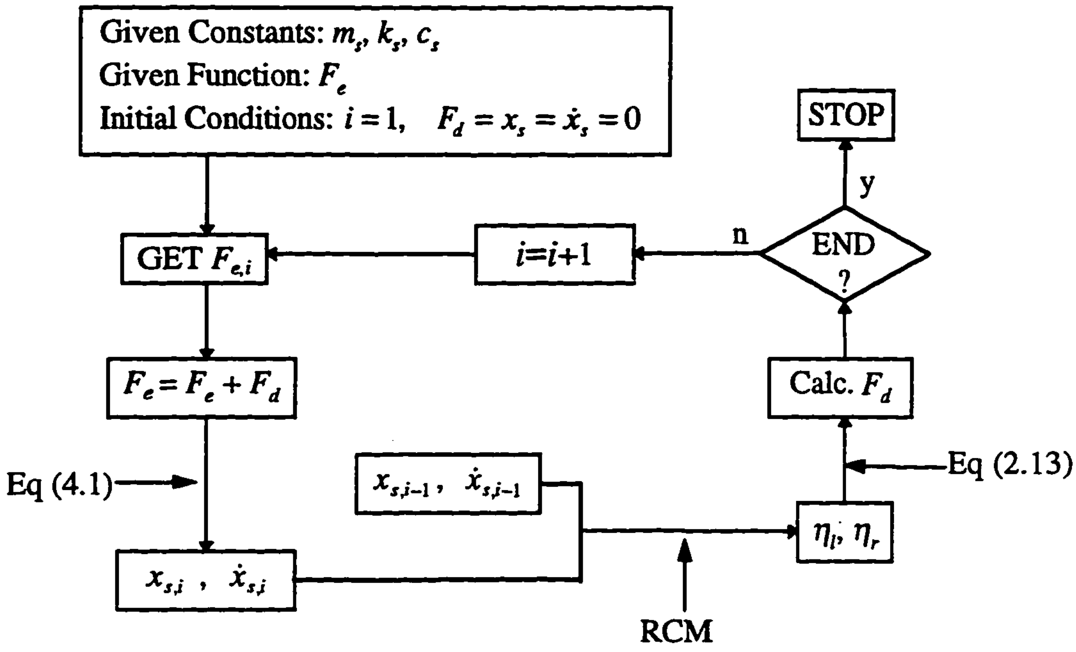

Figure 4.2 A numerical solution scheme for the responses of a SDOF structure coupled with a TLD. The TLD is simulated using the RCM model.

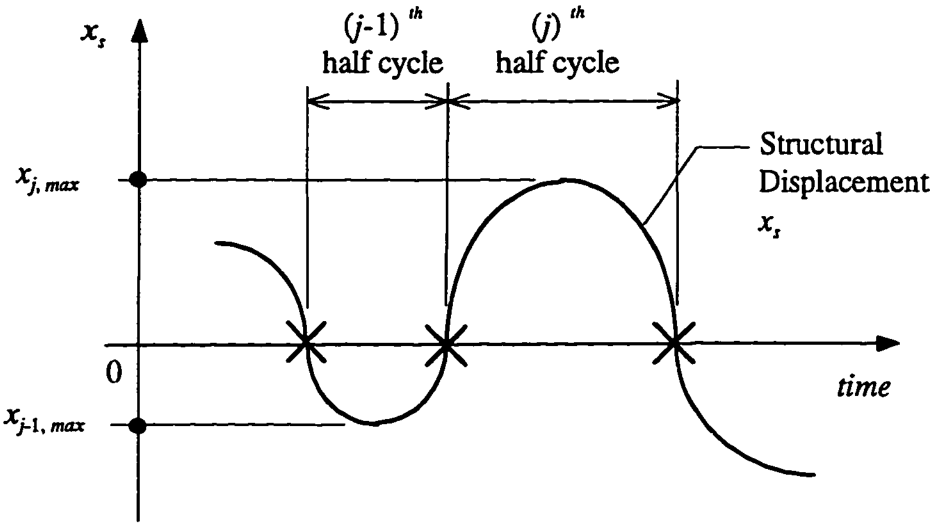

Figure 4.3 An arbitrary time history structural displacement.

Figure 4.3 shows an arbitrary sample time history structural displacement to illustrate how to determine the excitation amplitude A in Equations (3.9) and (3.10). Each time the structural displacement curve, x_s, crosses the horizontal time axis, the peak structural displacement, $x_{j\text{-}1,max}$ during the previous $(j\text{-}1)^{th}$ half cycle is sought. The absolute value of $x_{j\text{-}1,max}$ is assumed as the excitation amplitude A_j in Equations (3.9) and (3.10) during the next (j^{th}) half cycle to calculate c_d and k_d. The system stiffness and the damping matrices are reformulated with new values of c_d and k_d at this time step. Equation (4.2) is then solved using the Runge-Kutta method. The numerical solution procedure is illustrated in Figure 4.4.

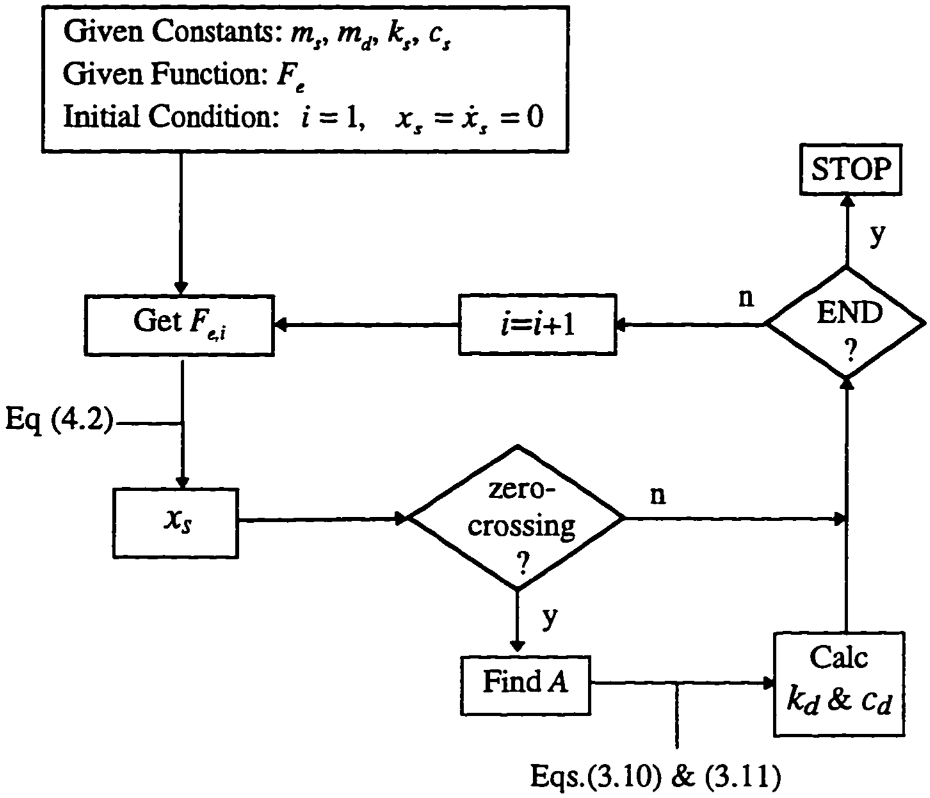

Figure 4.4 A numerical solution scheme for the responses of a SDOF structure coupled with a TLD. The TLD is characterized by the NSD model

4.1.2 Evaluation of the NSD model and the RCM model

It was shown in Figure 3.7 that the RCM model predicts accurately the energy dissipation capacity of the TLD in the region of weak wave breaking. It was also found, however, that the RCM model is not capable of predicting the energy dissipation capacity of the TLD in the strong wave breaking region. This limitation of the RCM model is verified through case studies in this section.

Consider the SDOF structural systems coupled with a TLD as shown in Figure 4.1. The properties of the selected systems are described in Table 4.1. In the first two cases, the tank size and the excitation amplitudes and frequencies fall into the range of the shaking table experimental investigations. The excitation amplitude for Case 1 was determined such that it falls into the region of weak wave breaking, i.e., A/L less than 0.03. Case 2 is for the same system as Case 1 but was subjected to stronger excitation which induces strong wave breaking in the TLD, i.e., A/L greater than 0.03. The tank size and the excitation amplitudes and frequencies for Case 3 fall beyond the range of shaking table experimental cases in order to evaluate the effectiveness of the NSD model in this range.

First, dynamic responses of the selected system for Case 1 under various excitation

Table 4.1 Data for case studies

Case	Structure		TLD				Exc.Amp$^{(*1)}$
ID	f_s	ζ_s	L	h	f_w	μ	$x_{0,max}$
1	0.458 Hz	0.7 %	590 mm	30 mm	0.458 Hz	1.0 %	50 mm
2	0.458 Hz	0.7 %	590 mm	30 mm	0.458 Hz	1.0 %	100 mm
3	0.180 Hz	0.7 %	2300 mm	70 mm	0.180 Hz	1.0 %	200 mm

(*1) The magnitude of the harmonic forcing function is adjusted such that the maximum structural displacement without the TLD becomes these values at steady-state.

frequencies were obtained by solving Equations (4.1) and (4.2) using the RCM and the NSD models, respectively. Figure 4.5 presents the time history structural responses for several excitation frequency ratios, $\beta = 0.95, 0.99, 1.00$ and 1.10. The results from the RCM and the NSD analyses at each excitation frequency are plotted together for comparison. The maximum structural displacements in the entire time duration and at steady-state are presented in the plots. The results from the two analyses are in close agreement in terms of both the shape and magnitude of the time history of the structural displacements.

Figure 4.6 shows the time histories of the damping and the stiffness hardening ratios of the NSD model for the cases as in Figure 4.5. These two parameters are recalculated at every zero-crossing time step using Equations (3.9) and (3.10) as explained in the previous section. It is noted that the values of κ for all four excitation frequency cases are approximately constant at 1.05 regardless of the structural excitation amplitudes. This behavior occurs because the structural vibration amplitudes for all four frequency cases fall into the region of weak wave breaking, i.e., $A/L < 0.03$ in which the values of κ changes slowly as shown in Figure 3.3.

Figure 4.7 presents the comparison of the results from both analyses in terms of the maximum structural displacements at sweep excitation frequencies. The maximum structural displacements at steady-state are plotted in Figure 4.7 (a). The two results are in close agreement. It is observed that the TLD reduces the maximum structural displacements at steady-state by approximately 70 %, i.e., from 50 mm for the structure without TLD to approximately 15 mm with TLD. The maximum structural displacements in the entire time duration are plotted in Figure 4.7 (b). The two results show close agreement.

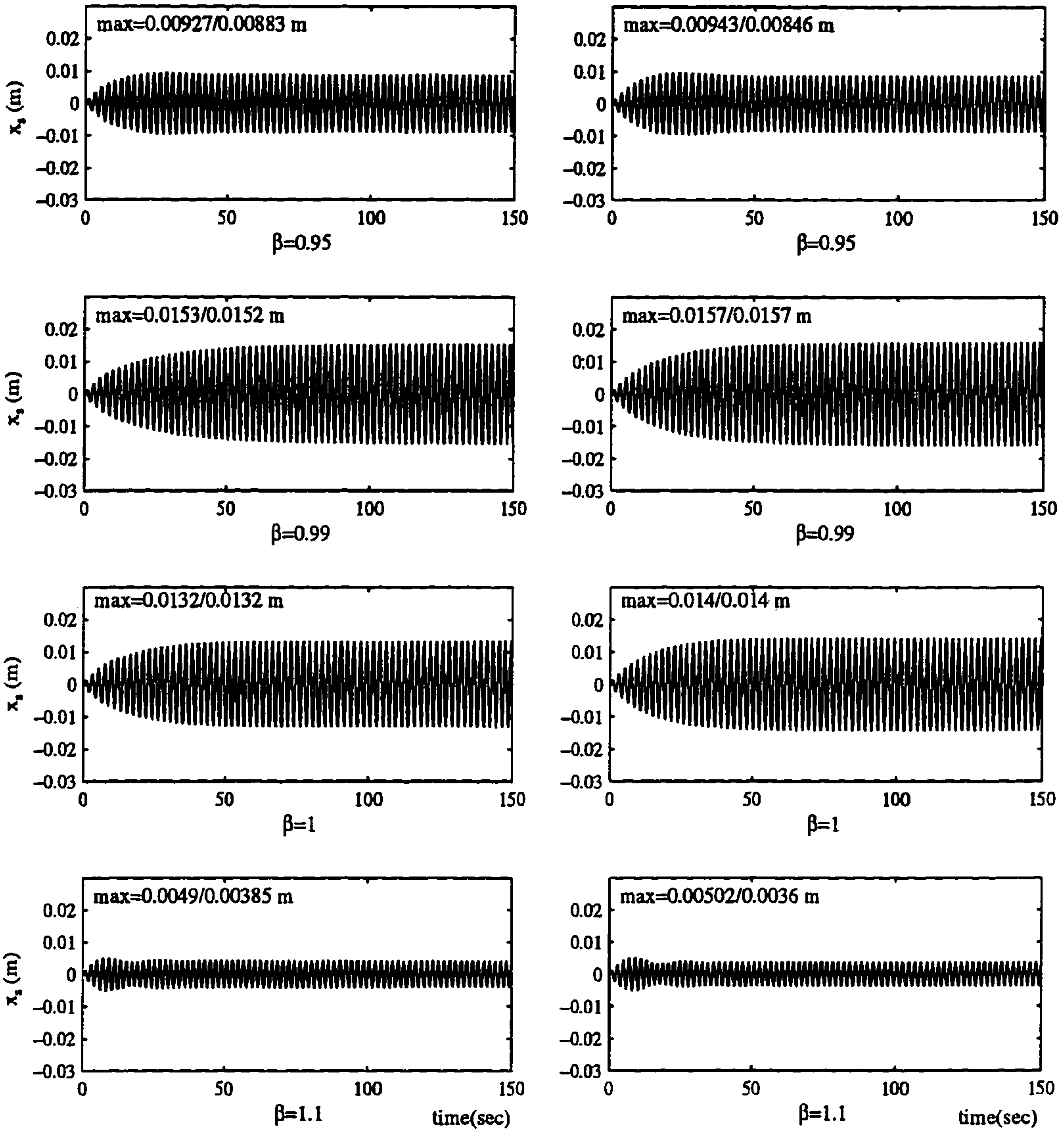

(a) RCM model (b) NSD model

Figure 4.5 Sample time history responses of the SDOF structure coupled with a TLD (Case 1). The TLD is characterized by the RCM and the NSD models, respectively. The excitation amplitude is in the region of weak wave breaking.

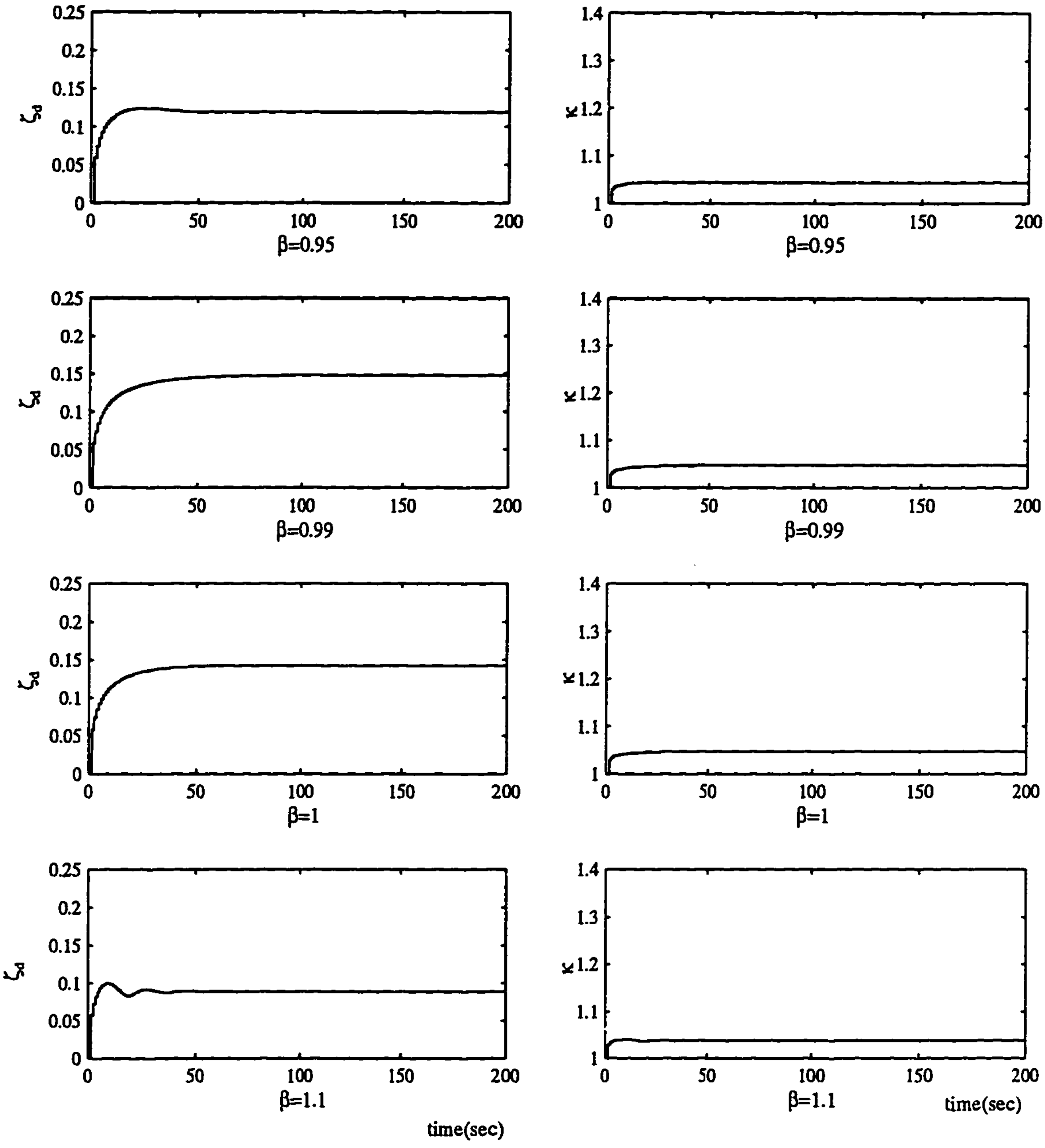

(a) Damping ratio

(b) Stiffness hardening ratio

Figure 4.6 Sample time histories of the NSD model properties for the TLD for the same cases as Figure 4.5.

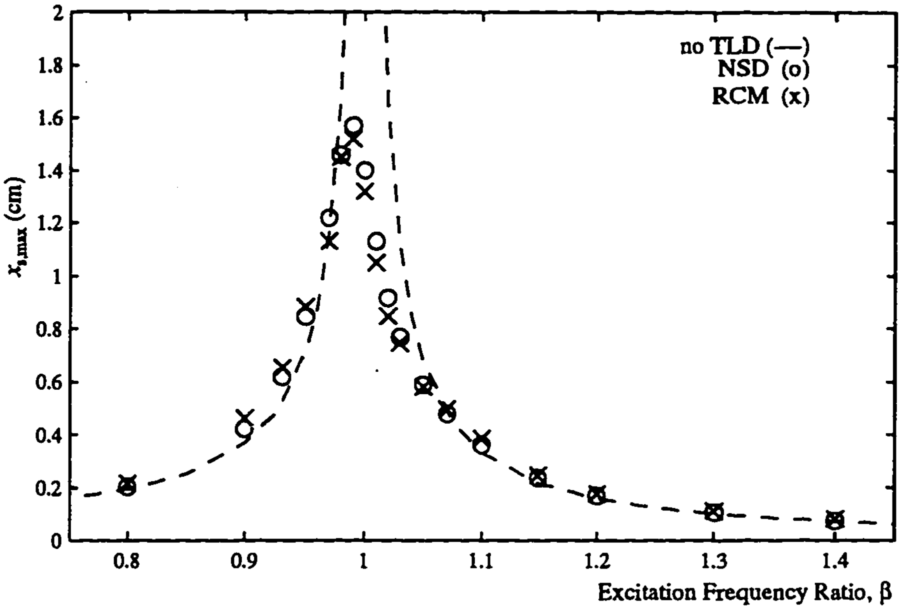

(a) Maximum structural displacement at steady state

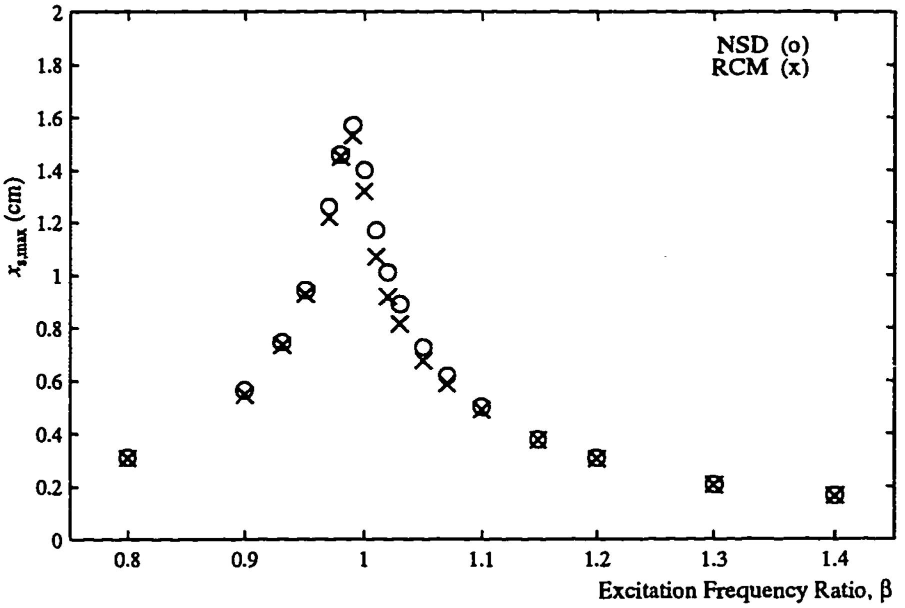

(b) Maximum structural displacement over entire period

Figure 4.7 The maximum displacements of the structure coupled with a TLD at sweep excitation frequencies. The TLD is characterized by the RCM and the NSD models, respectively. The excitation amplitude is in the region of weak wave breaking.

Next, the system for Case 2 was analyzed using two models in the same manner. The excitation amplitude in this case falls into the strong wave breaking region, i.e., A/L > 0.03, near the resonance frequency. As noted previously in Chaper 3, the RCM model cannot predict the TLD energy dissipation capacity accurately in this excitation range. The time history responses of the structure for Case 2 are presented in Figure 4.8 for several excitation frequencies, β = 0.95, 0.99, 1.00 and 1.10. The results from both analyses are plotted together for comparison. The results at excitation frequency ratios β = 0.95 and 1.10 are in close agreement. However, at $\beta = 0.99$ and 1.00 which are near resonance frequency, the structural displacement becomes larger and the values of the parameter A/L fall into the region of strong wave breaking, i.e., A/L is greater than 0.03. In this region, the RCM model has not predicted the behavior of the TLD accurately. The TLD develops stronger nonlinear behavior than predicted by the RCM model. Consequently, the TLD tuning is farther from the linear natural frequency and the structural natural frequency; therefore, it demonstrates less effectiveness.

Because the values of the NSD model parameters were derived based on the empirical results, the validity of the NSD model beyond the experimental range must be investigated. Case 3 was designed for this purpose. The selected structural natural frequency $f_s = 0.18$ Hz and the length of the TLD $L = 2300$ mm are outside of the range of the shaking table experimental cases. The water depth was determined such that the TLD is tuned to the structural natural frequency. The designated excitation amplitude $x_{0,max}$ = 270 mm was selected such that the steady-state structural motions for all excitation frequencies fell into the region of weak wave breaking. In this excitation region, the RCM model predicts the TLD behavior accurately. Numerical analyses were conducted using two models in the same manner as Case 1 and 2. The results are plotted in Figure 4.9. The results from the NSD model analyses demonstrate close agreement with those from the RCM model analyses for all excitation frequency cases. This result implies that the NSD model is valid for the conditions beyond those used for the derivation. In summary;

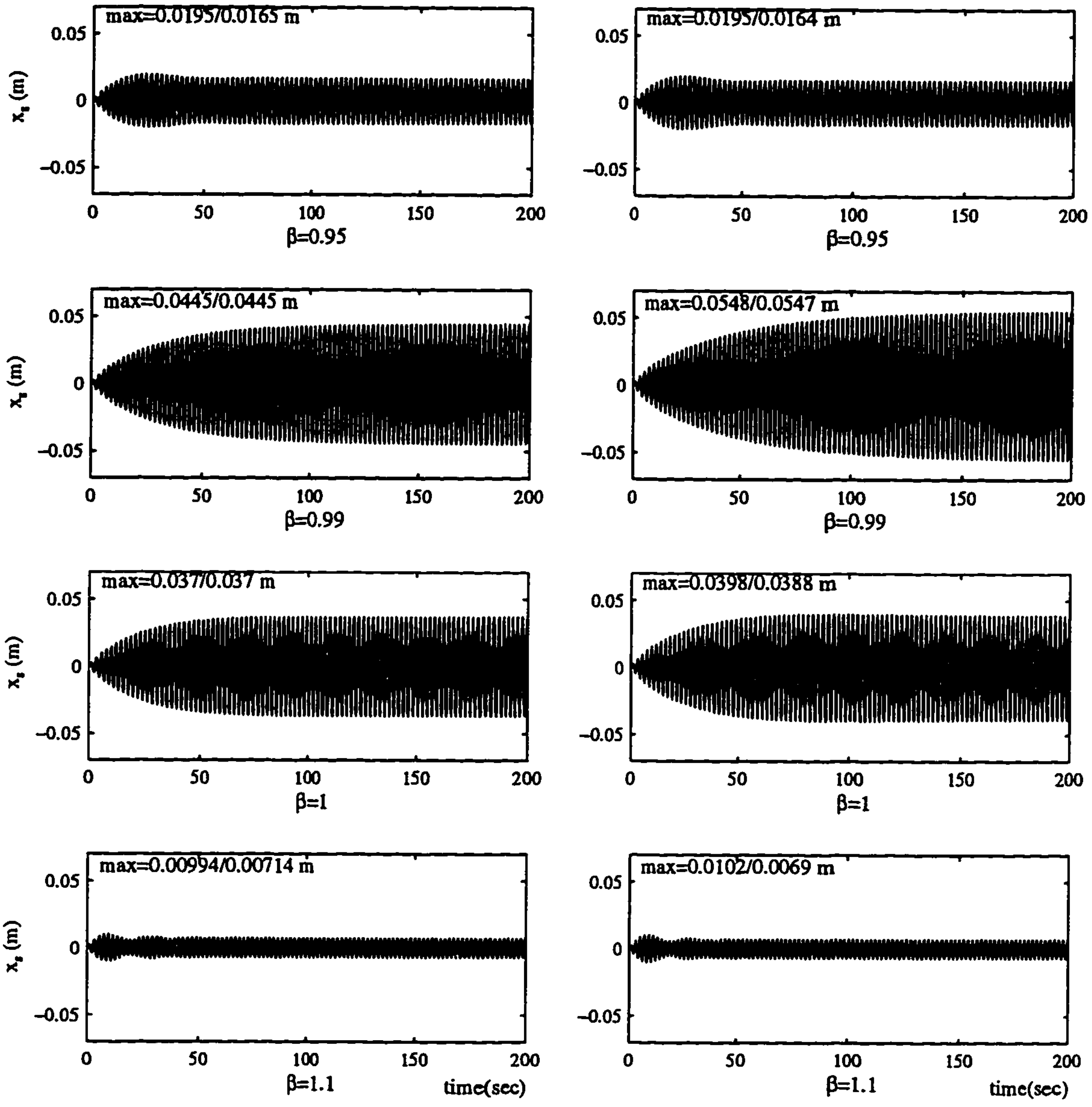

(a) RCM model (b) NSD model

Figure 4.8 Sample time history responses of the SDOF structure coupled with a TLD (Case 2). The TLD is characterized by the RCM and the NSD models, respectively. The excitation amplitude near resonance falls into the region of strong wave breaking.

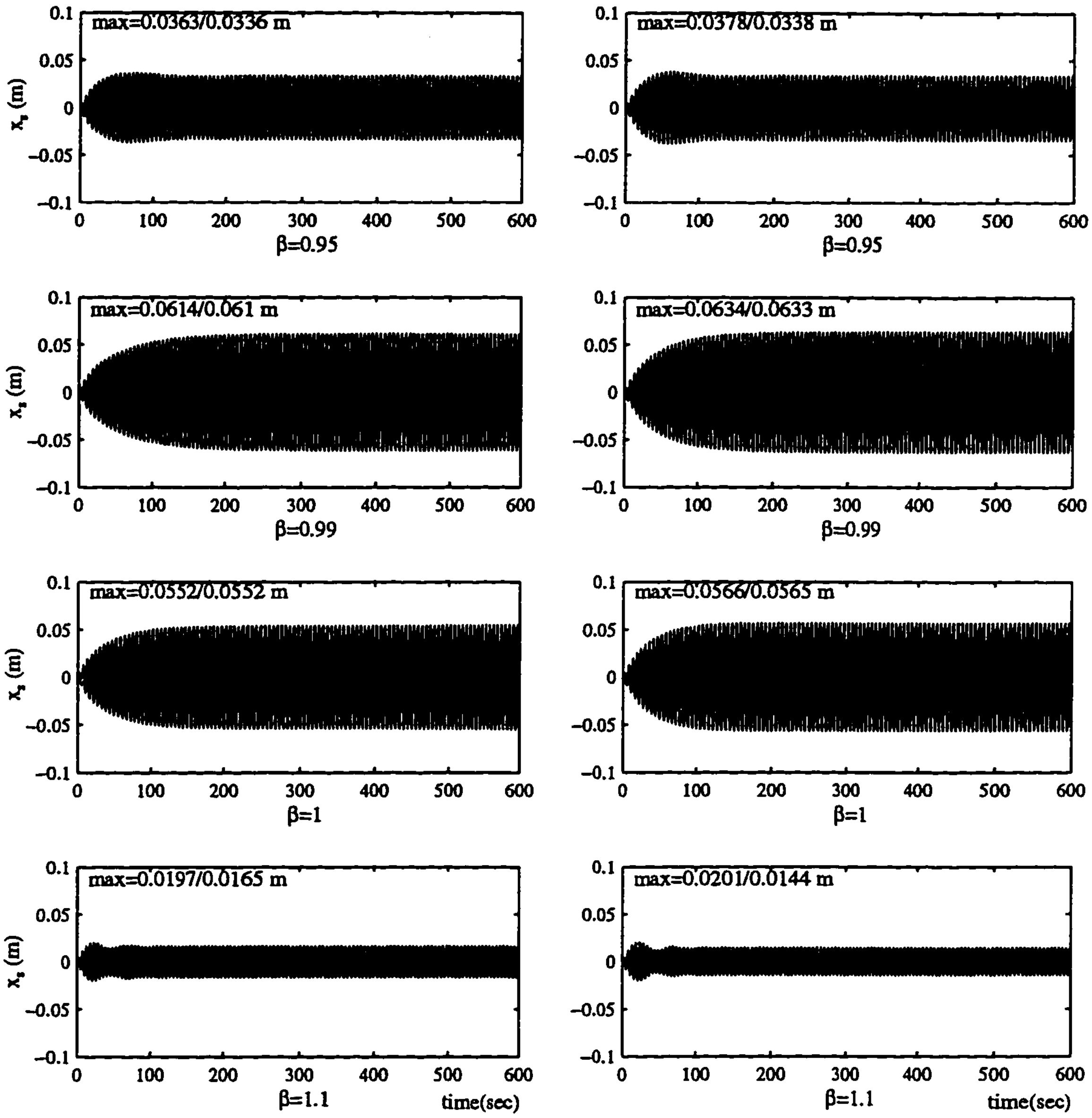

(a) RCM model (b) NSD model

Figure 4.9 Sample time history responses of the SDOF structure coupled with a TLD (Case 3). The TLD is characterized by the RCM and the NSD models, respectively. The selected system is in the condition beyond the experimental cases.

- The NSD model and the RCM model predict the TLD performance accurately in the excitation region of weak wave breaking.
- The RCM model does not adequately capture strong wave breaking.
- The NSD model which has been calibrated from the limited experimental investigation was shown to be valid for certain conditions which are beyond the limited experimental cases.

4.2 TLD performance and design procedure for harmonic excitations

In this section, the performance of TLDs coupled with a lightly damped SDOF structure is investigated for harmonic excitation. A frequency response analysis method coupled with an iteration procedure to solve the nonlinear system is proposed. The effectiveness of the TLD is defined as the reduction of the maximum displacement of the structure. The influence of the TLD nonlinearity on its effectiveness is evaluated. A simple TLD design procedure incorporating nonlinearity is proposed.

4.2.1 Frequency response analysis

A SDOF structural system equipped with a TLD can be modeled as a two-degree-of-freedom system by using the NSD model for the TLD as shown in Figure 4.10. The properties of the NSD model (k_d and c_d) are functions of the peak amplitude of the structural motion as described in Equations (3.9) and (3.10). As the structure is subjected to a harmonic excitation, the peak amplitude of the structural motion becomes a constant at steady-state. The properties of the NSD model (k_d and c_d), therefore, become constant at steady-state. Consequently, the TLD behaves like a linear system at steady-state. Therefore, the peak displacement of the structure at steady-state can be calculated by[1]

$$x_0 = \frac{F_0}{k_s} \frac{1}{\sqrt{RE^2 + IM^2}}, \tag{4.3}$$

---

[1] See Appendix B for detailed solution procedure

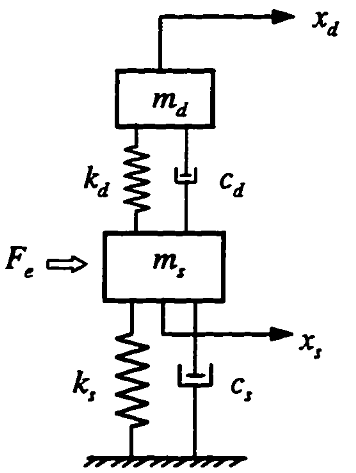

Figure 4.10 A SDOF structure equipped with a TLD (NSD model)

where,

$$RE = 1-\beta^2-\mu\beta^2\frac{\gamma^2\left(\gamma^2-\beta^2+(2\zeta_d\beta)^2\right)}{\left(\gamma^2-\beta^2\right)^2+(2\gamma\zeta_d\beta)^2}, \qquad IM = 2\zeta_s\beta+\frac{2\mu\gamma\zeta_d\beta^5}{\left(\gamma^2-\beta^2\right)^2+(2\gamma\zeta_d\beta)^2}, \tag{4.4}$$

$$\omega_s=\sqrt{\frac{k_s}{m_s}},\quad \omega_d=\sqrt{\frac{k_d}{m_d}},\quad \zeta_s=\frac{c_s}{2\sqrt{k_s m_s}},\quad \zeta_d=\frac{c_d}{2\sqrt{k_d m_d}}, \qquad \mu=\frac{m_d}{m_s},\quad \beta=\frac{\omega}{\omega_s},\quad \gamma=\frac{\omega_d}{\omega_s}. \tag{4.5}$$

To normalize Equation (4.3), the peak displacement of the structure without TLD is introduced

$$x_{0,wo}=\frac{F_0}{k_s}\frac{1}{\sqrt{(1-\beta^2)^2+(2\zeta\beta)^2}}\,. \tag{4.6}$$

The resonance peak displacement of the structure without TLD can be calculated by

$$A_0 = \frac{F_0}{k_s}\frac{1}{2\zeta_s\sqrt{1-\zeta_s^2}} \,. \tag{4.7}$$

The normalized peak displacement of the structure is obtained by dividing Equation (4.3) by (4.7) and expressed as

$$x_0' = \frac{x_0}{A_0} = \frac{2\zeta_s\sqrt{1-\zeta_s^2}}{\sqrt{RE^2+IM^2}} \,. \tag{4.8}$$

Because ζ_d and γ are functions of x_0, an iteration procedure is required to solve Equation (4.8). A simple iteration procedure is illustrated in Figure 4.11. The initial value of x_0 is

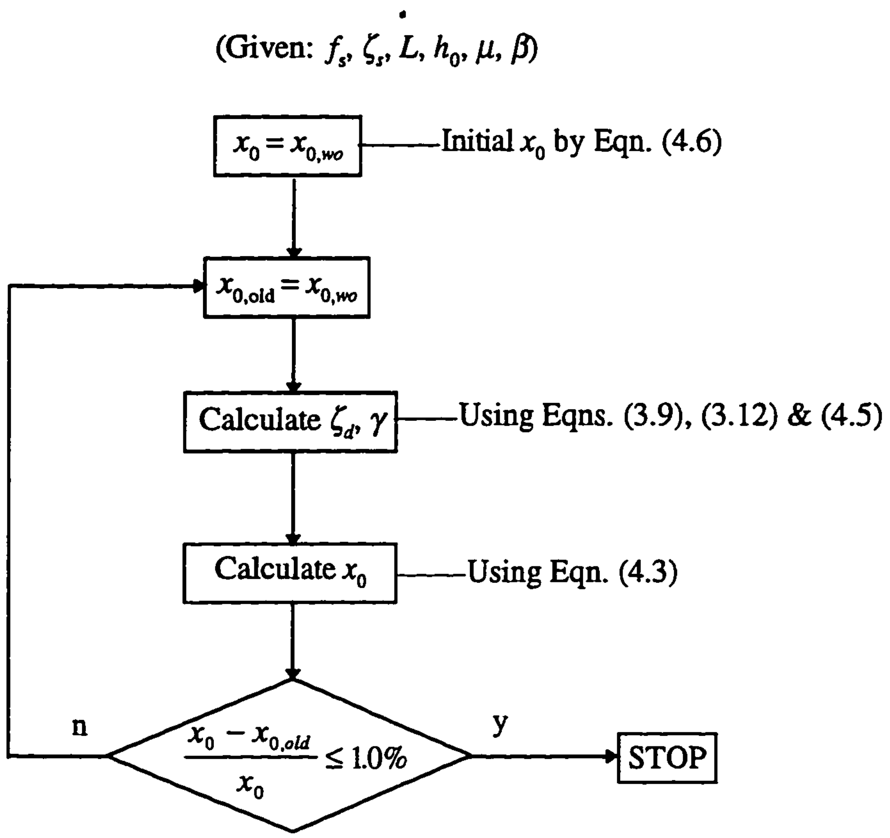

Figure 4.11 A solution procedure for the frequency responses of a structure coupled with a TLD as the structure is subjected to harmonic excitations. The TLD is characterized by the NSD model.

set to the peak displacement of the structure without the TLD calculated using Equation (4.6). Iteration stops as the calculated x_0 converges to the assumed x_0: in this study, the convergence criterion of 1.0 % is applied.

The effectiveness of the TLD is measured in terms of reduction in the maximum peak displacement of the structure due to the TLD as

$$\Psi = 1 - \max(x_0') \ . \tag{4.9}$$

4.2.2 TLD tuning - linear tuning and nonlinear tuning

In practice, the size of the tank is selected based upon construction considerations. The water depth is calculated to tune the TLD to the structure using the linear shallow-water wave theory. This is referred to as "linear tuning" of the TLD because the linear fundamental natural frequency of the TLD is tuned to the fundamental natural frequency of the structure. The linearly tuned water depth for the given size of the tank is calculated from Equation (2.1):

$$h_0 = \frac{L}{\pi}\tanh^{-1}\left(\frac{4\pi}{g}Lf_s^2\right) . \tag{4.10}$$

As discussed in the previous chapters, the real (or nonlinear) natural frequency of the TLD shifts from the linear natural frequency as a function of the excitation amplitude (See Equation (3.12)). The "nonlinear tuning" of the TLD is defined as: tuning the nonlinear fundamental natural frequency of the TLD to the fundamental natural frequency of the structure. From Equations (2.1) and (3.3), the nonlinear fundamental natural frequency is expressed as

$$f_d = \frac{\xi}{2\pi}\sqrt{\frac{\pi g}{L}\tanh\frac{\pi h_0}{L}} . \tag{4.11}$$

If the TLD is characterized by the NSD model, it is assumed that the nonlinear fundamental natural frequency f_d is related to the structural frequency f_s by the optimum tuning ratio, γ_{opt} for a TMD[1] as follows:

$$f_d = \gamma_{opt} f_s \; . \tag{4.12}$$

Combining Equations (4.11) and (4.12), the nonlinearly tuned water depth for the given size of the tank can be estimated by:

$$h_0 = \frac{L}{\pi} \tanh^{-1}\left(\frac{4\pi}{g} \frac{\gamma_{opt}^{\;2}}{\xi^2} L f_s^{\,2} \right) . \tag{4.13}$$

In this equation, h_0 is a function of ξ which is a function of excitation amplitude. Therefore, an iteration procedure is required to determine the nonlinearly tuned water depth h_0.

4.2.3 TLD performance for harmonic excitations

Steady-state responses of a structure equipped with a TLD can be obtained by solving Equation (4.8) using the proposed iteration solution scheme as described in Figure 4.11. For the given structural properties (f_s, ζ_s) and the mass ratio (μ), the structural response is a function of L, h_0 and β. The normalized structural responses also depend on the excitation amplitude because of the nonlinear characteristics of the TLD. In this section, performance of various TLDs attached to a lightly damped SDOF structure are evaluated by comparing sweep frequency responses of the structure for each TLD. The performance is measured in terms of the effectiveness as described in Equation (4.9).

A structure with natural frequency f_s = 0.32 Hz and damping ratio ζ_s = 1.0 % was selected.[2] The mass ratio μ of the TLD to the structural mass is set equal to 1.0 %. Because the property of the TLD depends on the excitation amplitude as shown in

---

[1] See Appendix B.2 for γ_{opt}

[2] The property of the selected structure is adopted from the Shin Yokohama Prince Hotel (Wakahara, 1992)

Equations (3.9) and (3.10), two different excitation amplitudes were employed. The excitation amplitudes were determined such that the maximum peak accelerations of the structure with a linearly tuned liquid damper becomes the designated values, $\ddot{x}_s$ = 20 or 3 milli-g. The corresponding maximum peak displacements for the selected structure can be calculated as $x_{s,0} = \frac{\ddot{x}_s}{\omega^2}$ = 4.85 or 0.73 cm. By estimating 60 % reduction in the peak acceleration due to a linearly tuned liquid damper, the maximum peak displacement of the structure without a TLD is estimated as $A_0 = \frac{x_{s,0}}{(1-0.6)}$ = 12.13 or 1.82 cm. The amplitude of the harmonic forcing, F_0, was determined such that the maximum peak displacement A_0 of the structure without a TLD becomes 12.13 or 1.82 cm, respectively, by using the equation:

$$F_0 = A_0 k_s 2\zeta_s \sqrt{1-\zeta_s^2} \; . \tag{4.14}$$

Two different sizes of TLDs (L = 171 and 300 mm) were employed for each excitation amplitude. Three different water depths were selected for each tank such that each TLD is linearly tuned, nonlinearly tuned or mis-tuned. The linearly tuned water depth was determined using Equation (4.10). The nonlinearly tuned water depth was determined using Equation (4.13). The mis-tuned water depth was selected to simulate the condition of approximately 10 % miscalculation in the water depth from the nonlinearly tuned value. The characteristics of the selected TLDs and excitation amplitudes are described in Table 4.2.

The results of the analyses for the frequency responses of the structure for each case are plotted in Figure 4.12 and 4.13 for each excitation amplitude, respectively. The plotted quantities are the responses normalized to the maximum response of the structure without the TLD. The resulting properties and effectiveness of each TLD are tabulated in Table 4.2. The results are summarized as follows:

- The performance of the TLD depends on the excitation amplitude. For example, the TLD with L = 171 cm and h_0 = 12.4 cm demonstrates an effectiveness level of 60 % and 70 % at acceleration level $\ddot{x}_s$ = 20 or 3 milli-g, respectively. In these limited cases, TLDs perform better at a lower excitation amplitude because the TLDs develop the damping ratios close to the optimum values at the acceleration level $\ddot{x}_s$ = 3 milli-g.
- The performance of the TLD is maximized by nonlinear tuning. For a given size of a tank, nonlinear tuning is achieved by adjusting the water depth.

Table 4.2 Properties and performance of TLDs attached to a structure at resonance.
(f_s = 0.32 Hz, ζ_s = 1.0 %, μ = 1.0 %)

Data						Results			
(*1)	Tank		Linear		Tuning	Nonlinear			Effectiveness
$\ddot{x}_s$ (milli-g)	L (cm)	h (cm)	$f_{d,lin}$ Hz	γ_{lin}	Type	ζ_d (%)	κ	γ	ψ (%)
20	171	12.4	0.32	1.00	(*1)	15	1.04	1.02	60
		11.6			(*2)	15	1.04	0.99	63
		10.5			(*3)	15	1.04	0.94	60
	300	39.7	0.32	1.00	(*1)	12	1.04	1.02	65
		36.8			(*2)	11	1.04	0.99	69
		33.0			(*3)	12	1.04	0.94	63
	600	180			(*2)	8.3	1.04	0.99	75
3	171	12.4	0.32	1.00	(*1)	6.8	1.02	1.02	70
		11.6			(*2)	6.3	1.03	0.98	76
		10.5			(*3)	7.3	1.03	0.94	63
	300	39.7	0.32	1.00	(*1)	5.6	1.03	1.01	70
		36.8			(*2)	5.3	1.03	0.98	74
		33.0			(*3)	6.2	1.04	0.93	60

Notes: *1. Linearly tuned, i.e., γ_{lin} = 1.0
*2. Nonlinearly tuned, i.e., γ = 0.99
*3. Mis-tuned, i.e., γ < 0.99
*4. Estimated structural acceleration in *milli-g*.

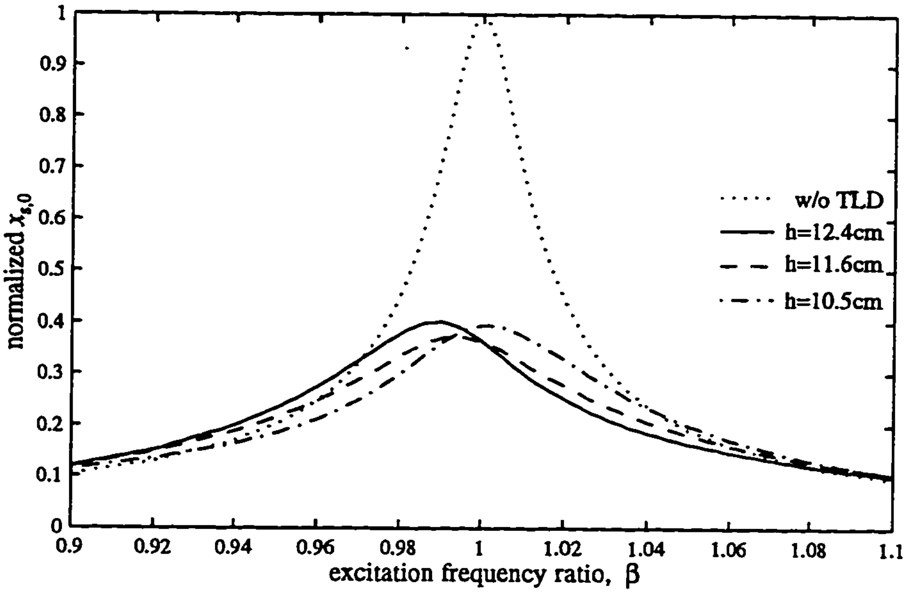

(a) $L = 171$cm

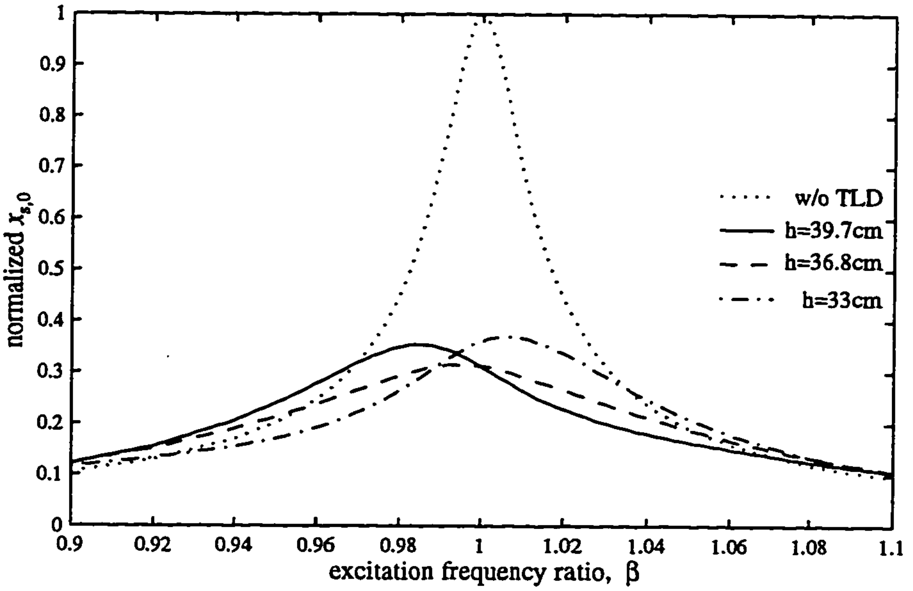

(b) $L = 300$cm

Figure 4.12 Frequency responses of the structure coupled with various TLDs. The natural frequency and the damping ratio of the structure are f_s=0.32 Hz and ζ_s=1.0 %. The mass ratio, μ=1.0%. The estimated maximum acceleration of the structure with the TLD, $x_{0,max}$ is approximately 20 *milli-g*.

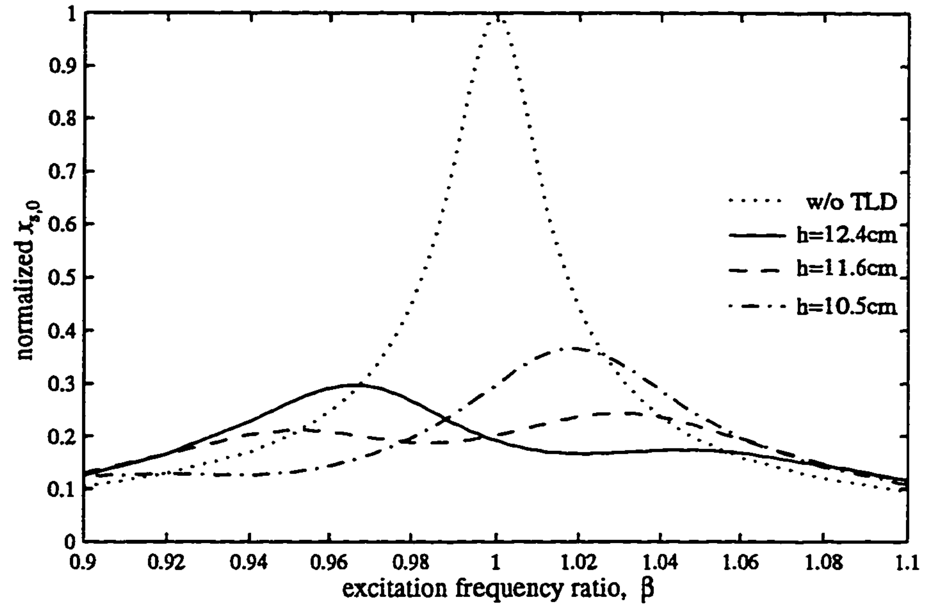

(a) $L = 171$cm

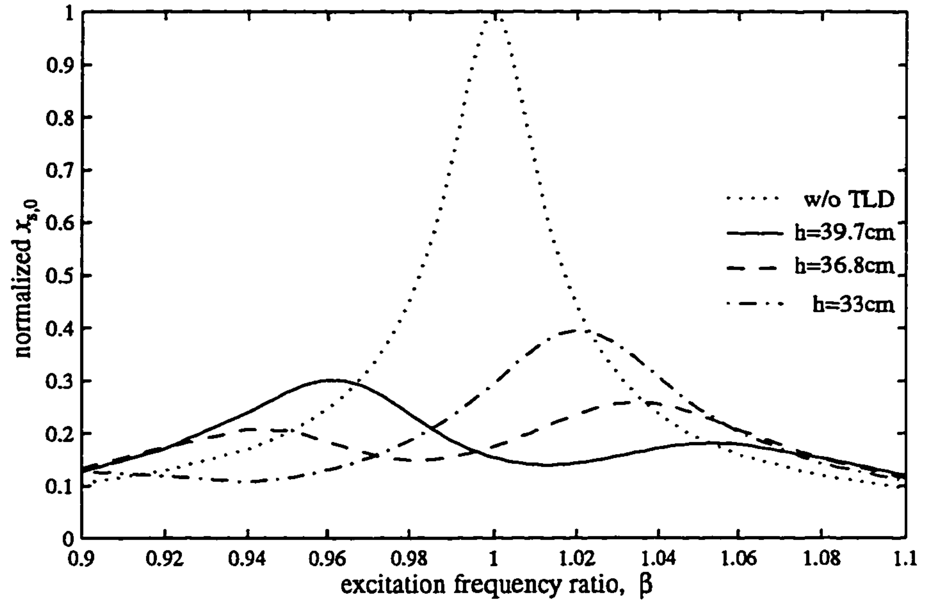

(b) $L = 300$cm

Figure 4.13 Frequency responses of the structure coupled with various TLDs. The natural frequency and the damping ratio of the structure are f_s=0.32 Hz and ζ_s=1.0 %, respectively. The mass ratio μ=1.0%. The estimated maximum acceleration of the structure with the TLD $x_{0,max}$ is approximately 3 *milli-g*

- The performance of TLD depends on the tank size. For example, the nonlinearly tuned TLDs with L = 171 cm and 300 cm demonstrate the effectiveness of 63 % and 69 %, respectively, at the acceleration level $\ddot{x}_s$ = 20 milli-g. In this case, the larger TLD performs better because it develops the damping ratios closer to the optimum values than the smaller one. However, at the acceleration level $\ddot{x}_s$ = 3 milli-g, the performance of both TLDs are at similar levels because their damping values are similar. Both TLDs demonstrate the higher effectiveness level, i.e., Ψ = 76 % and 74 %, respectively, because the damping ratios of both TLDs at this acceleration level are close to the optimum value.
- The TLDs at acceleration level $\ddot{x}_s$ = 20 milli-g develops high damping compared to the optimum value. To lower the damping value of the TLD, the tank size was increased to L = 600 cm. This TLD develops the damping ratio 8.3 % which is close to the optimum value and increases the effectiveness to 75 %.
- The mis-tuned TLDs have lower effectiveness for all cases.

4.2.4. TLD design guide for harmonic excitations

Consider a SDOF structure equipped with a linear mechanical damper. The normalized peak displacement of the structure x_0' as shown in Equation (4.8), is a function of μ, ζ_s, ζ_d, γ, and β. The normalized maximum structural displacement $x_{0,\max}'$ is defined as the maximum value of x_0' over sweep excitation frequencies. With given values of μ and ζ_s, $x_{0,\max}'$ is expressed as a function of ζ_d and γ.

The plots of $x_{0,\max}'$ vs. ζ_d of the linear system with various tuning ratios make a family of design curves as shown in Figure B.2 in Appendix B. In Figure 4.14, the curves for two values of tuning ratios (γ = 0.99 and 1.02) are plotted for the cases used in the previous section, i.e., f_s=0.32 Hz, ζ_s=1.0 % and μ=1.0 %.

The results from the case studies for the linearly and nonlinearly tuned TLDs with various sizes in the previous section are shown in this family of curves. The results described in Table 4.2 for the TLDs at acceleration level $\ddot{x}_{s,\max}$ = 20 milli-g are plotted in Figure 4.14 (a). In particular, the result for the linearly tuned TLD with length L=171 mm, ζ_d = 15 % and γ = 1.02 is identified in Figure 4.14 (a) with the label of L171h12.4. The normalized maximum structural displacement $x_{0,\max}'$ is 0.40 which corresponds to an effectiveness of the TLD of ψ = 60 %. This agrees with the value in Table 4.2 which was obtained from the frequency response analyses. Table 4.2 identifies ζ_d = 15 % and γ = 0.99 for the nonlinearly tuned TLD with the same size tank. These values are plotted with a cross-mark with the label of L171h11.6. An effectiveness of 63 % is identified from the figure, which agrees with the value in Table 4.2. The results from several other cases are shown in Figure 4.14(a) in the same manner. The nonlinearly tuned TLD with tank length L = 600 cm develops the values of ζ_d = 8.3 % and γ = 0.99 and the highest effectiveness of ψ = 75 %. Figure 4.14 (b) contains the plots of the results for the TLDs at excitation amplitude $\ddot{x}_{s,\max}$ = 3 milli-g in the same manner as described above. It is observed from this study that:

- There exists a TLD that performs most effectively under a harmonic excitation at a particular amplitude of excitation. The optimum parameters for the linear TMD hold true for the NSD model at steady-state.
- The effectiveness of a TLD at steady-state can be estimated using the design chart alone without further analysis.
- The nonlinear tuning significantly enhances the performance of the TLD as the damping ratio of the NSD model approaches the optimum value for the TMD.

Based upon the results of this numerical study, an iteration procedure was developed to select the most effective TLD for a given excitation amplitude. This design procedure is illustrated in Figure 4.15.

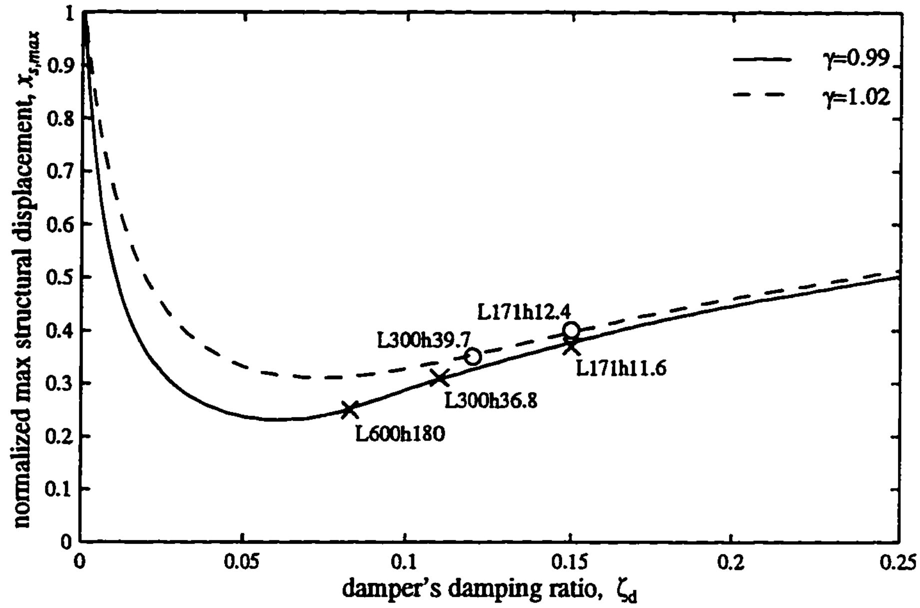

(a) $\ddot{x}_{s,\max}$ = 20 milli-g

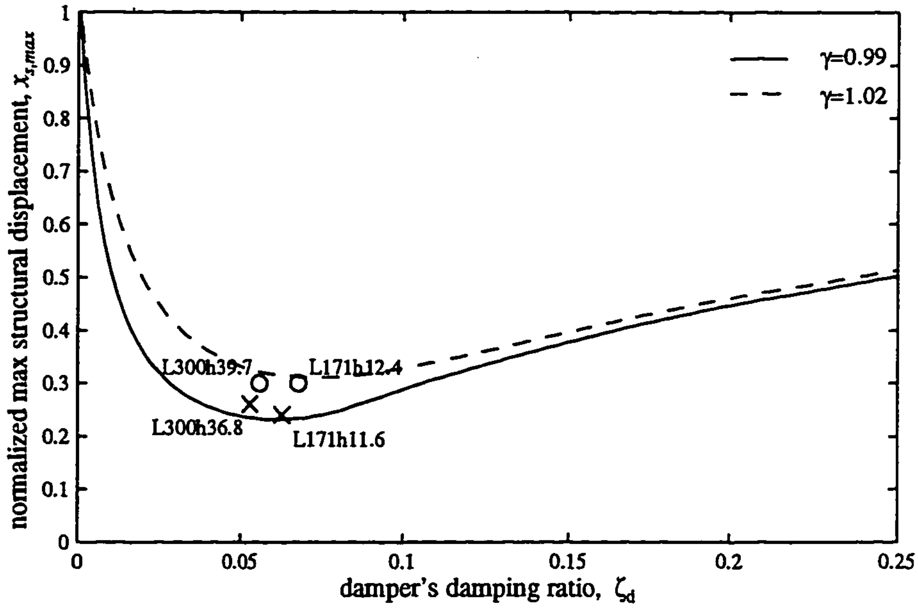

(b) $\ddot{x}_{s,\max}$ = 3 milli-g

Figure 4.14 Maximum structural displacements. Curves are for the structure equipped with linear TMDs with various tuning ratios. Circle-marks are for the structure equipped with linearly tuned liquid dampers. Cross-marks are for the structure equipped with nonlinearly tuned liquid dampers. The damping ratio of the structure, ζ_s=1.0 %. The mass ratio, μ=1.0 %.

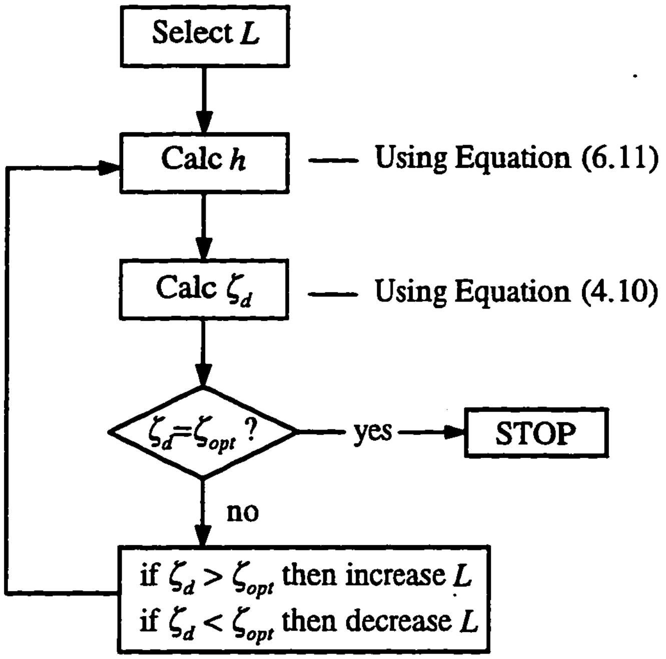

Figure 4.15 A scheme for selection of the most effective TLD for a given excitation amplitude. The TLD is characterized by an NSD model.

4.3 TLD performance and design procedure for white noise excitations

In this section, the behavior of the TLD coupled with a lightly damped SDOF structure is investigated for white noise excitation. An approximation solution scheme coupled with spectral analysis for the combined system is developed. The effectiveness is measured in terms of the reduction of the RMS value of the structural displacement. The approximation scheme is calibrated using the results from time-history analyses of the TLD.

4.3.1 Time history analysis

Consider a SDOF structure equipped with a TLD. The system can be modeled as a two-degree-of-freedom system using the NSD model for the TLD as shown in Figure 4.10. As the structure is subjected to a random forcing with a constant spectral density (white noise forcing), the equation of motion is written as Equation (4.2) and can be numerically solved as described in Section 4.1.

Fifty sets of 1200 Normally distributed random numbers with zero mean and unit variance were generated[1]. Each set of random numbers were smoothed using a cubic-spline fitting scheme. Twenty four equally distributed data points between each random number were added. Setting the time step between each data point equal to Δt=0.02 second, each data set becomes a 600-second white noise random number series.

The generated 50 sets of random number series were imposed as forcing functions on a SDOF structure equipped with various TLDs. The structure and TLDs which were employed for the case studies under harmonic excitation in Section 4.2.3 were selected, i.e., f_s=0.32 Hz, ζ_s=1.0 %, μ = 1.0 %, linearly or nonlinearly tuned TLDs with L=171 cm or 300 cm. The magnitudes of the random forcing functions were adjusted by trial and error such that the estimated maximum peak acceleration of the structure equipped with a

---

[1] Refer to the Matlab command "randn".

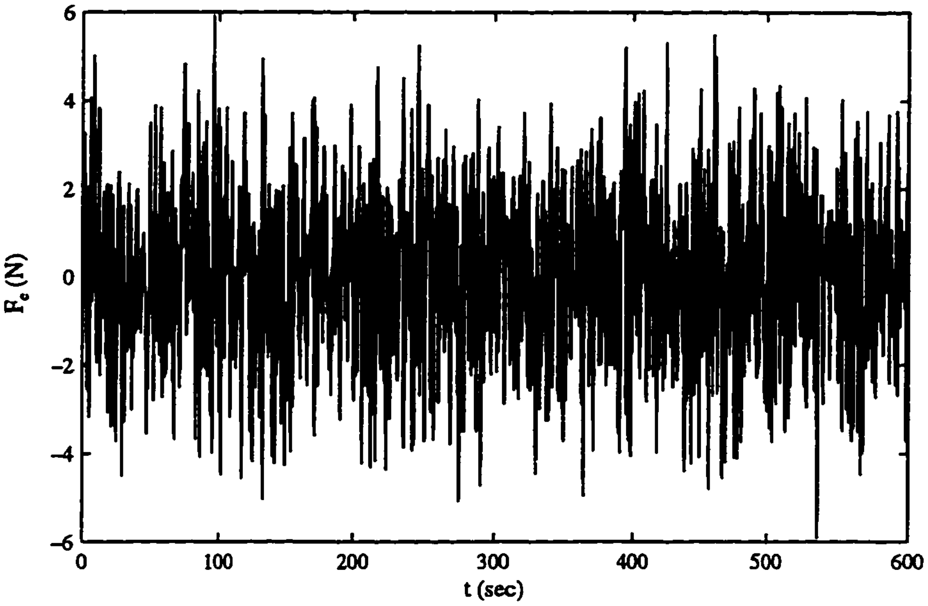

(a) White noise random forcing

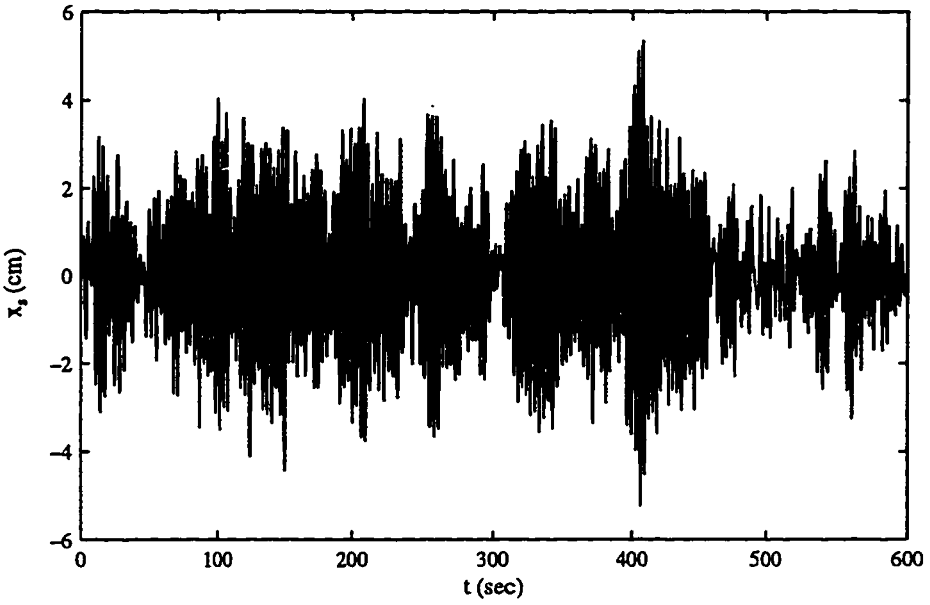

(b) Structural displacement induced by the random forcing

Figure 4.16 Sample plots of a generated white noise random forcing and the structural motion induced by the random forcing.

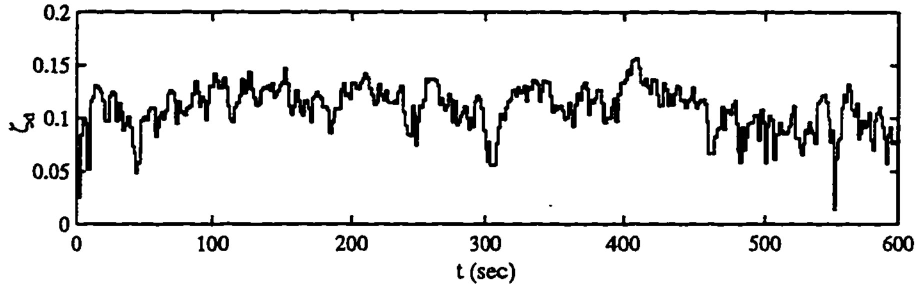

(a) Damping ratio, ζ_d

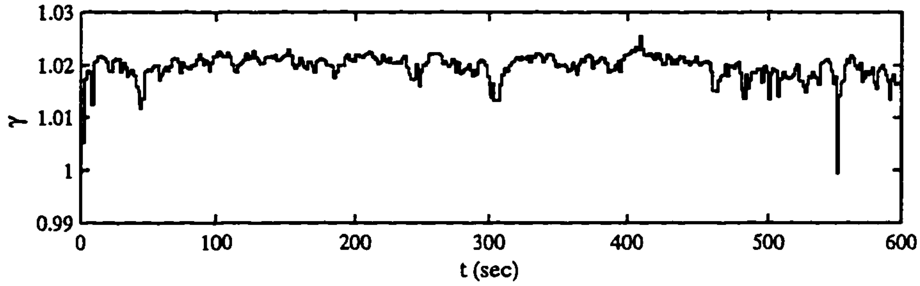

(b) Tuning ratio, γ

Figure 4.17 Sample time histories for the damping ratio and tuning ratio of the NSD model for the system described in Figure 4.16.

linearly tuned TLD with length L = 171 cm becomes 20 milli-g. One sample set of the generated random forcing function is plotted in Figure 4.16(a).

The adjusted random forcing functions were applied to the selected structural system equipped with TLDs. A sample time history of the structural displacements was plotted in Figure 4.16(b). The corresponding plots for the damping ratio ζ_d and frequency ratio γ of the NSD model are shown in Figure 4.17. After 300 seconds, the time histories for the structural responses and the stiffness and damping coefficients of the NSD model were recorded. The average results of the 50 loading cases were tabulated in Table 4.3.

Table 4.3 Responses of a SDOF structure with various TLDs under white noise excitation obtained from time history analyses.
($f_s = 0.32$ Hz, $\zeta_s = 1.0$ %, $\mu = 1.0$ %, targeted $\ddot{x}_{s,\max}$ =20 milli-g)

		L=171 cm		*L*=300 cm	
		h=12.4 cm (*1)	*h*=11.6 cm (*2)	*h*=39.7 cm (*1)	*h*=36.8 cm (*2)
x_s	rms (cm)	1.42	1.39	1.37	1.34
	max peak(cm)	4.56	4.44	4.44	4.30
	average peak (cm)	1.76	1.72	1.70	1.66
	max peak factor (α_{max})	3.21	3.20	3.24	3.22
	avg peak factor (α_{avg})	1.24	1.24	1.24	1.24
	reduction in rms (%)	34	36	36	38
	reduction in max (%)	27	29	29	31
$\ddot{x}_s$	rms (cm/s^2)	5.84	5.75	5.64	5.56
	max peak(cm/s^2)	19.3	18.8	18.7	18.3
	average peak (cm/s^2)	8.01	4.3.91	4.3.78	4.3.69
	max peak factor (α_{max})	3.30	3.27	3.32	3.29
	avg peak factor (α_{avg})	1.38	1.38	1.38	1.39
	reduction in rms (%)	34	35	36	37
	reduction in max (%)	27	28	29	30
ζ_d	average (%)	10.2	10.1	8.3	8.2
γ	average	1.02	0.99	1.02	0.98

Notes: (*1). Linearly tuned

(*2). Nonlinearly tuned

The maximum and average peak factors were defined as the ratio of the maximum and average peak responses, respectively, to the RMS (root mean square) response. The effectiveness is defined as the percent reduction of the RMS value of the structural displacement compared to the structure without TLD. In addition, the reductions of maximum displacement, RMS and maximum acceleration of the structure are presented for reference. The average values of ζ_d and γ of the NSD model during the recorded time duration for each TLD case were calculated and presented. The following summarize observations from the limited case studies:

- The maximum and average peak factors in the structural displacement were estimated as 3.2 and 1.25, respectively. These values will be used in the spectral analysis in the next section.
- The nonlinear tuning method developed for harmonic excitation as described in Equation (4.13) is also valid for white noise excitation, i.e., the tuning ratio of the NSD model of a nonlinearly tuned TLD approaches the optimal value for the linear TMD system.
- The damping of the NSD model can be adjusted by tank length.
- The effectiveness of the TLD increases as the ζ_d and γ of the NSD model approach the optimum values for the linear TMD system.

A detailed discussion about the effectiveness of the TLD will be presented in the next section.

4.3.2 Spectral analysis

The mean square response of a stationary process for a linear system under white noise excitation is calculated by

$$E[x_s^2] = S_0 \int_{-\infty}^{\infty} \left| H_{x_s}(\omega) \right|^2 d\omega \ , \tag{4.15}$$

in which S_0 is the constant spectral density of the random input forcing and $H_{x_s}(\omega)$ is the frequency response function of the structure. As described in Appendix C, the root mean square (RMS) response (displacement, $E\left[\sqrt{x_{s,0}^2}\right]$ *or* $x_{s,rms,wo}$) of the structure without a TLD is expressed as

$$E\left[\sqrt{{x_{s,0}}^2}\right] = \sqrt{\frac{\pi S_0}{2\zeta_s {m_s}^2 {\omega_s}^3}} = \sqrt{\frac{\pi S_0 \omega_s}{2\zeta_s {k_s}^2}} \; . \tag{4.16}$$

The RMS response of the structure equipped with a TLD is normalized to the RMS response of the structure without TLD. Through the solution procedure described in Appendix C, the normalized RMS displacement ($E'\left[\sqrt{x_s^2}\right]$ *or* $x_{s,rms}^{'}$) of the structure is calculated using the formula

$$E'\left[\sqrt{{x_s}^2}\right] = \sqrt{2\zeta_s \overline{\Pi}} \;\; , \tag{4.17}$$

where

$$\overline{\Pi} = \frac{-\overline{A}_1 - \overline{A}_3({\overline{B}_1}^2 - 2\overline{A}_0) + \overline{A}_0(\overline{A}_1 - \overline{A}_2\overline{A}_3)}{\overline{A}_0{\overline{A}_3}^2 + {\overline{A}_1}^2 - \overline{A}_1\overline{A}_2\overline{A}_3} \;\; , \tag{4.18}$$

$$\begin{gathered} \overline{A}_0 = \gamma^2; \quad \overline{A}_1 = 2(\zeta_s\gamma^2 + \zeta_d\gamma); \quad \overline{A}_2 = 4\zeta_s\zeta_d\gamma + 1 + \gamma^2(1+\mu); \\ \overline{A}_3 = 2(\zeta_s + \zeta_d(1+\mu)\gamma); \quad \overline{B}_0 = \gamma^2 = \overline{A}_0; \quad \overline{B}_1 = 2\zeta_d\gamma. \end{gathered} \tag{4.19}$$

The normalized RMS displacement of the structure, as described in Equation (4.16), is a function of μ, ζ_s, ζ_d and γ. The values of ζ_d and γ of the NSD model are functions of the peak structural displacement as seen in Equations (3.9) and (3.12). Because of the non-deterministic nature of the structural displacement under random vibration, it is essential to estimate the expected value of the peak structural displacement over a specific time period.

The maximum peak factor α_{max} is defined as the ratio of the maximum peak displacement to the RMS displacement of the structure. The average peak factor α_{avg} is defined as the ratio of the average peak displacement to the RMS displacement of the structure. The maximum and average peak factors of the structural motion under white noise excitation are estimated from a series of time history analyses. The expected maximum and average peak displacements of the structure can be estimated by multiplying the expected RMS structural displacement by the maximum and average peak factors, respectively. The corresponding values of ζ_d and γ of the NSD model are determined using Equations (3.9) and (3.12).

Figure 4.18 illustrates the schematic diagram of the solution procedure for the given system. Because of the nonlinearity of the TLD, an iterative process is required.

4.3.3 TLD performance under white noise excitation

Sample studies are conducted to evaluate the performance of TLDs interacting with a lightly damped SDOF structure. Equation (4.17) is solved using the proposed stochastic scheme. The convergence criterion for the iteration procedure is set equal to 1.0 %. The effectiveness of the TLD is assessed in terms of the reduction of the RMS displacement of the structure.

From 50 sets of sample time history analyses, which were described in Section 4.3.1, the maximum and average peak factors for the structural displacement were measured as approximately 3.2 and 1.25, respectively. These estimated peak factors are used in these sample studies.

The structure and TLDs which were employed for the case studies of time history analysis in the previous section are used in this investigation, i.e., $f_s = 0.32$ Hz, $\zeta_s = 1.0$ %, $\mu = 1.0$ % and linearly or nonlinearly tuned TLDs with $L = 171$ cm or 300 cm. In addition, the same size TLDs but with 10 % under-estimated water depth are investigated. The spectral density of the excitation force is determined such that the estimated maximum peak acceleration of the structure, equipped with a linearly tuned TLD, becomes approximately 20 milli-g. It is accomplished by the following procedure:

If it is assumed that the TLD reduces the maximum peak acceleration by approximately 35 %, the maximum peak acceleration of the structure without a TLD is estimated by

$$\ddot{x}_{s,peak,wo} = \frac{\ddot{x}_{s,peak}}{(1-0.35)} = 30.8\, milli - g\,. \tag{4.20a}$$

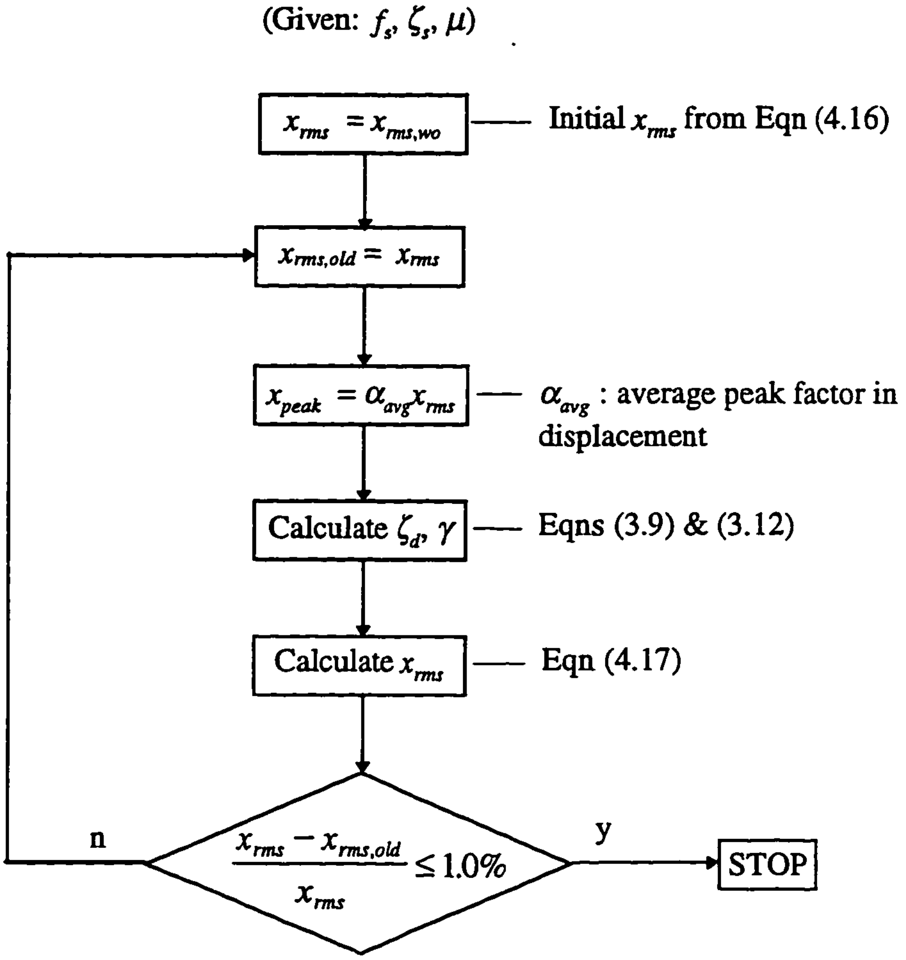

Figure 4.18 A solution procedure for the stochastic responses of a structure coupled with a TLD as the structure is subjected to white noise excitation. The TLD is characterized by the NSD model.

Dividing this result by the estimated maximum peak factor $\alpha_{max} = 3.2$, the targeted RMS acceleration of the structure without a TLD is estimated by

$$\ddot{x}_{s,rms,wo} = \frac{\ddot{x}_{s,peak,wo}}{\alpha_{\max}} = 9.6\ milli - g\,. \tag{4.20b}$$

The RMS displacement of the structure without a TLD is approximated by

$$x_{s,rms,wo} = \frac{\ddot{x}_{s,rms,wo}}{\omega_s^2} = \frac{(9.62)(0.981)}{(2\,\pi\,0.32)^2} = 2.33\ cm\,. \tag{4.20c}$$

Substituting this result into Equation (4.16), the spectral density of the white noise random forcing is determined as

$$S_0 = \frac{2\zeta_s \cdot \omega_s^3 m_s^2 x_{s,rms,wo}^s}{\pi} = 0.281 \cdot 10^{-4} \cdot m_s^2 \ \left[N^2 \big/ \mathrm{sec} \right]. \tag{4.20d}$$

The results of the spectral analyses are tabulated in Table 4.4. In comparing the results with the time history analysis results, it is observed that the spectral analyses yield

Table 4.4 Responses of a SDOF structure with various TLDs under white noise excitation obtained from the proposed stochastic analysis.
($f_s = 0.32$ Hz, $\zeta_s = 1.0$ %, $\mu = 1.0$ %, targeted $\ddot{x}_{s,\max}$ =20 milli-g)

		L=171 cm			*L*=300 cm		
		h=12.4 (*1)	*h*=11.6 (*2)	h=10.5 (*3)	*h*=39.7 (*1)	*h*=36.8 (*2)	*h*=33.0 (*3)
x_s	rms (cm)	1.43	1.40	1.46	1.38	1.35	1.45
	average peak (cm)	1.78	1.75	1.82	1.72	1.69	1.81
	reduction in rms (%)	39	40	37	41	42	38
ζ_d	average (%)	10.7	10.6	10.8	8.7	8.6	8.8
γ	average	1.02	0.99	0.94	1.02	0.98	0.94

Notes: (*1). Linearly tuned
(*2). Nonlinearly tuned
(*3). Mis-tuned (approximately 10 % error in water depth)

approximately 5 % higher values of the effectiveness of the TLDs. It is assumed that this error is caused by approximations in estimating parameters for the spectral solution procedure.

4.3.4 TLD design procedure for white noise excitation

Consider a SDOF structure equipped with a linear TMD system. The normalized RMS displacement $x_{s,rms}'$ of the structure, as described in Equation (4.17), is a function of ζ_d and γ for the given values of μ and ζ_s. Figure 4.19 contains the plots of $x_{s,rms}'$ vs. ζ_d of the linear TMD system with two values of tuning ratios ($\gamma = 0.99$ and 1.02)[1]. The solid curve is for the case with the damper tuning ratio γ of 0.99 which corresponds to the cases with nonlinearly tuned TLDs in Table 4.4. The dashed curve is for the case with the damper tuning ratio γ of 1.02 which corresponds to the cases with linearly tuned TLDs.

The results of the sample case studies using the spectral analyses are shown in Figure 4.19(a). The results from the time history analyses are presented in Figure 4.19(b). As discussed previously, the approximate 5 % over-estimation of the TLD effectiveness from the spectral analysis compared with the time history analysis results is apparent. It is concluded that the most effective TLD for the system under white noise excitation can be determined using the spectral analysis procedure coupled with the searching scheme described in Figure 4.15.

---

[1] See Figure C.2 for the same plots for the system with various tuning ratios.

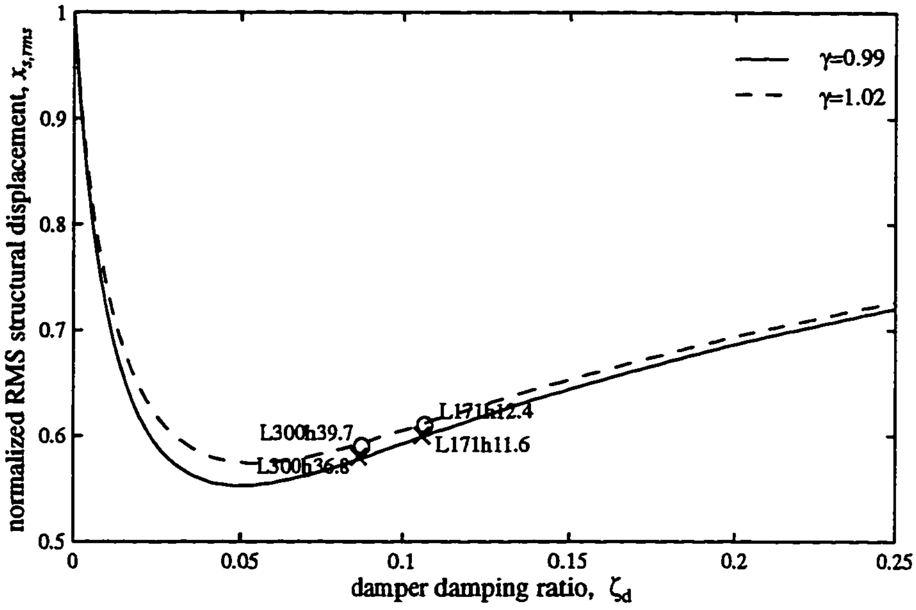

(a) The results from spectral analyses

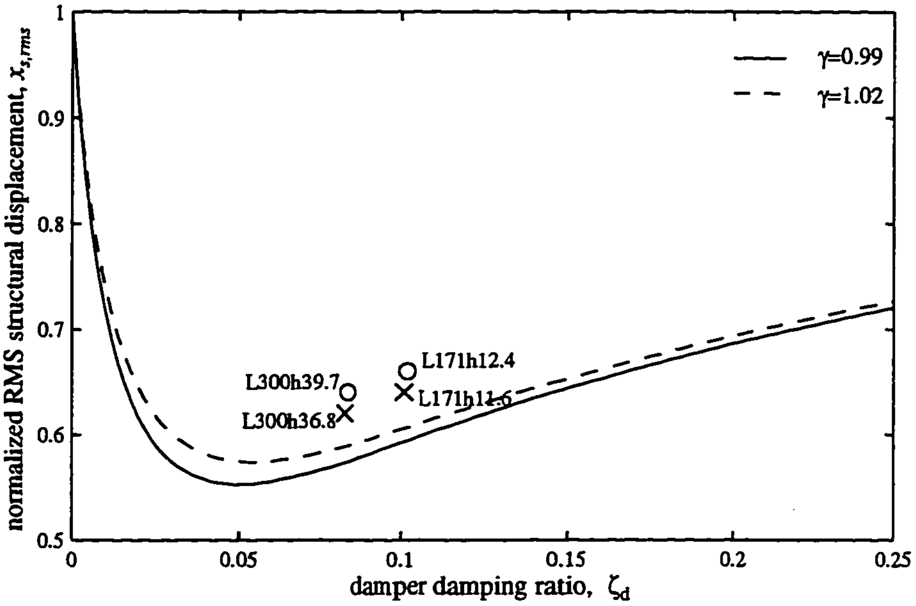

(b) The results from time history analyses

Figure 4.19 The results from sample spectral analyses and time history analyses as compared with a family of curves for the system with a linear TMD system.

4.4 TLD performance under wind conditions

In this section, the performance of TLDs coupled with a lightly damped SDOF structure is investigated using the time series analyses as the structure is subjected to wind pressure loadings. The influence of TLD nonlinearity on its effectiveness is evaluated.

Reed (1983) proposed the ARIMA time series model for wind pressure loadings. For the windward region, Reed proposed an autoregressive model of order 2 (AR(2)) as

$$P_i = \phi_1 P_{i-1} + \phi_2 P_{i-2} + a_t, \tag{4.21}$$

where ϕ_1=1.1450, ϕ_2=-0.2369 and a_t indicates a series of Normally distributed random shocks. Using the AR(2) model, 50 sets of time series of wind pressure loadings were generated. Each series is composed of 30,000 numbers. Setting the sample interval equal to $\Delta t = 0.02$ second, each data set covers 600-seconds.

To investigate the performance of the TLD under wind conditions, the generated wind pressure series were imposed on a SDOF structure equipped with a TLD. By modeling the TLD as the NSD model, the equation of motion of the system is written as Equation (4.2). The dynamic response of the structure were obtained by numerically solving the equation as described in Section 4.1.1.

A SDOF structure and TLDs which were employed for the case studies under harmonic or white noise excitations in the previous sections were selected, i.e., f_s = 0.32 Hz, ζ_s = 1.0 %, μ = 1.0 % and linearly and nonlinearly tuned TLDs with length L = 171 cm and 300 cm, respectively. The data for the case studies are tabulated in Table 4.5.

Because of the nonlinear characteristics of the TLD, the target excitation amplitude was determined first. In this case study, the behavior of the TLD for the maximum structural acceleration of 20 milli-g was targeted. The magnitudes of the wind pressure series were adjusted by trial and error such that the estimated maximum peak acceleration of the structure equipped with a linearly tuned TLD became approximately targeted 20 milli-g.

A sample set of the simulated time series for wind pressure is presented in Figure 4.20(a). The corresponding displacements of the structure equipped with a TLD are presented in Figure 4.20(b). The corresponding plots for the damping ratio ζ_d and tuning ratio γ of the NSD model are shown in Figure 4.21.

Table 4.5 Responses of a SDOF structure with various TLDs as the structure is subjected to wind. ($f_s = 0.32$ Hz, $\zeta_s = 1.0$ %, $\mu = 1.0$ %, targeted $\ddot{x}_{s,\max}$ =20 milli-g)

		L=171 cm		*L*=300 cm	
		h=12.4 cm (*1)	*h*=11.6 cm (*2)	*h*=39.7 cm (*1)	*h*=36.8 cm (*2)
x_s	rms (cm)	2.12	2.08	2.07	2.02
	max (cm)	7.01	6.89	6.86	6.72
	average peak (cm)	2.17	2.11	2.10	2.03
	peak factor	3.30	3.31	3.31	3.31
	reduction in rms (%)	26	27	28	29
	reduction in max (%)	21	22	22	24
$\ddot{x}_s$	rms (cm/s^2)	6.81	6.65	6.54	6.40
	max (cm/s^2)	21.8	21.3	21.2	20.6
	average peak (cm/s^2)	9.20	9.04	8.91	8.76
	peak factor	3.21	3.2	3.24	3.22
	reduction in rms (%)	34	37	38	40
	reduction in max (%)	27	30	29	33
ζ_d	average (%)	10.7	10.6	8.7	8.6
γ	average	1.02	0.99	1.02	0.98

Notes: (*1). Linearly tuned

(*2). Nonlinearly tuned

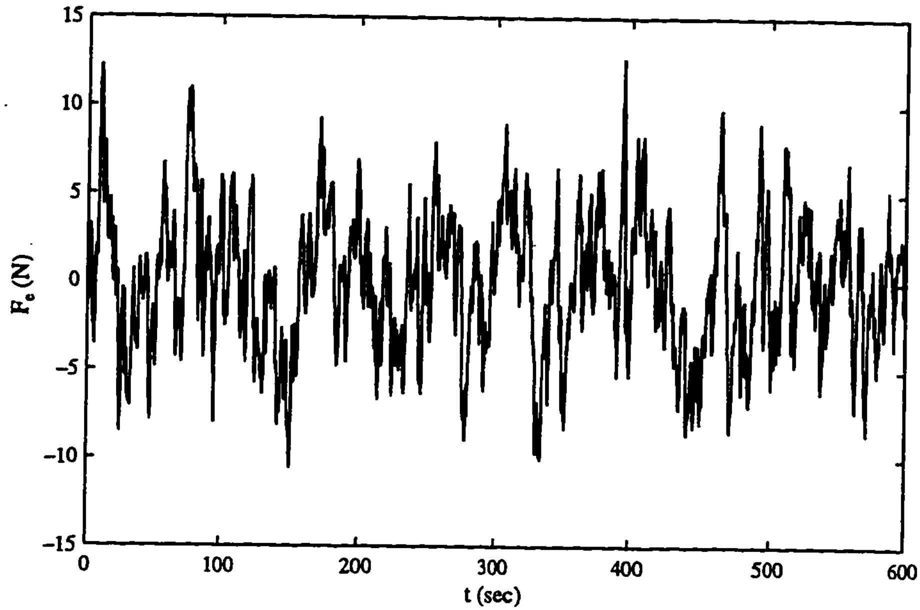

(a) Simulated time series for wind pressure

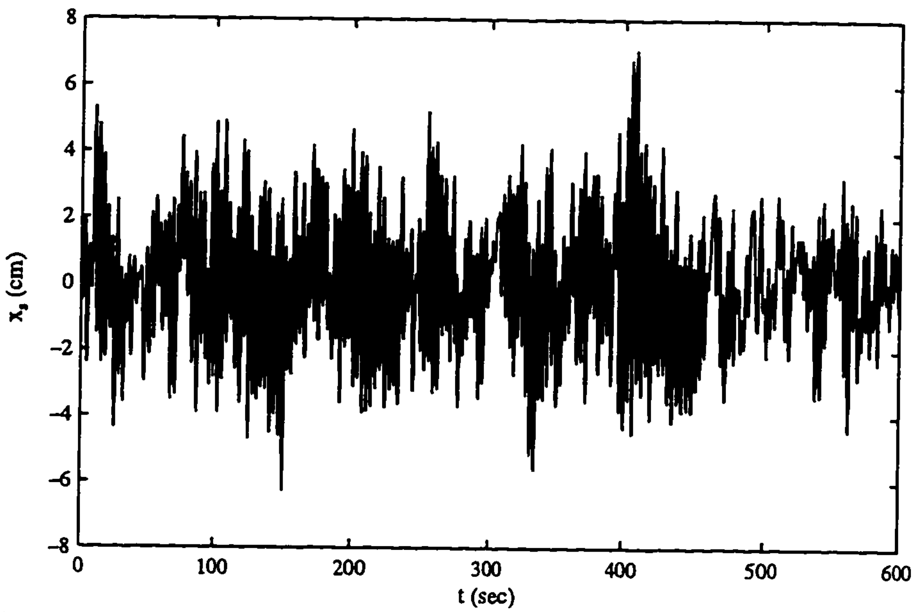

(b) A time series of the displacement of the structure with a TLD

Figure 4.20 A sample set of the simulated time series for wind pressure using the AR(2) model and the structural displacement with a TLD under this wind pressure loading. The properties of the structure and the TLD are: $f_s = 0.32$ Hz; $\zeta_s = 1.0$ %; $\mu = 1.0$ %; $L = 171$ cm; $h = 12.4$ cm.

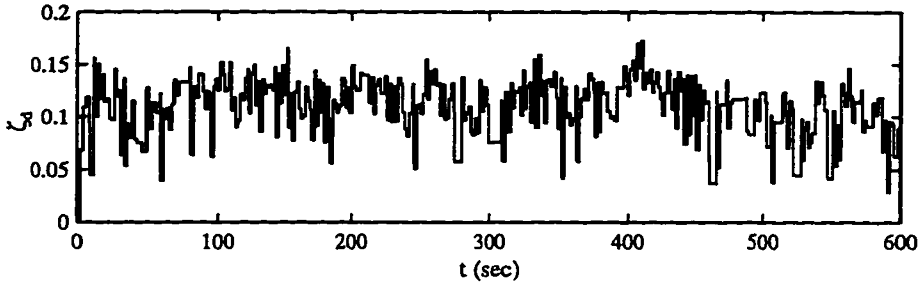

(a) Damping ratio, ζ_d

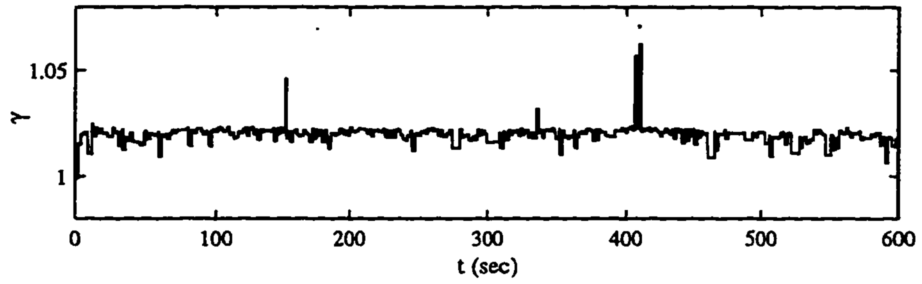

(b) Tuning ratio, γ

Figure 4.21 Time histories of ζ_d and γ of the NSD model for the case of Figure 4.20.

It is assumed that the TLD activated fully after 300 seconds. The time histories of the structural responses and the stiffness and damping coefficients of the NSD model were recorded. The average results of the 50 loading cases for each system are tabulated in Table 4.5. The peak factors were defined as in the previous section. To assess the effectiveness of the TLD, the reduction in the RMS and the maximum values of the displacement and acceleration of the structure equipped with each TLD were compared to those of the same structure without the TLD. The average damping ratio ζ_d and tuning ratio γ of the NSD model for each case were estimated.

The results described in Table 4.5 display trends similar to those observed in the time history analyses of the TLD for white noise excitation. To summarize:

- The nonlinear tuning method developed for harmonic excitation as described in Equation (4.13) is also valid for AR(2) wind pressure excitation, i.e., the tuning ratio of the NSD model of a nonlinearly tuned TLD approaches the optimal value for the linear TMD system.
- The damping of the NSD model can be adjusted by tank length.
- The effectiveness of the TLD increases as the average values of ζ_d and γ of the NSD model approach the optimum values for the linear TMD system.

4.5 Behavior of the TLD under earthquake excitation

The performance of TLDs attached to a lightly damped structure subjected to earthquake ground motion is investigated. Because the NSD model was derived for the harmonic excitation, validity of the model to an earthquake situation was verified using shaking table experiments prior to the performance investigation.

4.5.1 Validity of the NSD model for the earthquake condition

The NSD model was derived under the conditions of harmonic excitation with sweep frequencies. To verify the effectiveness of the model under earthquake motion, shaking table experiments were conducted.

Consider a SDOF structure equipped with a TLD. As the structure is subjected to earthquake motion, the TLD reacts to the structural motion. To simulate the behavior of the TLD for earthquake motion, the TLD must be excited by the structural motions corresponding to the earthquake. As a SDOF structure is subjected to base excitation, the equation of motion of the system is written as Equation (A.1) in Appendix A. The dynamic responses of the structure can be obtained by numerically solving the equation.

Figures 4.22 (a) and (b) show the ground motions for the 1940 El Centro earthquake obtained from "NCEER Strong-Motion Data Base". These ground motions were imposed numerically on an undamped SDOF structure whose natural frequency is $f_s = 0.5$ Hz. The dynamic responses of the structure were numerically simulated. Because the maximum allowed displacement of the shaking table is approximately 50 mm, the total structural displacement, x_s, was scaled down such that the maximum absolute value of x_s becomes approximately 40 mm. The scaled shaking table motions were plotted in Figure 4.22 (c).

A TLD with length L = 590 mm and water depth h = 36 mm was mounted on the shaking table as illustrated in Figure 2.1. Its linear fundamental natural frequency is 0.506 Hz which is approximately the same as that of the selected structure. The table was excited in the motions shown in Figure 4.22 (c) which were the scaled total displacements

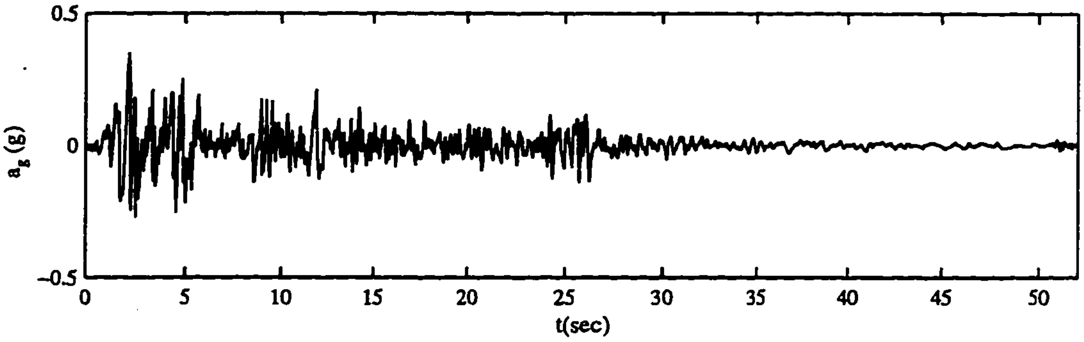

(a) Ground acceleration

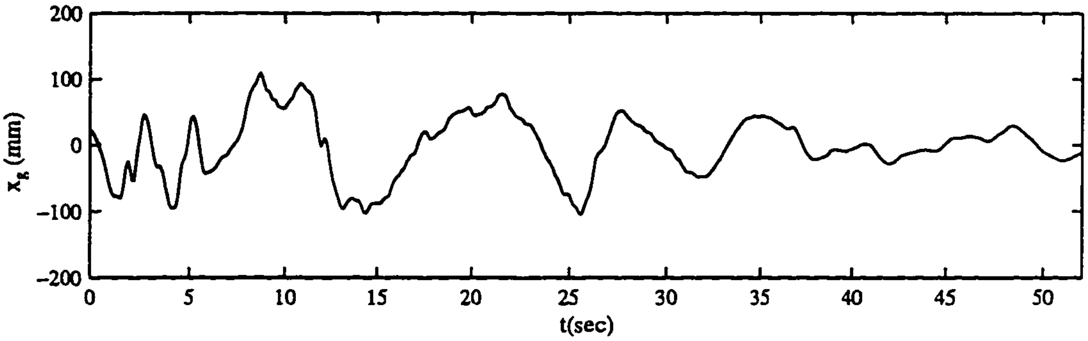

(b) Ground displacement

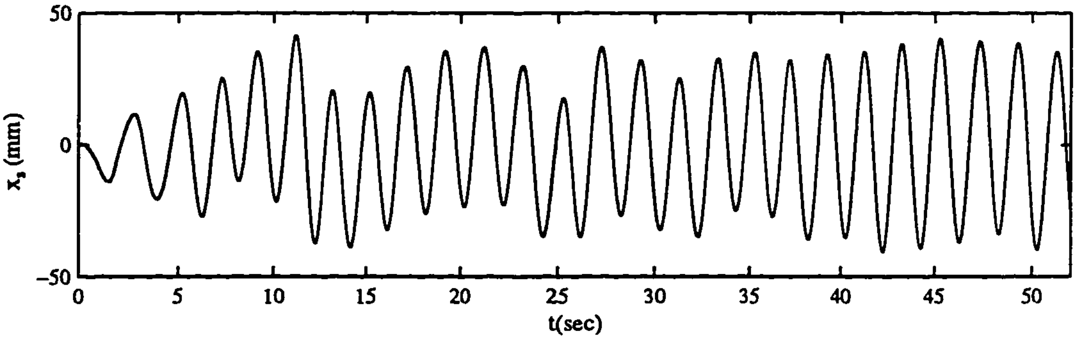

(c) Scaled total structural displacement

Figure 4.22 Ground motions during the El Centro earthquake obtained from "NCEER Strong-Motion Data Base" and scaled total displacements of a undamped structure with natural frequency $f_s = 0.5$ Hz.

of the selected structure under the El Centro earthquake. The base shear generated by the TLD during the entire excitation period was measured with the loadcell and recorded in Figure 4.23 (a) with a solid curve. The amount of energy dissipation due to the base shear during each half cycle was calculated and recorded in Figure 4.23 (b) with a solid curve.

The NSD model for the employed TLD was assumed to be subjected to the same excitation of the shaking table. The equation of motion for the system is expressed as Equation (A.1) in Appendix A. The dynamic responses of the NSD model to the base excitation were obtained numerically. The time history of the base shear generated by the NSD model is presented in Figure 4.23 (a) with a dashed curve. The amount of energy dissipation due to the base shear during each half cycle was calculated and recorded in Figure 4.23 (b) with a dashed curve.

In both plots, it is apparent that the solid curve and the dashed curve are in close agreement. The result indicates that the NSD model which has been derived from the shaking table experiments for harmonic excitations predicts accurately the behavior of the TLD under the El Centro earthquake motion. Figure 4.24 presents the time histories of the damping ratio and the stiffness hardening ratio of the NSD model during the excitation period.

4.5.2 Performance of the TLD under earthquake

Numerical simulation was used to investigate the performance of the TLD attached to a lightly damped SDOF structure subjected to the 1994 Northridge earthquake. The ground motions of the Northridge earthquake obtained from "NCEER Strong-Motion Data Base" and shown in Figure 4.25 are obviously different from the El Centro records. The structure with $f_s = 0.32$ Hz and $\zeta_s = 1.0$ % was selected. The TLD with length $L =$ 171 cm and water depth $h_0 = 11.6$ cm was attached to the structure. The mass ratio of the TLD was set equal to $\mu = 1.0$ %.

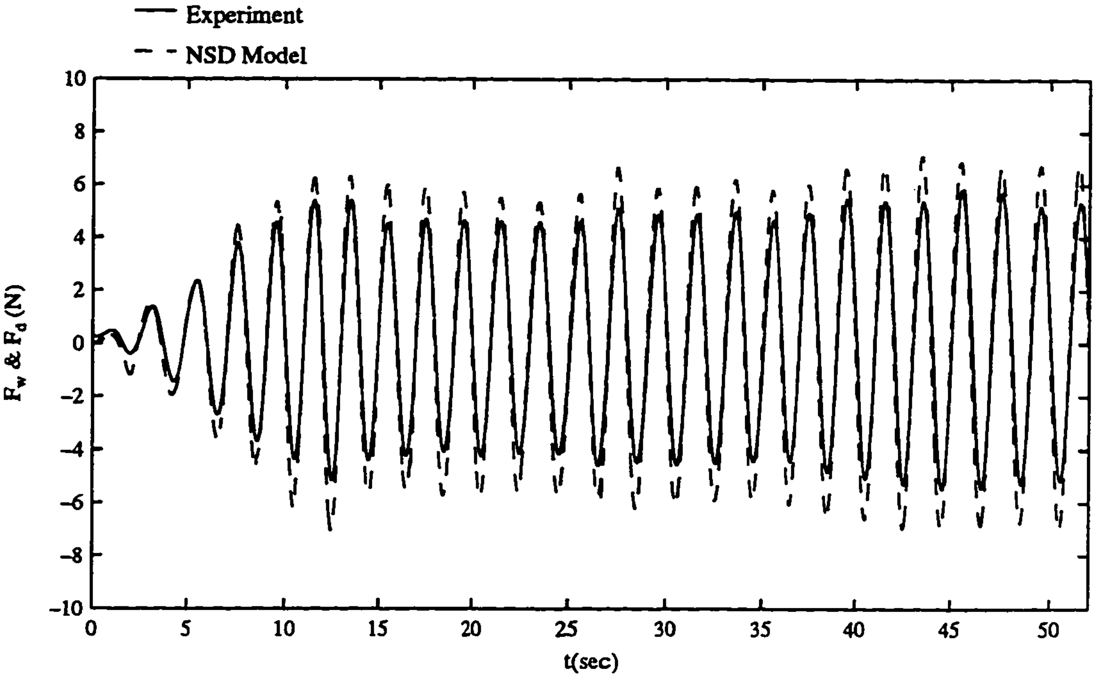

(a) Damping forces

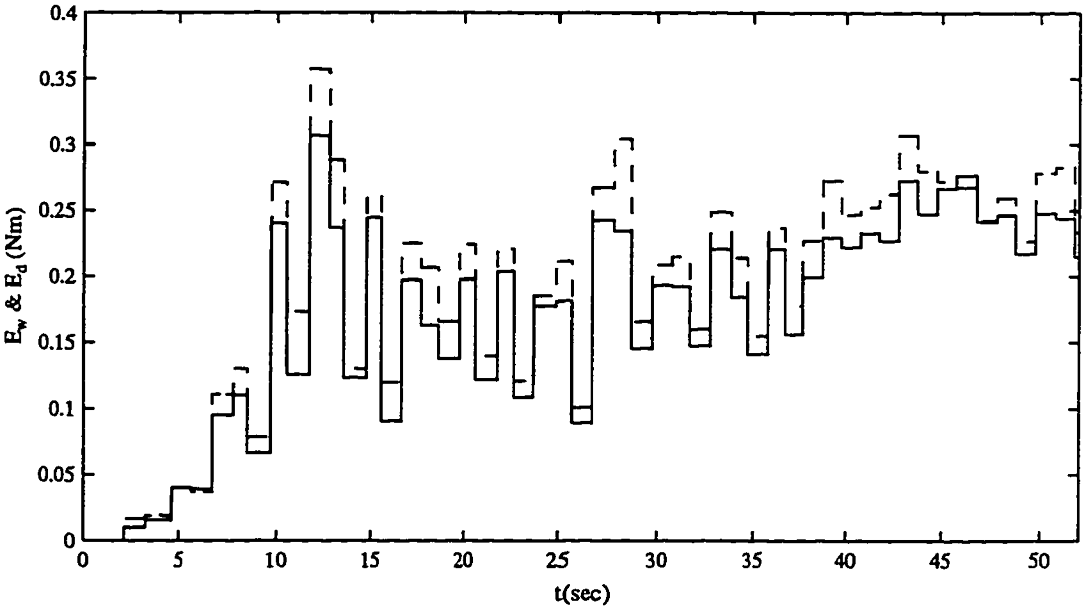

(b) Energy dissipation per cycle

Figure 4.23 Damping forces and energy dissipation per cycle generated by the TLD with the length $L = 590$ mm, water depth $h_0 = 36$ mm and its corresponding NSD model. The maximum shaking table displacement $x_{s,max}$ was adjusted to approximately 40 mm.

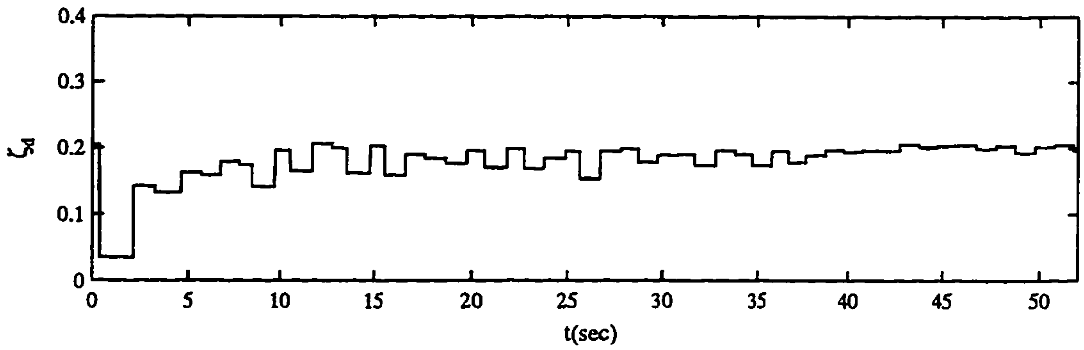

(a) Damping ratio, ζ_d

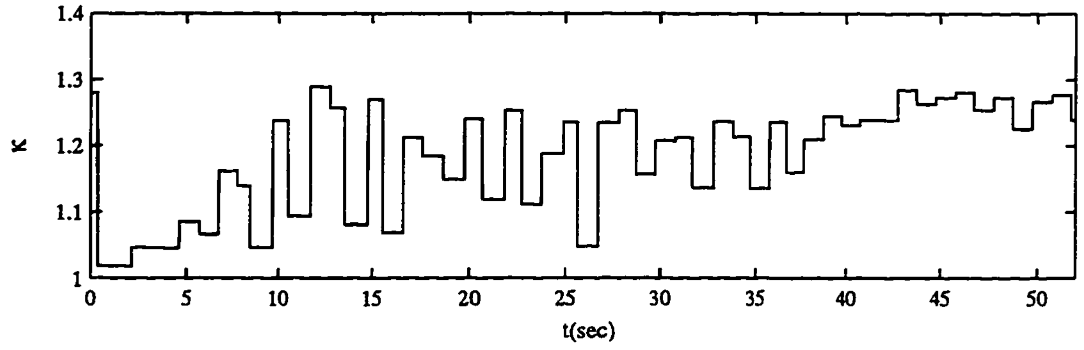

(b) Stiffness hardening ratio, κ

Figure 4.24 Time histories for ζ_d and κ of the NSD model for the case of Figure 4.23.

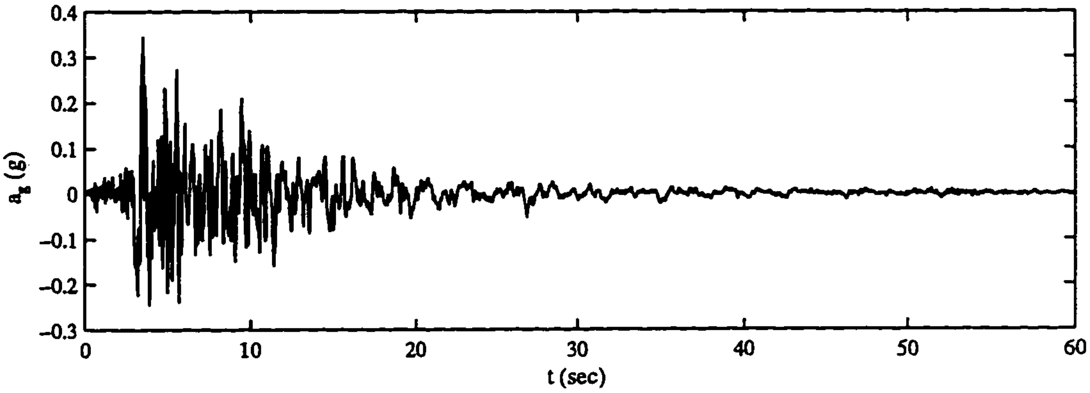

(a) Ground acceleration

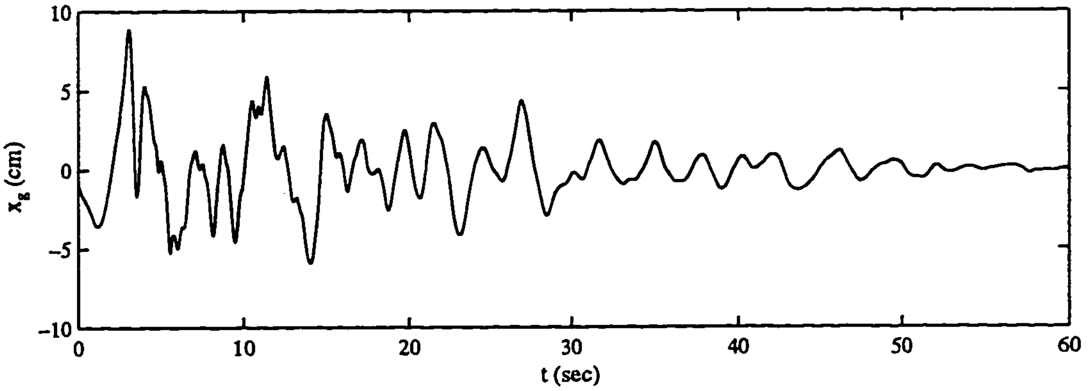

(b) Ground displacement

Figure 4.25 Time history records of ground motions during the 1994 Northridge earthquake. The records were obtained from "NCEER Strong-Motion Data Base - 1990".

By modeling the TLD as a NSD model, the equation of motion of the system is written as in Equation (4.2). The dynamic responses of the structure are obtained by numerically solving the equation as described in Section 4.1. One 60 second record of the responses (displacement and acceleration) of the structure with and without a TLD are plotted together in Figure 4.26. The reduction of the maximum and the RMS responses during every 20 second intervals are averaged and recorded in the plots.

It appears that the TLD does not play any significant role during the initial period of ground motion. This is because the structural motion during this stage is not periodic; consequently, the TLD is not properly tuned to the structural motion. But as time passes, the structural motion becomes more periodic in nature. The TLD which is tuned to the structural natural frequency begins to gain effectiveness. During the last 20 second period, the effectiveness of the TLD increases to approximately 50 % in terms of the RMS displacement or acceleration. However, because the "impact" of the earthquake in the initial seconds is crucial to the structural safety, the TLD must be further investigated to improve its performance for this type of nonstationary motion. Figure 4.27 presents the time histories of the damping and the tuning ratios of the NSD model during the excitation period.

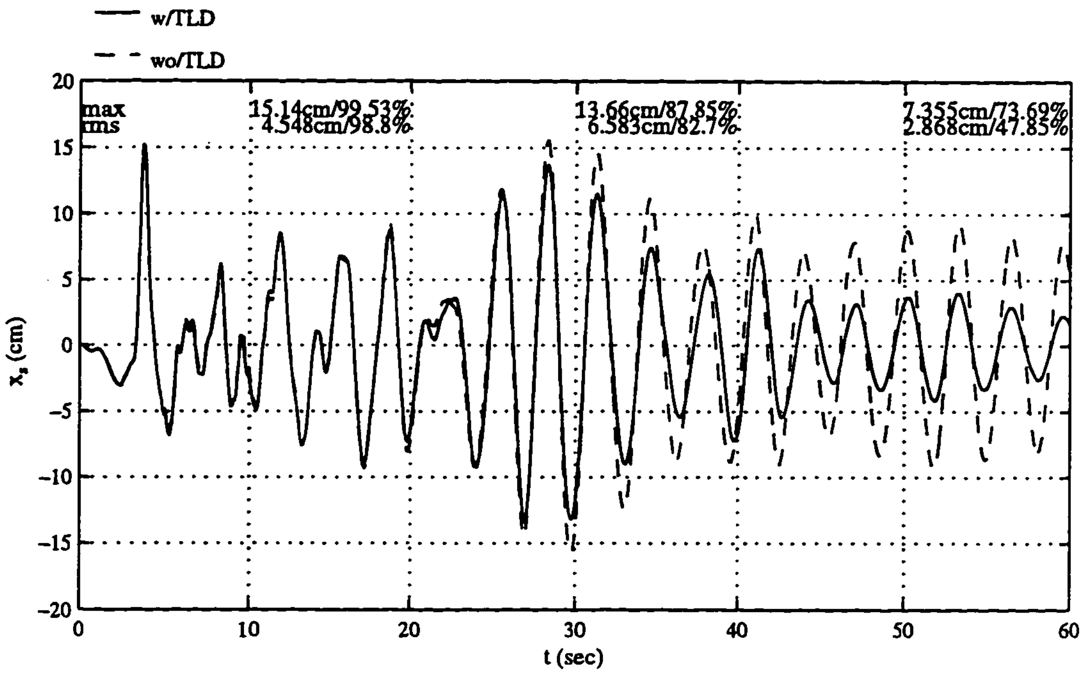

(a) Structural displacement

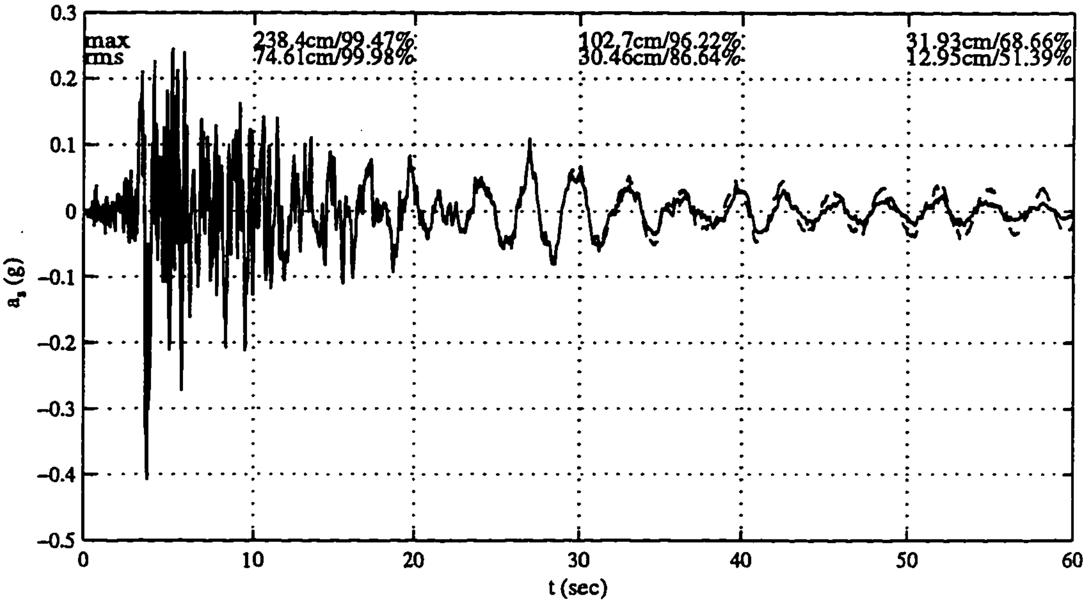

(b) Structural acceleration

Figure 4.26 Time history responses of the structure with and without a TLD under the Northridge earthquake. Structure with f_s = 0.32 Hz and ζ_s = 1.0 %; TLD with L = 171 cm, h_0 = 11.6 cm and μ = 1.0 %.

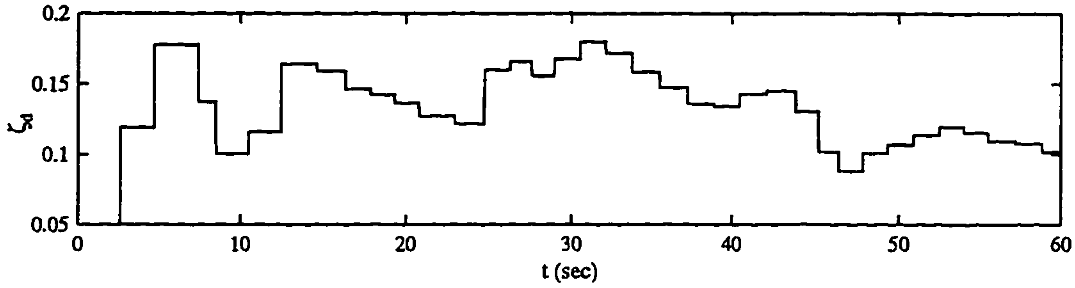

(a) Damping ratio, ζ_d

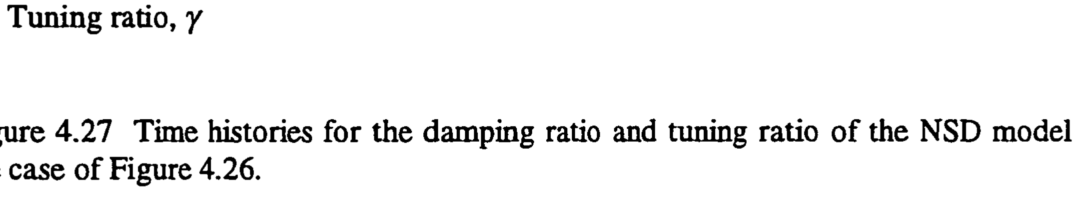

(b) Tuning ratio, γ

Figure 4.27 Time histories for the damping ratio and tuning ratio of the NSD model for the case of Figure 4.26.

CHAPTER 5

CONCLUSIONS

The fundamental behavior of shallow water sloshing motion in TLDs was investigated experimentally and numerically. The results reveal the following:

- Shallow water possesses hardening-spring type nonlinear characteristics. The nonlinearity is dependent upon the excitation amplitude.
- The nonlinearity of the TLD was quantified using the parameter "jump-frequency". The jump-frequency may be explicitly expressed as a function of nondimensional excitation amplitude, $\Lambda = \frac{A}{L}$.
- Regions of weak wave breaking and strong wave breaking were identified. In the region of strong wave breaking, the nonlinear behavior changes more rapidly.
- As the excitation amplitude increases, the frequency range for which the damper is effective widens. This fact indicates that the TLD performs in a wider frequency range under strong excitation, i.e., it is a robust energy-dissipating system.
- Higher frequency components of the water sloshing motion do not influence significantly the energy dissipation capacity of the TLD. An approximate analysis method using only the fundamental mode is valid.
- The damping forces due to water sloshing motion can be adequately calculated based on the hydrostatic pressure assumption at the end walls of the rectangular tank.

An equivalent TMD of the rectangular TLD (NSD model) was developed based upon the shaking table experiments. The damping ratio and the stiffness hardening ratio of the NSD model were explicitly expressed as functions of the parameter (A/L). In the weak wave breaking region, the stiffness of the NSD model changes only slightly and remains approximately constant at a value of 1.05. In the strong wave breaking region, the stiffness changes rapidly. This phenomenon is consistent with the jump-frequency investigation.

Although the water sloshing motion in a circular tank is more complex than that in the rectangular one, preliminary experimental results suggest it may be treated as an equivalent rectangular tank for design purposes.

A numerical scheme to solve the shallow-water equation using the Random Choice Method (RCM model) proposed by Gardarsson and Yeh (1994) predicts quite accurately the water sloshing motion in the region of weak wave breaking, i.e. $A/L < 0.03$. However, the RCM model cannot simulate accurately the water sloshing with strong wave breaking that occurs in the excitation range $A/L > 0.03$.

Based on the observed nonlinearity of the TLD, nonlinear tuning was proposed. The nonlinearly tuned TLD was shown to perform more effectively than the linearly tuned one.

Numerical solution schemes in the time domain for interaction of the TLD with a SDOF structure were developed. The behavior of the TLD was simulated using the NSD and the RCM models, respectively. These solution schemes were employed to evaluate the TLD performance under various excitation conditions.

Iterative solution procedures for the frequency responses of a SDOF structure equipped with a TLD were proposed for the structure subjected to harmonic or white noise excitations. Using the solution schemes, the parameters of the NSD model may be determined. The effectiveness of the TLD may be estimated using the proposed frequency response method.

The performance of TLDs attached to lightly damped structures was evaluated using the proposed numerical solution schemes for the structure under various excitation conditions (harmonic forcing, white noise forcing, wind or earthquake). The results of extensive numerical investigations reveal the following:

- For harmonic or white noise excitations, the optimization of the parameters for the NSD model follows that of the traditional linear TMD. The nonlinear tuning enhances the performance of the TLD.

- Effectiveness of TLDs was evaluated for a structural system subjected to typical time-varying wind pressure loadings. The wind pressure loading was simulated using an AR(2) model proposed by Reed (1983). These preliminary results from the time-history numerical analyses show that the selected TLDs reduce the RMS structural accelerations up to 40 %. This result illustrates the viability of the NSD model. Further investigation of the TLD performance for time series representation of various wind loadings is warranted.

- The effectiveness of the TLD under earthquake conditions was investigated numerically. Northridge earthquake ground motions were imposed on a lightly damped SDOF structure equipped with a nonlinearly tuned TLD. The TLD does not reduce the structural response during the initial stage of the earthquake. This limitation indicates the inability of this passive system for damping "impact-type" loadings. The performance of the TLD for earthquake loadings must be further investigated.

REFERENCES

Ayorinde, E.O. and Warburton, G. B., 'Minimizing structural vibration with absorbers', Earthquake Engineering and Structural Dynamics. Vol. 8, 219-236, 1980.

Benito, M., Pacheco, M. and Fujino, Y., 'Perturbation Technique to Approximate the Effect of Damping Nonproportionality in Modal Dynamic Analysis', JSCE, Structural Engineering / Earthquake Engineering, Vol. 6, No. 1, 169-178, 1989.

Blevins, R.D., Formulas for Natural Frequency and Mode Shape, Robert E. Krieger Publishing Company, Malaber, Florida, pp. 368.

Chaiseri, P., Fujino, Y., Pacheco, B. M. and Sun, L. M., 'Interaction of Tuned Liquid Damper (TLD) and Structure - Theory, Experimental Verification and Application.' J. Structural Engineering / Earthquake Engineering, Proc. JSCE, Vol. 6, No. 2, 273-282,1989.

Chester, W., 'Resonant Oscillation of Water Waves. I. Theory & II. Experiment.' Proceedings, Royal Society of London, A306, pp.5-39, 1968.

Den Hartog, J. P., 'Two degree of freedom', Mechanical Vibrations, 4th ed, McGraw-Hill, New York, pp. 79-120, 1956.

Faltinson, O.M., 'A Numerical Nonlinear Method of Sloshing in Tanks with Two-Dimensional Flow.' J. of Ship Research, Vol.22, pp.193-202, 1978.

Fediw, A. A., Breukelman, B., Morrish, D. P. and Isyumov, N., 'Effectiveness of a Tuned Sloshing Water Damper to Reduce the Wind-Induced Response of Tall Buildings', Proc. of the 7th U.S. National Conference of Wind Engineering, Vol. 1, Los Angeles, June 27-30, p233-242, 1993.

Fediw, A. A., Isyumov, N. and Vickery, B. J., 'Performance of a One Dimensional Tuned Sloshing Water Damper', to be presented at the 1st IAWE European and African Regional Conference, Guernsey, September, 1993.

Fediw, A. A., Isyumov, N., Morrish, D. P. and Breukelman, B., 'Dynamic Behaviour of a Tall Reinforced Concrete Building', ASCE Structures Congress '92, San Antonio, Texas, April, 1992.

Friberg, P. A. and Susch, C. A., 'A User's Guide to Strongmo: Version 1.0 of NCEER's Strong-Motion Data Access Tool for Pcs and Terminals', Lamont-Doherty Geological Observatory of Columbia University, Palisades, New York, 1990.

Fujii, K., Tamura, Y., Sato, T. and Wakahara, T., 'Wind-Induced Vibration of Tower and Practical Applications of Tuned Sloshing Damper,' J. of Wind Engineering, Japan Association for Wind Engineering, No. 37, pp. 537-546, 1988.

Fujii, K., Tamura, Y., Sato, T. and Wakahara, T., 'Wind-Induced Vibration of Tower and Practical Applications of Tuned Sloshing Damper,' J. of Wind Engineering and Industrial Aerodynamics, 33, 263-272, 1990.

Fujino, Y. and Abe, M., 'Design Formulas for Tuned Mass Dampers Based on a Perturbation Technique', Earthquake Engineering and Structural Dynamics, Vol. 22, 833-854, 1993.

Fujino, Y., et al., 'Tuned Liquid Damper (TLD) for Suppressing Horizontal Motion of Structures', ASCE, J. of Engineering Mechanics, Vol. 118, No. 10, 1992.

Fujino, Y., Pacheco, B. M., Chaiseri, P. and Sun, L. M., 'Parametric Studies on Tuned Liquid Damper (TLD) Using Circular Containers By Free-Oscillation Experiment', J Structural Engineering / Earthquake Eng., JSCE., Vol. 5, No. 2, pp. 381-391, 1988.

Gardarsson, S. and Yeh, H., 'Numerical Simulations of Bores using the Random Choice Method', Proc. the 3rd UJNR Workshop, 1994.

Housner, C.W., 'Dynamic pressure on accelerated fluid containers', Bulletin of the Seismological Society of America, 1959.

Igusa, T. and Der Kiureghian, A., 'Dynamic characterization of two degree of freedom equipment-structure systems', J. Engineering Mechanics, ASCE 111, 1-19, 1985.

Igusa, T. and Xu, K., 'Vibration Reduction Characteristics of Distributed Tuned Mass Dampers', Proc., 4th Intl. Conf., Structural Dynamics: Recent Advances, Southampton, UK, 1991, pp. 596-605.

Igusa, T. and Xu, K., 'Vibration Control using Multiple Tuned Mass Dampers', J. of Sound and Vibration, 175(4), pp. 491-503, 1994.

Kareem, A. and Sun, W. J., 'Stochastic Response of Structures with Fluid-Containing Appendages', J. of Sound and Vibration, Vol. 119, No. 3, 1987.

Kareem, A., 'Acrosswing Response of Buildings', ASCE, J. Structural Division, Vol. 108, No. ST4, 1982.

Kareem, A., 'Mitigation of Wind Induced Motion of Tall Buildings', J. of Wind Engineering and Industrial Aerodynamics, Vol. 11, 1983.

Kareem, A., 'Reduction of Wind Induced Motion Utilizing a Tuned Sloshing Damper', J. of Wind Engineering and Industrial Aerodynamics, Vol. 36, 1990.

Kareem, A., 'Serviceability Issues and Motion Control of Tall Building', Structures Congress 92, ASCE, pp476-479, 1992.

Kareem, A., 'Tuned Liquid Dampers: Past, Present and Future', Proceedings of the Seventh U.S. National Conference on Wind Engineering, 1993.

Kareem, A., 'Wind Induced Response of Buildings: A Serviceability Viewpoint', AISC, Proceedings of the National Engineering Conference, Miami Beach, Florida, 1988.

Keulegan, G.R.L., 'Energy Dissipation in Standing Waves in Rectangular Basins.' J. Fluid Mechanics, Vol. 6, pp.33-50, 1959.

Koh, C. G., Mahatma, S. and Wang, C. M., 'Theoretical and Experimental Studies on Rectangular Liquid Dampers under Arbitrary Excitations', Earthquake Engineering and Structural Dynamics, Vol. 23, 17-31, 1994.

Koh, C. G., Mahatma, S. and Wang, C. M., 'Reduction of Structural Vibrations by Multiple-Mode Liquid Dampers', Earthquake Engineering and Structural Dynamics, 1995.

Lamb, H., Hydrodynamics, 6th edition, pp. 619-621, Cambridge University Press, 1932.

Lee, J., 'Optimal Weight Absorber Designs for Vibrating Structures Exposed to Random Excitations', Earthquake Engineering and Structural Dynamics, Vol. 19, 1209-1218, 1990.

Lepelletier, T. G. and Raichlen, F., 'Nonlinear Oscillations in Rectangular Tanks' J. of Engineering Mechanics, Vol. 114(1), ASCE, pp. 1-23, 1988.

McNamara, R. J., 'Tuned Mass Dampers for Buildings', J. of the Structural Division, ASCE, Vol. 103, pp 1785-1798, 1977.

Miles, J.W., 'Nonlinear Surface Waves in Closed Basins." J. Fluids Mechanics, Vol.75, pp.419-448, 1976.

Modi, V. J. and Welt, F., 'Damping of Wind Induced Oscillations through Liquid Sloshing', J. Wind Engineering and Industrial Aerodynamics, 30, 85-94, 1988.

Modi, V. J. and Welt, F., 'Vibration Control Using Nutation Dampers', Proc. Int. Conf. on Flow Induced Vibrations, England, pp. 369-376, 1987.

Nakayama, T. and Washizu, K., 'The Boundary Element Method Applied to the Analysis of Two-Dimensional Nonlinear Sloshing Problems', International Journal for Numerical Method in Eng., Vol. 17, pp. 1631-1646, 1981.

Nayfeh, A.H. and Mook, D. T., Nonlinear Oscillations, John Wiley & Sons, Inc., pp. 161-257, 1979.

Nayfeh, A.H., Perturbation Methods, Wiley, New York, pp. 110-114, 1973.

Newland, D.E., An Introduction to Random Vibrations, Spectral & Wavelet Analysis, 3rd ed., Longman Scientific & Technical, pp371-372, 1993

Noji, T., Yoshida, H., Tatsumi, E. and Hagiuda, H., 'Study on Vibration Control Damper Utilizing Sloshing of Water', J. of Wind Engineering, Japan Association for Wind Engineering, No. 37, pp. 557-566, 1988.

Okamoto, T. and Kawahara, M., 'Two Dimensional Sloshing Analysis by the Arbitrary Lagrangian-Eulerian Finite Method', JSCE, Structural Engineering / Earthquake Engineering, Vol. 8, No. 4, 207-216, 1992.

Pacheco, B. M. and Fujino, Y., 'Approximate explicit formulas for complex modes of a two-degree-of-freedom (2DOF) system', Struct. Engineering / Earthquake Engineering, JSCE 6(1), 191-200, 1989.

Reed, D.A. and Scanlan, R.H., 'Time Series Analysis of Cooling Tower Wind Loading', ASCE, J. of Structural Engineering, Vol. 109, No. 2, 538-554, 1983.

Reed, D.A., Yeh, H., Yu, J. and Gardarsson, S., 'Experimental Investigation of Tuned Liquid Dampers', Proc. of the ASCE 1996 International Conference on Natural Disaster Reduction, Washington D.C., December, 1996

Reed, D.A., Yeh, H., Yu, J. and Gardarsson, S., 'Performance of Tuned Liquid Dampers for Large Amplitude Excitation', Proc. of the 2nd International Workshop on Structural Control, Hong Kong, December, 1996

Sayar, B. and Baumgarten, J.R., 'Linear and Nonlinear Analysis of Fluid Sloshing Damper.' AIAA J., Vol.20, No.11, pp.1534-1538, 1982.

Shimizu, T. and Hayama, S., 'Nonlinear Response of Sloshing Based on the Shallow Water Wave Theory', JSME International Journal, Vol. 30, No. 263, pp. 806-813, 1987.

Snaebjornsson, J. and Reed, D. A., 'Wind Induced Accelerations of a Building: A Case Study', Engineering Structures, Vol. 13, 1991.

Sun, L. M., 'Semi-Analytical Modeling of Tuned Liquid Damper (TLD) with Emphasis on Damping of Liquid Sloshing', Ph.D. Thesis, The University of Tokyo, September, 1991.

Sun, L. M., Fujino, Y., Chaiseri, P., Pacheco, B. M., 'The Property of Tuned Liquid Dampers using a TMD Analogy' Earthquake Engineering and Structural Dynamics, Vol. 24, pp. 967-976, 1995.

Sun, L. M., Fujino, Y., Pacheco, B. M and Chaiseri, P., 'Modelling of Tuned Liquid Damper (TLD)' Proc. 8th Int. Conf. on Wind Engineering, London, Canada, 12pp, 1991.

Sun, L. M., Fujino, Y., Pacheco, B. M. and Isobe, M., 'Nonlinear Waves and Dynamic Pressures in Rectangular TLD - Simulation and Experimental Verification -', J. Structural Engineering / Earthquake Engineering, JSCE., Vol. 6, No. 2, pp. 251-262, 1989.

Tamura, Y., Fujii, K., Sato, T., Wakahara, T. and Kosugi, M., 'Wind Induced Vibration of Tall Towers and Practical Applications of Tuned Sloshing Damper', Proceedings Vol. 1, Symposium/Workshop on Serviceability of Buildings, U. of Ottawa, Canada, May 1988.

Tamura, Y., Kousaka, R. and Modi, V. J., 'Practical Application of Nutation Damper for Suppressing Wind Induced Vibrations of Airport Towers', Proceedings of Workshop on Serviceability of Buildings, 1988.

Tsai, H. C. and Lin, G. C., 'Optimum Tuned Mass Dampers for Minimizing Steady State Response of Support Excited and Damped Systems', Earthquake Engineering and Structural Dynamics, Vol. 22, 957-973, 1993.

Tsai, T. C., 'Greens Function of Support Excited Structures with Tuned Mass Dampers by a Perturbation Method', Earthquake Engineering and Structural Dynamics, Vol. 22, 975-990, 1993.

Ueda, T., Nakagaki, R. and Koshida, K., 'Suppression of Wind Induced Vibration by Dynamic Dampers in Tower-like Structures', International Symposium for Innovation in Cable Stayed Bridges, Japan, 1991.

Villaverde, R. and Koyama, L. A., 'Damped Resonant Appendages to Increase Inherent Damping in Buildings', Earthquake Engineering and Structural Dynamics, Vol. 22, 491-507, 1993.

Wakahara, T., 'Wind-Induced Response of TLD-Structure Coupled System Considering Nonlinearity of Liquid Motion', Shimizu Tech. Res. Bull, No. 12, March 1993.

Wakahara, T., Ohyama, T. and Fujii, K., 'Suppression of Wind-Induced Vibration of a Tall Building using Tuned Liquid Damper', J. of Wind Engineering and Industrial Aerodynamics, 41-44, 1895-1906, 1992.

Warburton, G. B. and Ayorinde, E.O., 'Optimal absorber parameters for simple systems', Earthquake Engineering and Structural Dynamics. 8, 197-217, 1980.

Warburton, G. B., 'Optimum Absorber Parameters for Minimizing Vibration Response', Earthquake Engineering and Structural Dynamics, Vol. 9, 251-262, 1981.

Warburton, G. B., 'Optimum Absorber Parameters for Various Combinations of Response and Excitation Parameters', Earthquake Engineering and Structural Dynamics, 10, 381-401, 1982.

Welt, F. and Modi, V. J., 'Vibration Damping Through Liquid Sloshing: Part I --- A Nonlinear Analysis, Part II --- Experimental Results', Proc. Diagnostics Vehicle Dynamics and Special Topics, ASME, Design Engineering Division (DE), Vol. 18-5, pp. 149-165, 1989.

Xu, Y. L. and Kwok, K.C.S., 'Semianalytical Method for Parametric Study of Tuned Mass Dampers', ASCE, J. Structural Engineering, Vol. 120, No.3, 1994.

Xu, Y. L., Samali, B. and Kwok, K. C. S., 'Control of Along Wind Response of Structures by Mass and Liquid Dampers', J. Engineering Mechanics, Vol. 118, No. 1, 1992.

Yamaguchi, H and Harnpornchai, N., 'Fundamental Characteristics of Multiple Tuned Mass Dampers for Suppressing Harmonic Forced Oscillations', Earthquake Engineering and Structural Dynamics, Vol. 22, 51-62, 1993.

Yang, J. N. and Samali, B., 'Control of Tall Buildings in Along Wind Motion', J. Structural Engineering, Vol. 109, No. 1, 1983.

Appendix A. **Linear SDOF System**

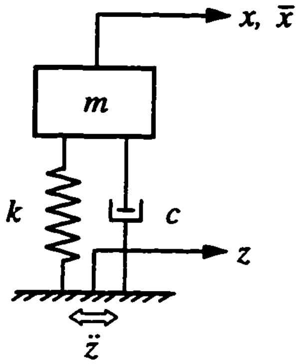

Figure A.1 SDOF system

Figure A.1 shows a SDOF system subjected to a base excitation. The equation of motion of the system is written as

$$m\ddot{\bar{x}} + c\dot{\bar{x}} + k\bar{x} = -m\ddot{z} \qquad \text{(A. 1)}$$

where *m*, *k* and *c* indicate the mass, stiffness and damping coefficients of the damper respectively; x and $\bar{x}$ are the absolute and relative displacements of the damper, respectively; z is the displacement of the base. In the next section, Equation (A.1) is solved using the frequency response analysis.

A.1 Frequency response analysis

The frequency response function is a frequency sweep series of the amplitude ratios and phase angles between the input and output functions which is useful to describe the dynamic characteristics of a linear system. If the base excitation is a harmonic function of a constant amplitude z_0 and fixed angular frequency ω

$$z = z_0 e^{i\omega t} \qquad \text{(A. 2)}$$

then, the steady state response of the system must also be a harmonic function of fixed amplitude $\bar{x}_0$ and the same frequency ω and phase difference ϕ, so that

$$\bar{x} = \bar{x}_0 e^{i(\omega t - \phi)}. \qquad \text{(A. 3)}$$

The complex frequency response functions relating $\bar{x}$ or x to z are respectively

$$H_{\bar{x}/z} = \frac{m\omega^2}{-m\omega^2 + k + ic\omega} = \frac{\beta^2}{1 - \beta^2 + i2\zeta\beta} \qquad \text{(A. 4)}$$

and

$$H_{x/z} = 1 + H_{\bar{x}/z} = \frac{1 + i2\zeta\beta}{1 - \beta^2 + i2\zeta\beta} \qquad \text{(A. 5)}$$

in which the excitation frequency ratio β and the damping ratio of the system ζ are defined as $\beta = \omega/\omega_s$ and $\zeta = c/2\sqrt{mk}$, respectively. The magnitude of $H_{x/z}$ and the phase angle ϕ between x and z are expressed respectively as

$$\left|H_{x/z}\right| = \sqrt{\frac{1 + (2\zeta\beta)^2}{(1-\beta^2)^2 + (2\zeta\beta)^2}} \qquad \text{(A. 6)}$$

and

$$\phi = \tan^{-1}\left(\frac{2\zeta\beta^3}{1 - \beta^2 + (2\zeta\beta)^2}\right). \qquad \text{(A. 7)}$$

The magnitude of $H_{\bar{x}/z}$ is determined by

$$\left|H_{\bar{x}/z}\right| = \frac{\beta^2}{\sqrt{(1-\beta^2)^2 + (2\zeta\beta)^2}}. \qquad \text{(A. 8)}$$

The frequency response function relating $\bar{x}$ to the excitation force F_e is determined by

$$H_{\bar{x}/F_e} = H_{\bar{x}/m\omega^2 z} = \frac{1}{k\beta^2} H_{\bar{x}/z}. \qquad \text{(A. 9)}$$

The dynamic magnification factor (DMF) at the given excitation frequency and the corresponding amplitude of structural displacement are calculated respectively as

$$DMF = \frac{k}{F_0} x_0 = k\left|H_{\bar{x}/F_e}\right| = \frac{1}{\beta^2}\left|H_{\bar{x}/z}\right| = \frac{1}{\sqrt{(1-\beta^2)^2 + (2\zeta\beta)^2}} \qquad \text{(A. 10)}$$

and

$$x_0 = \frac{F_0}{k} \frac{1}{\sqrt{(1-\beta^2)^2 + (2\zeta\beta)^2}}. \qquad \text{(A. 11)}$$

Note that F_0 is the amplitude of the excitation force. The maximum DMF and the corresponding amplitude of the structural displacement over the sweep excitation frequencies are obtained respectively by

$$DMF_{\max} = \frac{1}{2\zeta\sqrt{1-\zeta^2}} \qquad \text{(A. 12)}$$

and

$$x_{0,\max} = \frac{F_0}{k}\frac{1}{2\zeta\sqrt{1-\zeta^2}} \qquad \text{(A. 13)}$$

Figure A.2 shows the plots of Equation (A.6), (A.7) and (A.10) for the systems with various damping values.

A.2 Energy dissipation per cycle by a SDOF damping device

Suppose the SDOF system in Figure A.1 is a damping device which is subjected to a harmonic base excitation. The damping force F_d which is defined as the force resisting the base excitation is expressed as

$$F_d = -(c\dot{\bar{x}} + k\bar{x})\,. \qquad \text{(A. 14)}$$

Noting $-(c\dot{\bar{x}} + k\bar{x}) = m\ddot{x}$ from Equation (A.1), F_d can be calculated by

$$F_d = -(c\dot{\bar{x}} + k\bar{x}) = m\ddot{x} = -m\omega^2 x = -m\omega^2 z_0 \left|H_{x/z}\right| e^{i(\omega t-\phi)}\,. \qquad \text{(A. 15)}$$

Dividing by $m\ddot{z}_0 = -m\omega^2 z_0$, the nondimensional amplitude of the damping force F_d' becomes

$$\left|F_d'\right| = \left|H_{x/z}\right| = \sqrt{\frac{1+(2\zeta\beta)^2}{(1-\beta^2)^2+(2\zeta\beta)^2}}\,. \qquad \text{(A. 16)}$$

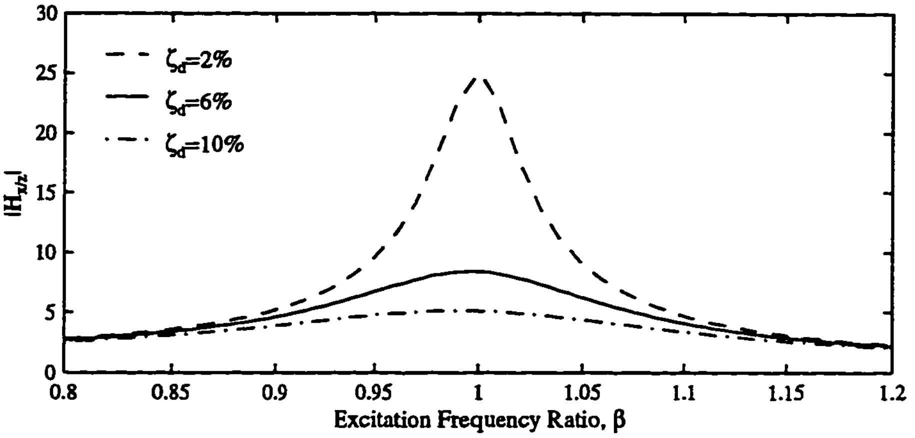

(a) Amplitude of frequency response function

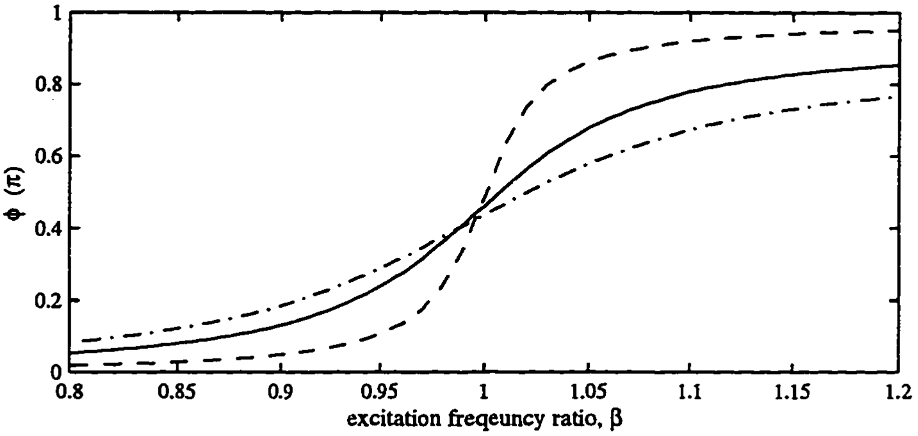

(b) Phase angle

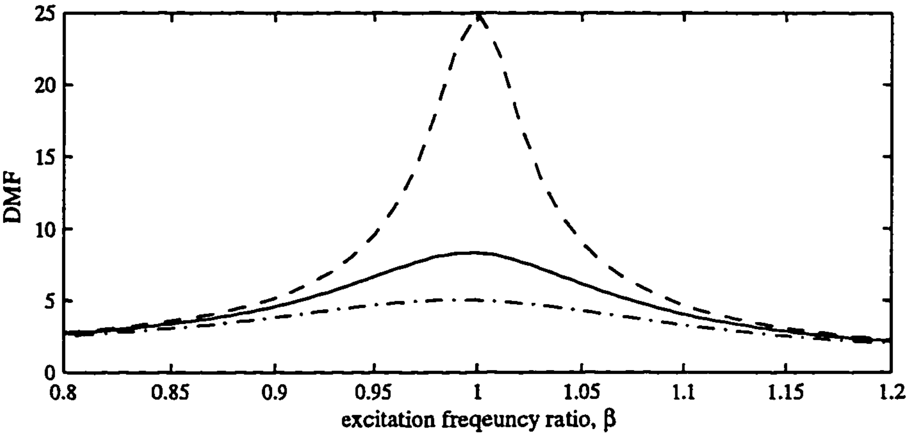

(c) Dynamic magnification factor

Figure A.2 Frequency responses of SDOF systems with various damping values calculated using Equations (A.6), (A.7) and (A.10).

The energy dissipation by the damper E_d is defined as the amount of work done by the damping forces during one cycle of the base excitation and calculated by

$$E_d = \int_{cycle} F_d dz = \int_{T} F_d \dot{z} dt = -m\omega^3 z_0^2 \left|H_{y/z}\right| \int_0^T (e^{i(\omega t-\phi)})(ie^{i\omega t})dt . \qquad \text{(A. 17)}$$

Assuming a sine wave input, i.e., $z = z_0 \operatorname{Im}(e^{i\omega t}) = z_0 \sin(\omega t)$, Equation (A.17) is rewritten as

$$E_d = -m\omega^3 z_0^2 \left|H_{y/z}\right| \int_0^T (\sin(\omega t - \phi)\cos\omega t)dt = -m\omega^2 z_0^2 \pi \left|H_{y/z}\right| \sin\phi . \qquad \text{(A. 18)}$$

Dividing by $-\frac{1}{2}m(\omega z_0)^2$, it is written in the nondimensional form as,

$$E_d' = 2\pi\left|H_{y/z}\right|\sin\phi \xrightarrow{or} E_d' = 2\pi\left|F_d'\right|\sin\phi . \qquad \text{(A. 19)}$$

Figure A.3(a) presents the sweep frequency plots of the nondimensional energy dissipation calculated using Equation (A.19) for dampers with various damping values. The damper with lower damping ratio shows the higher and narrower energy dissipation curve. The influence of the damper stiffness on the energy dissipation capacity is illustrated on Figure A.3(b). The solid line is the frequency sweep plot of the energy dissipation capacity of a SDOF system with the damping ratio of 6 % and an arbitrary natural frequency, f_{d1}. The system's natural frequency is increased by 5% and 10% respectively by increasing the stiffness of the system by 10.25% and 21% respectively. The frequency shifting ratio ξ is defined as the ratio of the natural frequency of each system to that of the original system. Hence, ξ values of three systems shown on the figure are 1.0, 1.05 and 1.10 respectively. The x-axis of the plot is the ratio of the excitation frequency to the natural frequency of the original system of which ξ = 1.0. As the natural frequency of the system is increased the energy dissipation curve for the system shifts toward higher β region. The observed trends of the influences of damping and stiffness of the system on the energy dissipation capacity is utilized in searching for an equivalent mechanical model of each TLD.

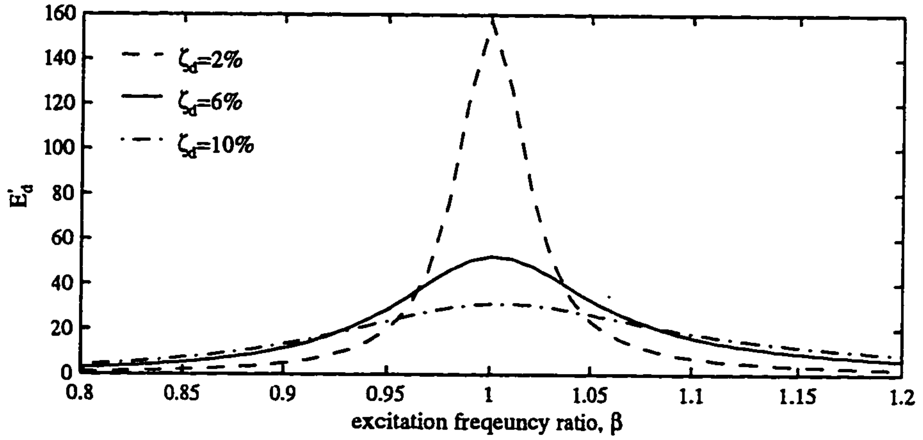

(a) with various damping values

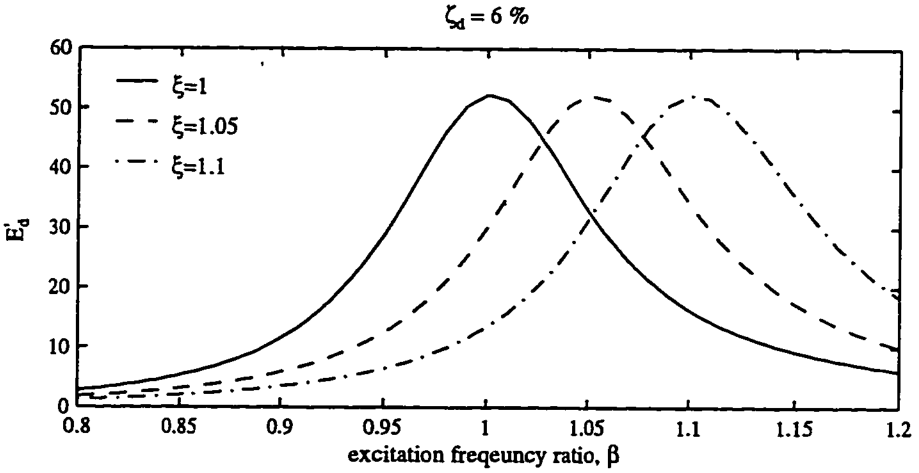

(b) with various stiffness values

Figure A.3 Energy dissipation curves for SDOF systems with various damping or various stiffness values. Calculated using Equation (A.19).

Appendix B. Linear 2DOF System under Harmonic Excitation*

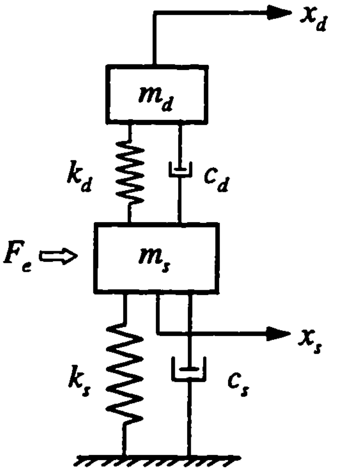

Figure B.1 SDOF structure with a damper

A SDOF structure with a SDOF mechanical damper is modeled as a simple linear two degree of freedom system as shown in Figure B.1. In Section B.1, the frequency response function of the system is derived. The steady state responses of undamped or lightly damped structures under harmonic excitation force are calculated using the frequency response function. The well-known optimal parameters of the TMD attached to an undamped or a lightly damped structure are briefly reviewed in Section B.2. The behavior and performance of the TMDs with various damping values are illustrated in Section B.3.

For the 2DOF system shown on Figure B.1, the equations of motion are written as

$$\begin{bmatrix} m_d & 0 \\ 0 & m_s \end{bmatrix}\begin{Bmatrix} \ddot{x}_d \\ \ddot{x}_s \end{Bmatrix}+\begin{bmatrix} c_d & -c_d \\ -c_d & c_d+c_s \end{bmatrix}\begin{Bmatrix} \dot{x}_d \\ \dot{x}_s \end{Bmatrix}+\begin{bmatrix} k_d & -k_d \\ -k_d & k_d+k_s \end{bmatrix}\begin{Bmatrix} x_d \\ x_s \end{Bmatrix}=\begin{Bmatrix} 0 \\ F_e \end{Bmatrix}. \qquad \text{(B. 1)}$$

B.1 Frequency response analysis

As a structure is subjected to a harmonic excitation, the external force and the steady-state response of the structure can be expressed respectively as

$$\begin{aligned} F_e &= F_0 e^{i\omega t} \quad and \\ x_s &= x_0 e^{i(\omega t-\phi)}. \end{aligned} \qquad \text{(B. 2)}$$

---

* See "List of Symbol" for the definition of the variables which are not defined in this section.

Introducing tne parameters

$$\omega_s = \sqrt{\frac{k_s}{m_s}},\ \omega_d = \sqrt{\frac{k_d}{m_d}},\ \zeta_s = \frac{c_s}{2\sqrt{k_s m_s}},\ \zeta_d = \frac{c_d}{2\sqrt{k_d m_d}},$$

$$\mu = \frac{m_d}{m_s},\ \beta = \frac{\omega}{\omega_s},\ \beta_d = \frac{\omega}{\omega_d},\ \text{and}\ \gamma = \frac{\omega_d}{\omega_s} = \frac{\beta}{\beta_d}, \qquad \text{(B. 3)}$$

the complex frequency response function relating x_s to F_e can be obtained by

$$H_{x_s} = H_{x_s/F_e} = \frac{1}{k_s\left(1 - \beta^2 + i2\zeta_s\beta - \mu\beta^2 H_{x_d}\right)} \qquad \text{(B. 4)}$$

where the complex frequency response function relating x_d to x_s is

$$H_{x_d} = H_{x_d/x_s} = \frac{1 + i2\zeta_d\beta_d}{1 - \beta_d^{\,2} + i2\zeta_d\beta_d} = \frac{\gamma^2\left(\gamma^2 - \beta^2 + (2\zeta_d\beta)^2\right) - i2\gamma\zeta_d\beta^3}{\left(\gamma^2 - \beta^2\right)^2 + \left(2\gamma\zeta_d\beta\right)^2}. \qquad \text{(B. 5)}$$

Substituting (B.5) and after some manipulations, Equation (B.4) becomes

$$H_{x_s} = \frac{1}{k_s}\frac{1}{RE + iIM} \qquad \text{(B. 6)}$$

where

$$RE = 1 - \beta^2 - \mu\beta^2 \frac{\gamma^2\left(\gamma^2 - \beta^2 + (2\zeta_d\beta)^2\right)}{\left(\gamma^2 - \beta^2\right)^2 + \left(2\gamma\zeta_d\beta\right)^2} \quad \textit{and}$$

$$IM = 2\zeta_s\beta + \frac{2\mu\gamma\zeta_d\beta^5}{\left(\gamma^2 - \beta^2\right)^2 + \left(2\gamma\zeta_d\beta\right)^2}. \qquad \text{(B. 7)}$$

The dynamic magnification factor (DMF) and its corresponding peak displacement of the structure at the given excitation frequency are obtained respectively by

$$DMF = \frac{k_s}{F_0}x_0 = k_s\left|H_{x_s}\right| = \frac{1}{\sqrt{RE^2 + IM^2}} \quad \text{and} \qquad \text{(B. 8)}$$

$$x_0 = \frac{F_0}{k_s} \frac{1}{\sqrt{RE^2 + IM^2}} \,. \tag{B. 9}$$

The normalized peak displacement of the structure at the given excitation frequency is defined as

$$x_0' = \frac{x_0}{x_{0,\max}} = \frac{2\zeta_s \sqrt{1-\zeta_s^{\,2}}}{\sqrt{RE^2 + IM^2}} \tag{B. 10}$$

where $x_{0,\max}$ is the maximum peak displacement of the structure without a damper over the sweep excitation frequencies which is expressed in Equation (A.13).

B.2 Optimum design parameters of the linear mechanical damper

Undamped Structure, $\zeta_s = 0$: Substituting $\zeta_s = 0$ into (B.7) and (B.9), the familiar Den Hartog's expression (Den Hartog, 1954) is obtained. Following the well-known procedure utilizing the existence of invariant points on the response curves, we can obtain the optimum tuning ratio and optimum damping ratio of the damper as follows,

$$\gamma_{opt} = \frac{1}{1+\mu} \quad and \qquad \zeta_{d,opt} = \sqrt{\frac{3\mu}{8(1+\mu)}} \,. \tag{B. 11}$$

Lightly Damped Structure, $\zeta_s > 0$: For the system with a damped structure, the invariant points do not exist anymore in the response curves. The optimum parameters of the damper cannot be obtained using the analytical method as for the undamped case. The optimum parameters of the damper for the system with a damped structure can be determined by a numerical search for the minimum peak response, e.g., Warburton (1980) and Tsai (1993). For the lightly damped structure ($\zeta_s \leq 0.01$) subjected to harmonic excitation, the optimum parameters of the damper were found to be

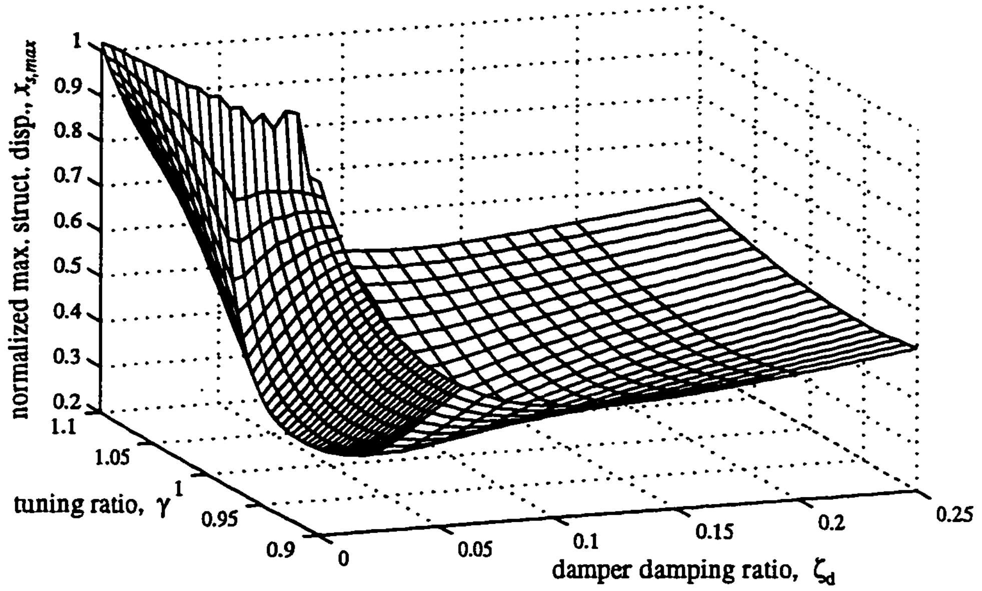

Figure B.2 Normalized peak displacements of the structure equipped with a TMD for harmonic excitation: The structural damping ratio, ζ_s=1.0 %. The mass ratio, μ=1.0 %.

$$\begin{aligned} \gamma_{opt} &\approx 0.99 \\ \zeta_{d,opt} &\approx 0.06 \end{aligned} \tag{B. 12}$$

Figure B.2 containes a 3-D plot of the normalized peak displacements of a structure equipped with various TMDs for the structural damping ratio ζ_s = 1.0 % and the damper mass ratio μ = 1.0 %. The tuning ratios γ vary in the range between 0.9 and 1.1 in the increment of 0.01. The optimum parameters for the damper as defined in Equation (B.12) are evident in this figure.

B.3 Performance of the TMD - Case study

Figure B.3 shows the frequency response plots of a lightly damped structure with three differently damped TMDs under harmonic external force. The mass ratio μ of each TMD is 1%. The structural damping ratio ζ_s is 0.7%.

For the given system, the optimum parameters were found as in Equation (B.12). In these analyses, the TMDs are tuned to the fundamental natural frequency of the structure. The damping ratios of each TMD ζ_d are 2 % (under-damped), 6 % (optimally damped) and 20 % (over-damped) respectively. The dynamic magnification factor (DMF) of each system was calculated using Equation (B.8). The figure identifies that the optimally-damped TMD reduces the peak displacement of the structure most effectively over the broad range of the excitation frequencies.

Figure B.4 shows the time history performances of each TMD under the free vibration of the structure with the initial displacement $x_0 = 50$ mm. The structural motion shows a beating phenomenon with the under-damped TMD. In general, as the damping of the TMD approaches the optimal value, the beating phenomenon weakens and finally

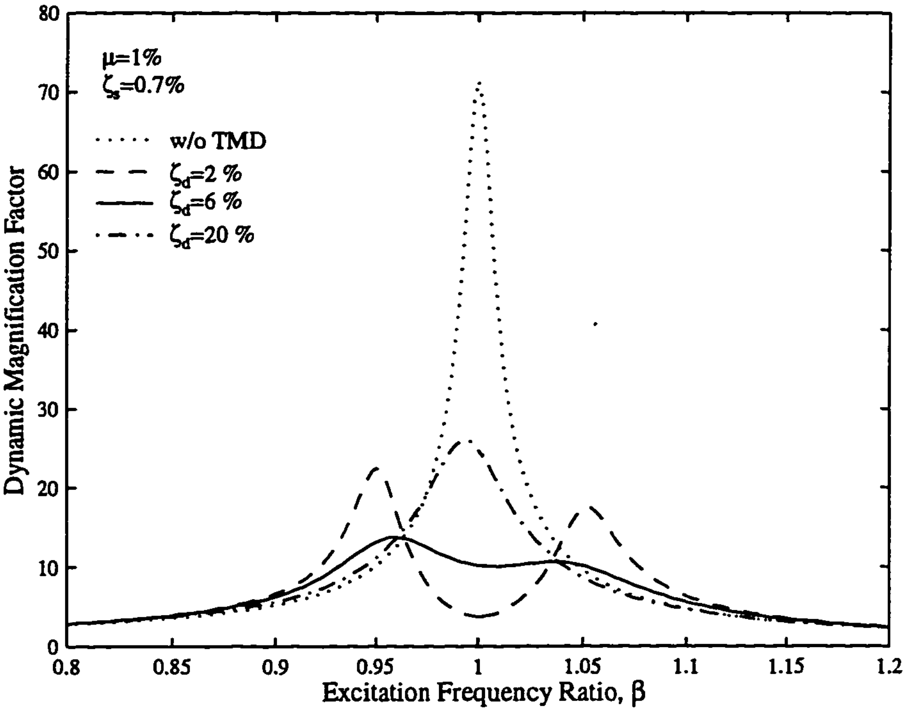

Figure B.3 Frequency response of lightly damped structures with variously damped TMDs disappears near the optimal value. If the damping of the TMD keeps increasing beyond the optimal value, the structural motion decays more slowly.

Figure B.5 shows the time history responses of a structure with the same TMDs under harmonic excitation at excitation frequency ratio β of 1.0 and 0.95 respectively. The amplitude of the external force was selected such that the maximum displacement of the structure without TMD became 50 mm under the given forcing function. Near the vicinity of the excitation frequency ratio of unity (i.e., the β = 1.0), the under-damped TMD (ζ_d = 2%) reduces the structural response most effectively. But the under-damped TMD performs worst at β = 0.95. The behavior of the over-damped TMD is opposite to that of the under-damped TMD. The optimally-damped TMD performs effectively over the broad range of the excitation frequencies. These observations are consistent with the plots in Figure B.4.

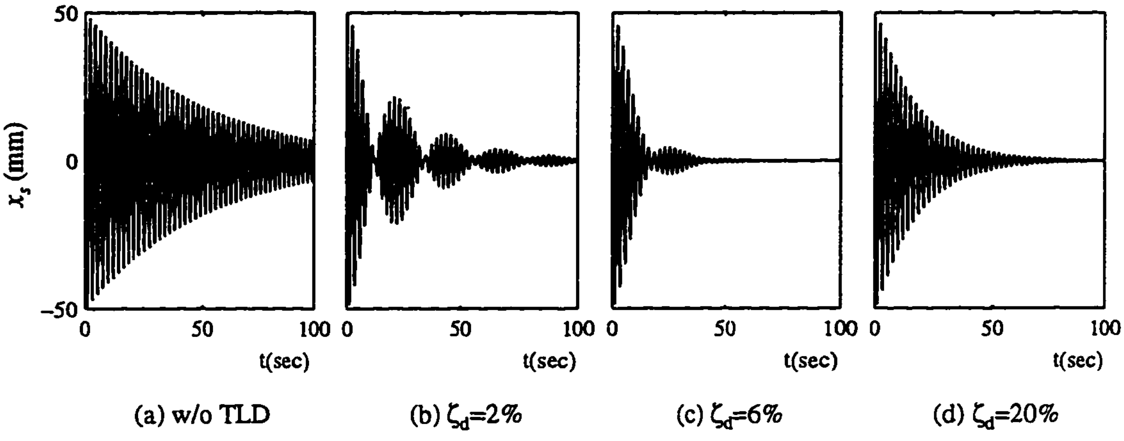

(a) w/o TLD (b) ζ_d=2% (c) ζ_d=6% (d) ζ_d=20%

Figure B.4 Time history free vibration responses of lightly damped structures with variously damped TMDs under harmonic excitation

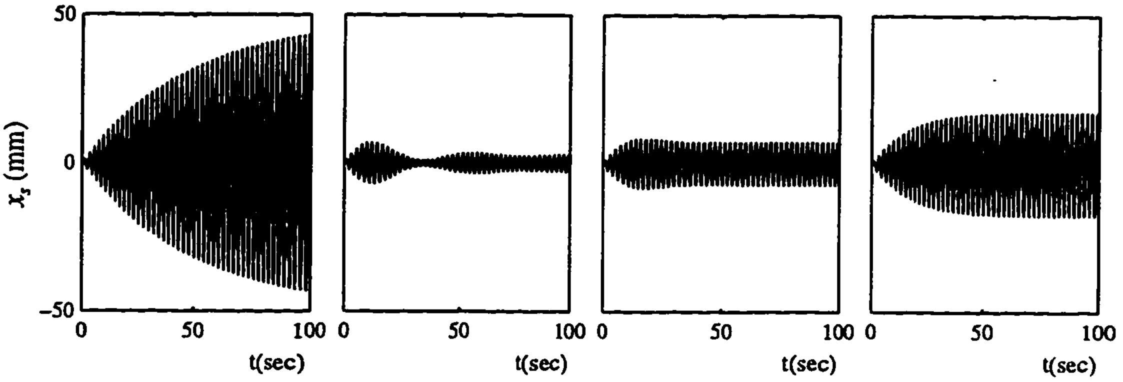

(a) no TLD (b) ζ_d=2% (c) ζ_d=6% (d) ζ_d=20%

A. β=1

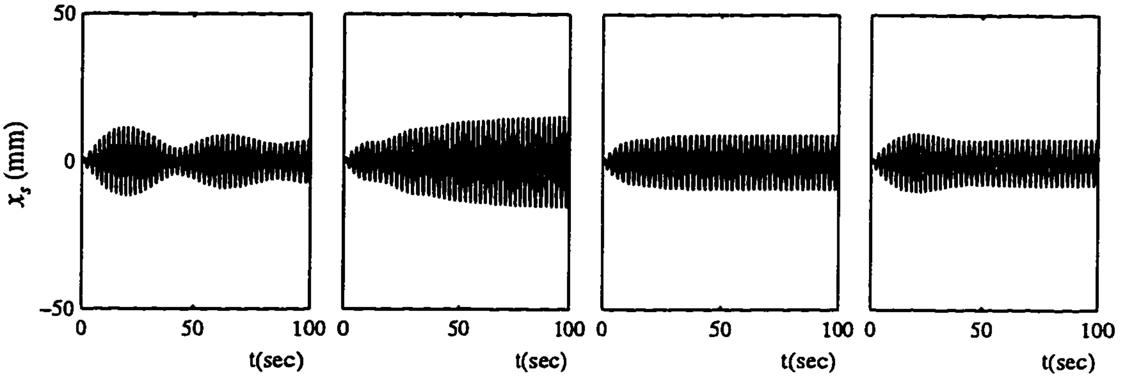

(a) no TLD (b) ζ_d=2% (c) ζ_d=6% (d) ζ_d=20%

B. β=0.95

Figure B.5 Time history forced vibration responses of lightly damped structures with variously damped TMDs under harmonic excitation

Appendix C. **Linear 2DOF System under White Noise Excitations** *

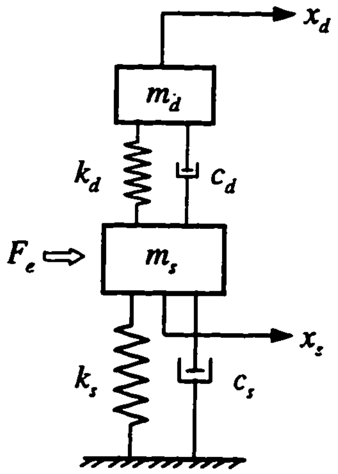

Figure C.1 SDOF structure with a damper

Figure C.1 shows a simple linear two degree of freedom system subjected to an external force. If the external force is random with a constant spectral density (white noise spectrum), the steady state response of the stationary process can be obtained. In Section C.1, the steady state response of the system is calculated using frequency response analysis coupled with spectral analysis. The optimal parameters of the TMD attached to an undamped or lightly damped structure are briefly reviewed in Section C.2.

C.1 Steady state responses

To obtain the steady-state response of the system under a random excitation with a constant spectral density S_0, the frequency response functions, H_{x_s} and H_{x_d} in Equations (B.4) and (B.5) are rewritten respectively as

$$H_{x_s} = \frac{1}{m_s(i\omega)^2 + c_s(i\omega) + k_s + m_d H_{x_d}(i\omega)^2} \quad \text{and} \qquad \text{(C.1)}$$

$$H_{x_d} = \frac{k_d + c_d(i\omega)}{k_d + c_d(i\omega) + m_d(i\omega)^2} \,. \qquad \text{(C.2)}$$

Substituting (C.2) into (C.1) and after some manipulations using (B.3), we obtain

---

* See "List of Symbol" for the definition of the variables which are not defined in this section.

$$H_{x_s} = \frac{1}{m_s}\frac{B_0 + B_1(i\omega) + B_2(i\omega)^2 + B_3(i\omega)^3}{A_0 + A_1(i\omega) + A_2(i\omega)^2 + A_3(i\omega)^3 + A_4(i\omega)^4} \tag{C.3}$$

where

$$\begin{gathered} A_0 = \omega_s{}^2\omega_d{}^2; \quad A_1 = 2\zeta_s\omega_s\omega_d{}^2 + 2\zeta_d\omega_s{}^2\omega_d; \\ A_2 = 4\zeta_s\zeta_d\omega_s\omega_d + \omega_s{}^2 + \omega_d{}^2(1+\mu); \\ A_3 = 2\zeta_s\omega_s + 2\zeta_d\omega_d(1+\mu); \quad A_4 = 1; \\ B_0 = \omega_d{}^2; \quad B_1 = 2\zeta_d\omega_d; \quad B_2 = 1; \quad B_3 = 0\,. \end{gathered} \tag{C.4}$$

The mean square response of a stationary response process is given by

$$E\left[x_s{}^2\right] = S_0 \int_{-\infty}^{\infty} \left|H_{x_s}(\omega)\right|^2 d\omega\,. \tag{C.5}$$

Substituting (C.3) into (C.5) and evaluating the integral (Newland, 3rd ed., pp.372), the mean square response is obtained in the form

$$E\left[x_s{}^2\right] = \frac{\pi S_0}{m_s{}^2}\Pi(A_0,\cdots,A_4,B_0,\cdots,B_s) \tag{C.6}$$

in which

$$\Pi = \frac{\begin{gathered} A_0B_3{}^2(A_0A_3 - A_1A_2) + A_0A_1A_4(2B_1B_3 - B_2{}^3) \\ -A_0A_3A_4(B_1{}^2 - 2B_0B_2) + A_4B_0{}^2(A_1A_4 - A_2A_3) \end{gathered}}{A_0A_4(A_0A_3{}^2 + A_1{}^2A_4 - A_1A_2A_3)}\,. \tag{C.7}$$

Substituting A_4=1, B_2=1 and B_3=0, it is simplified as

$$\Pi = \frac{-A_0A_1 - A_0A_3(B_1{}^2 - 2B_0) + B_0{}^2(A_1 - A_2A_3)}{A_0(A_0A_3{}^2 + A_1{}^2 - A_1A_2A_3)}\,. \tag{C.8}$$

Introducing new variables

$$\bar{A}_i = \frac{A_i}{\omega_s^{4-i}}; \quad \bar{B}_i = \frac{B_i}{\omega_s^{2-i}}; \tag{C.9}$$

i.e.,

$$\begin{gathered} \bar{A}_0 = \gamma^2; \quad \bar{A}_1 = 2(\zeta_s \gamma^2 + \zeta_d \gamma); \quad \bar{A}_2 = 4\zeta_s \zeta_d \gamma + 1 + \gamma^2(1+\mu); \\ \bar{A}_3 = 2(\zeta_s + \zeta_d(1+\mu)\gamma); \quad \bar{B}_0 = \gamma^2 = \bar{A}_0; \quad \bar{B}_1 = 2\zeta_d \gamma, \end{gathered} \tag{C.10}$$

Equation (C.8) is simplified as

$$\Pi = \frac{1}{\omega_s^3} \bar{\Pi} \tag{C.11}$$

where,

$$\bar{\Pi} = \frac{-\bar{A}_1 - \bar{A}_3(\bar{B}_1^2 - 2\bar{A}_0) + \bar{A}_0(\bar{A}_1 - \bar{A}_2\bar{A}_3)}{\bar{A}_0\bar{A}_3^2 + \bar{A}_1^2 - \bar{A}_1\bar{A}_2\bar{A}_3} . \tag{C.12}$$

Equation (C.6) is rewritten as

$$E\left[x_s^2\right] = \frac{\pi S_0}{m_s^2 \omega_s^3} \bar{\Pi} . \tag{C.13}$$

Mean square response of the structure without damper can be obtained by

$$E\left[x_{s,0}^2\right] = \frac{\pi S_0}{2\zeta_s m_s^2 \omega_s^3} . \tag{C.14}$$

Normalizing (C.13) to (C.14), the nondimensional mean square response of the structure is written as

$$E'\left[x_s^2\right] = \frac{E\left[x_s^2\right]}{E\left[x_{s,0}^2\right]} = 2\zeta_s \bar{\Pi} \tag{C.15}$$

which is a function of μ, ζ_s, ζ_d and γ.

C.2 Optimum design parameters for the linear mechanical damper

The optimum parameters for the damper can be determined through numerical searches for the minimum peak response by solving Equation (C.15). An extensive numerical search for the optimum parameters has been conducted and reported by Warburton (1982). Figure C.2 shows the plots for the normalized RMS displacement of a structure equipped with various TMDs as the structural damping ratio $\zeta_s = 1.0$ % and the damper mass ratio $\mu = 1.0$ %. The tuning ratio γ vary in the range between 0.9 and 1.1 with the increment of 0.01. The damper damping ratios ζ_d range from to 0.25. For the given structure, the optimum parameters were identified from the figure as

$$\begin{aligned} \gamma_{opt} &\approx 0.99 \quad and \\ \zeta_{d,opt} &\approx 0.05. \end{aligned} \tag{C.16}$$

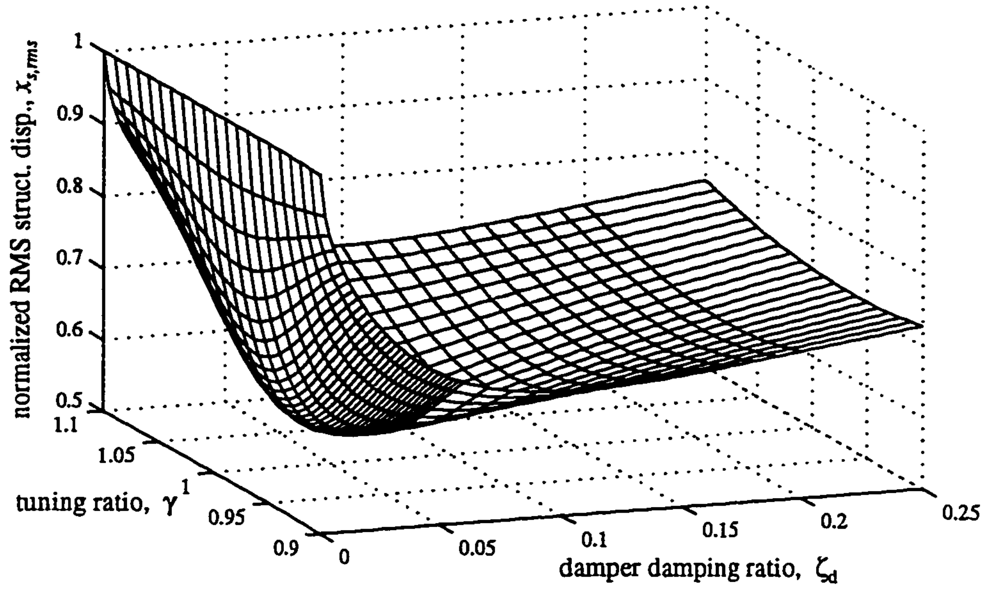

Figure C.2 Normalized RMS displacements of the structure equipped with a TMD for white noise excitation: The structural damping ratio, ζ_s=1.0%. The mass ratio, μ=1.0%.

Appendix D. **Time history analysis for a SDOF structure equipped with a TLD under an arbitrary excitation.**

As a SDOF structure equipped with a TLD is subjected to an arbitrary external force, the equation of motion is written as

$$m\ddot{x} + c\dot{x} + kx = F_e + F_d \tag{D. 1}$$

where m, c and k indicate the mass, damping and stiffness coefficients of the structure respectively; x indicates the relative displacement of the structure; F_e is the excitation forcing function; and F_d is the hydrodynamic force induced by water sloshing motion in the TLD.

In the numerical time history analysis of the structural response to the driving force, the external force is approximated as a piecewisely constant step function. At each time step, Equation (D.1) can be rewritten in the form

$$m\ddot{x}_i + c\dot{x}_i + kx_i = P_i \ . \tag{D. 2}$$

If the displacement and the velocity of the structure at time step t_{i-1} are known, i.e., x_{i-1} *and* $\dot{x}_{i-1}$ are known, the responses at the time step t_i can be obtained by solving Equation (D.2). The results are as follows:

$$x_i = e^{-\zeta\omega\Delta t}(A \sin\omega_d \Delta t + B\cos\omega_d \Delta t) + \frac{P_i}{k} \ , \tag{D. 3}$$

$$\dot{x}_i = -\zeta\omega e^{-\zeta\omega\Delta t}(A\sin\omega_d\Delta t + B\cos\omega_d\Delta t) + e^{-\zeta\omega\Delta t}\omega_d(A\cos\omega_d\Delta t - B\sin\omega_d\Delta t)\ , \tag{D. 4}$$

and

$$\ddot{x}_i = e^{-\zeta\omega\Delta t}[((2\zeta^2 - 1)\omega^2 A + 2\zeta\omega\omega_d B)\sin\omega_d\Delta t + ((-2\zeta\omega\omega_d A + (2\zeta^2 - 1)\omega^2 B)\cos\omega_d\Delta t] \tag{D. 5}$$

where, ζ and ω are the damping ratio and the natural angular frequency of the structure respectively and $\omega_d = \omega\sqrt{1-\zeta^2}$. At time step t_{i-1}, substitute $\Delta t = 0$ and we obtain

$$x_{i-1} = B + \frac{P_i}{k} \quad \Rightarrow \quad B = x_{i-1} - \frac{P_i}{k} \tag{D. 6}$$

and

$$\dot{x}_{i-1} = -\zeta\omega B + \omega_d A \quad \Rightarrow \quad A = \frac{1}{\omega_d}(\dot{x}_{i-1} + \zeta\omega(x_{i-1} - \frac{P_i}{k})). \tag{D. 7}$$

Substituting (D.6) and (D.7) into (D.3), (D.4) and (D5) and noticing $t = \Delta t$ at time step t_i, we obtain displacement, velocity and acceleration at current time step. This numerical scheme is employed to solve the dynamic equations of motion for the SDOF system with TLD as the TLD is modeled with a fluid model.

Appendix E. **The Results for the Shaking Table Experimental Investigations.**

The data and results of the energy dissipation matching procedure for the experimental cases of rectangular tanks, which are plotted in Figure 3.3, are tabulated in Table E.1. Those for numerical simulation using the random choice method, which

Table E.1: The data and results for the rectangular tanks.

Tank Size		*Water*	*Excitation Amplitude*		*NSD Model*	
Length L *(mm)*	Width b *(mm)*	Depth h_0 *(mm)*	A *(mm)*	A/L	ζ_d	κ
590	335	15	10	0.017	0.16	1.02
			20	0.034	0.22	1.08
			40	0.068	0.23	1.35
590	335	22.5	10	0.017	0.12	1.08
			20	0.034	0.15	1.08
			40	0.068	0.20	1.32
590	335	30	10	0.017	0.11	1.10
			20	0.034	0.15	1.06
			40	0.068	0.22	1.25
590	335	45	20	0.034	0.17	1.10
900	335	40	2.5	0.003	0.08	1.00
			5	0.006	0.09	1.10
			10	0.011	0.10	1.12
			20	0.022	0.15	1.02
			20	0.022	0.16	1.02
			30	0.033	0.18	1.04
			40	0.044	0.20	1.15
900	335	55	20	0.022	0.13	1.08
335	203	15	2.5	0.007	0.09	1.02
			2.5	0.007	0.07	1.00
			5	0.015	0.11	1.02
			5	0.015	0.10	1.00
			10	0.030	0.15	1.04
			10	0.030	0.14	1.04
			20	0.060	0.18	1.21
			20	0.060	0.17	1.25
			30	0.090	0.20	1.32

correspond to Figure 3.7, are tabulated in Table E.2. Table E.3 summarizes those for experimental cases of circular tanks, which are plotted in Figure 3.4.

Table E.2. The data and results for the rectangular TLDs obtained from the numerical simulation using the RCM model.

Tank Size		*Water*	*Excitation Amplitude*		*NSD Model*	
Length L *(mm)*	*Width* b *(mm)*	*Depth* h_0 *(mm)*	A *(mm)*	*A/L*	ζ_d	κ
590	335	30	10	0.017	0.11	1.04
			20	0.034	0.14	1.10
			30	0.051	0.18	1.12
			40	0.068	0.21	1.15
900	335	40	10	0.011	0.10	1.02
			20	0.022	0.13	1.04
			30	0.033	0.16	1.06
			40	0.044	0.17	1.08

Table E.3. The data and results for the circular tanks.

Tank Size	*Water*	*Excitation Amplitude*		*NSD Model*	
Diameter D *(mm)*	*Depth* h_0 *(mm)*	A *(mm)*	*A/L*	ζ_d	κ
690	15	10	.017	0.14	1.00
		20	.034	0.20	1.12
		40	.068	0.23	1.30
	22.5	10	.017	0.15	1.00
		20	.034	0.19	1.15
		40	.068	0.23	1.32
690	30	2.5	.004	0.06	1.06
		5	.008	0.07	1.15
		10	.017	0.15	1.15
		20	.034	0.19	1.18
		30	.051	0.16	1.23
		40	.068	0.19	1.35
	45	5	.008	0.07	1.00
		10	.017	0.10	1.04

Appendix F. **Shallow-Water Wave Theory**

Assuming an inviscid incompressible fluid in a constant gravitational field, the laws of mass conservation and momentum conservation give

$$\nabla \cdot \vec{q} = 0 \tag{F.1}$$

$$\rho(\vec{q}_t + \vec{q} \cdot \nabla \vec{q}) = -\nabla(p + \rho g y) \tag{F.2}$$

where $\vec{q} = u\vec{i} + v\vec{j} + w\vec{k}$ is the velocity vector in which $\vec{i}$, $\vec{j}$, $\vec{k}$ are the cartesian unit vectors along axes x, y and z, respectively, p is the pressure, ρ is the fluid density and g is the acceleration of gravity.

Consider the two-dimensional flow as shown on Figure F.1 by assuming that the velocity field is independent of z-axis (the lateral direction). Equation (F.1) can be rewritten as

$$u_x + v_y = 0 \tag{F.3}$$

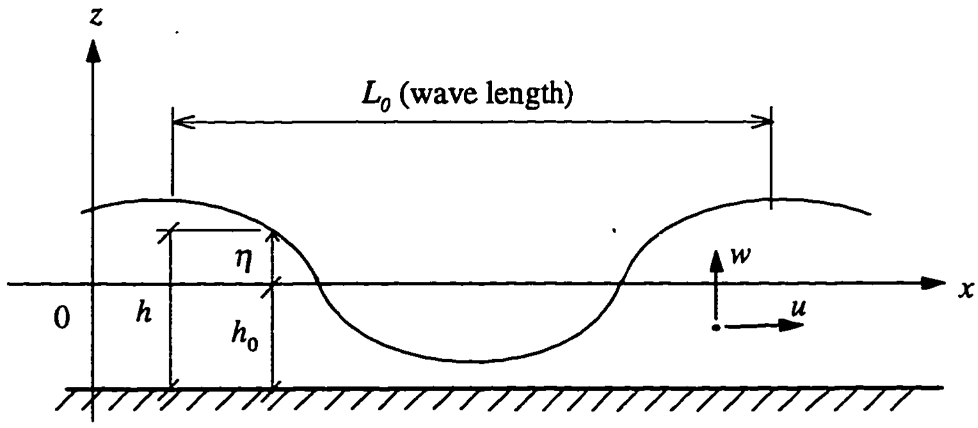

Figure F.1 Geometry of the shallow water wave

Integration of (F.3) over the water depth, $y = -h_0$ to η, leads to

$$\int_{-h_0}^{\eta} (u_x + v_y)dy = \frac{\partial}{\partial x}\int_{-h_0}^{\eta} udy + [v]_{y=-h_0}^{y=\eta} [u]_{y=\eta}\eta_x - [u]_{y=-h_0} h_{0,x} = 0 \qquad \text{(F.4)}$$

For a flat horizontal bottom, $h_{0,x} = 0$ and the last term disappears. Now introducing the kinematic boundary conditions at the bottom and the free surface

$$v = \eta_t + u\eta_x \text{ on the free surface, } y = \eta \qquad \text{(F.5)}$$

$$v = 0 \text{ on the bottom, } y = -h_0 \qquad \text{(F.6)}$$

Equation (F.4) is simplified as

$$\frac{\partial}{\partial x}\int_{-h_0}^{\eta} udy + \eta_t = 0 \qquad \text{(F.7)}$$

Noticing the disturbed water depth, $h = \eta + h_0$ hence $h_t = \eta_t$ and u is constant over the water depth, equation (F.7) can be rewritten as the final form

$$h_t + (uh)_x = 0 \qquad \text{(F.8)}$$

In hydrostatic pressure field, i.e., $p_y = -\rho g$ or, $p = \rho g(\eta - y)$, the momentum conservation in the horizontal direction from the equation (F.2) becomes

$$u_t + uu_x + vu_y = -g\eta_x \qquad \text{(F.9)}$$

Again, noticing $u_y = 0$ and $h_x = \eta_x$, the equation (F.9) becomes in the final form

$$u_t + uu_x + gh_x = 0 \qquad \text{(F.10)}$$

Equations (F.8) and (F.10) are the shallow-water wave equations. The wave motions based on the shallow-water wave equations are nondispersive and fully nonlinear.

VITA

Jin Kyu Yu

The author was born in Korea on August 7, 1957. He earned a Bachelor of Science degree in Architectural Engineering in January 1981 from Seoul National University in Seoul, Korea. After graduation he worked for five years as a field construction engineer for Dong Bu Construction Company.

He then came to U.S. to pursue an advanced degree in structural engineering. After graduating from Drexel University in June 1989 with a degree of Master of Science in Civil Engineering, he worked as a structural consulting engineer responsible for structural design of building structures.

In September 1993 he started his Ph.D. study at University of Washington in the Structural and Geotechnical Engineering and Mechanics Program of the Civil Engineering Department. He was interested in the field of structural vibration control and made his Ph.D. dissertation titled "Nonlinear Characteristics of Tuned Liquid Damper".

After graduation he plans to continue his practice in building design and apply his experience and knowledge of the structural vibration control to the practice.